Victoria Kürzinger

Determination and Differentiation of the Hydrothermal Precipitates of Panarea, Italy

68 pages, 54 figures, 11 tables, 46 references

Abstract

Panarea Island comprises a complex shallow-marine hydrothermal system which has been of great interest for geoscientific research since many years. The shallow-marine gray smoker 'Black Point' is of particular concern for interdisciplinary working-groups. Apart from this geoscientific highlight, a common feature in the volcanically active area is the cementation of volcanoclastic sediments by hydrothermal mineral precipitates. Most of these secondary minerals develop under reducing conditions. Thus, oxidation as additional alteration is expected when the mineral phases get into contact with ambient air or sea water, which is enriched in oxygen in respect to the hydrothermal fluids. A special sampling method, using a protective atmosphere, is supposed to give an insight into the native mineralogical and geochemical circumstances and prevailing properties in the different facies of mineral precipitates. Furthermore, a comprehensive investigation of each type of cement was carried out using geochemical and mineralogical analytical methods from cm to µm scale.

Sulfide ore minerals, iron(hydr)-oxide precipitates, and elemental sulfur are the major types of secondary minerals in the sediment or near the seafloor. Additionally, clay minerals occur as hydrothermal alteration product of the underlying volcanic bedrock. Hot and acidic fluids are emitted at the seafloor and produce a reducing environment in their immediate vicinity. However, the relatively shallow situation of 30 m water depth is responsible for the dynamic of the system in respect to changing oxic and anoxic conditions.

Zusammenfassung

Die Insel Panarea umfasst ein komplexes, flachmarines Hydrothermalsystem, welches seit vielen Jahren von großem Interesse für die geowissenschaftlichen Forschungen ist. Von besonderer Bedeutung für interdisziplinäre Arbeitsgruppen ist der flachmarine graue Raucher ‚Black Point'. Neben diesem geowissenschaftlichen Highlight ist die Zementation der vulkanoklastischen Sedimente im vulkanisch aktiven Gebiet durch hydrothermale Mineralausfällungen ein charakteristisches Merkmal. Die meisten dieser sekundären Minerale bilden sich unter reduzierenden Bedingungen. Demnach wird Oxidation als eine zusätzliche Alteration erwartet, wenn diese Mineralphasen mit Luft oder Meerwasser in Kontakt kommen, welches relativ zu den hydrothermalen Fluiden sauerstoffangereichert ist. Eine besondere Methode der Probenahme unter Verwendung einer geschützten Atmosphäre soll Aufschluss über die ursprüngliche Mineralogie, die geochemischen Rahmenbedingungen und vorherrschenden Parameter der verschiedenen Mineralausfällungen

geben. Weiterhin wurde eine umfassende Untersuchung jedes Zementtyps im cm- bis μm-Maßstab mit geochemischen und mineralogischen Analysemethoden durchgeführt.

Sulfidische Erzminerale, eisen(hydr)-oxidische Ausfällungen und elementarer Schwefel bilden die Haupttypen der sekundären Minerale in den Sedimenten oder nahe des Meeresbodens. Des Weiteren treten Tonminerale als hydrothermales Alterationsprodukt des unter den Sedimenten liegenden vulkanischen Gesteins auf. Heiße und saure Fluide treten am Meeresboden aus und erzeugen in unmittelbarer Nähe ein reduzierendes Umfeld. Allerdings ist die relativ flache Lage von 30 m Wassertiefe für die Dynamik des Systems in Hinsicht auf die wechselnden oxischen und anoxischen Bedingungen verantwortlich.

Acknowledgements

List of abbreviations

Contents

1   Introduction

1.1   Preface

Hydrothermal systems connected with volcanic activity and geodynamic processes occur in many places worldwide. Their importance for the understanding of the Earth and its processes has been known for a long time. Volcanic activity is not only reflected in the eruption of lava but also in the exhalation of volcanic gases. Subaerial and subaqueous evidences of magma degassing at depth are the discharge of fluids occurring at the Earth's surface or the seafloor as hydrothermal vents, also described as fumarolic fields (Inguaggiato et al., 2018).

The most active volcanoes in Europe are found in Italy (e.g. Etna, Stromboli, Marsili). Panarea, an island of the Aeolian Arc, comprises a complex shallow-marine hydrothermal system which has been in focus of geoscientific research for many years. The system is known as a natural field laboratory on a diversity of environmental issues such as ocean acidification, CO_2 sequestration or volcanic forecasting. Due to its situation at water depths of up to 30 m, it is reachable by scientific divers and suits well for different types of in-situ investigations and long-term monitoring. Especially geoscientific highlights as the shallow-marine gray smoker 'Black Point' make the Panarea system a hotspot for scientists of different disciplines from all over the world. The CMAS Scientific Diving Center Freiberg organizes research expeditions to Panarea at least once a year since 2006. Interdisciplinary working-groups cover various topics about geological, sedimentological and volcanological issues. Also, hydro(geo-)logical, ecological and technical tasks are in focus of recent work.

The focus of this thesis is set on developing a general inventory of cements and mineral precipitates related to the fluid emanations in the hydrothermal system of Panarea Island and the surrounding islets.

1.2 Submarine hydrothermal systems

A submarine hydrothermal system comprises the process of sea water heating beneath the seafloor. The heated sea water extracts metals from volcanic rocks and gets enriched in dissolved metals. Together with sulfur, these fluids, which can be water, gas or a mixture of both, are discharged at the sea floor through hydrothermal vents. Special cases where an immediate chemical reaction between the discharging hydrothermal fluids and the surrounding sea water in form of chimney-shaped precipitates can be seen are black, white or gray smokers. The name depends on the color of the exhaling smoke and the precipitated minerals which are a result of the elements dissolved in the fluids.

The focus of hydrothermal activity research is mainly focused on the environment around black smokers. Such sites are situated in deep back-arc basins and along mid-ocean ridges which are volcanically active (Pichler, 2009). However, hydrothermal activity in submarine settings is not restricted to the deep sea. Hydrothermal vents with rather different characteristics and appearance are found as well in shallow-marine environments (< 200 m water depth) along active transform faults as well as on the flanks of volcanic ocean islands and arc volcanoes originating in subduction zones (Pichler, 2009; Aliani et al., 2010). Tectonic conditions strongly control the occurrence of hydrothermalism because a high thermal gradient is necessary to initiate the circulation (Pichler, 2009). A thermal source is given by heat release from magma intrusions or by heat generation along faults and fractures.

Hydrothermal fluids are gases and hot waters, enriched with respect to certain elements (e.g. As, Cd, Cu, Fe, Pb and Zn) due to intense water-rock interactions. Meteoric water, in or near terrestrial areas, and sea water are likely sources for the aquatic phase whereas the gas mainly results from magma or phase separation in the system. The initial chemical composition of hydrothermal fluids in shallow-marine environments and thus their origin is hard to define. Mixing of every combination of magmatic, meteoric and sea water is possible and affects certain properties and parameters of a hydrothermal system. Especially affected are chemical composition, gas content and temperature of fluids (Pichler, 2009). Gases may have a similar chemical composition to volcanic gases which discharge from adjacent volcanoes. Main components of such volcanic gases are CO_2 and H_2S followed by minor concentrations of SO_2, CH_4, and He (Ellis and Mahon, 1964; Tassi et al., 2009; Inguaggiato et al., 2018).

One example of such an environment is the shallow-marine hydrothermal system of Panarea (Italy) in the volcanic back-arc region in the south of the Tyrrhenian Sea.

1.3   Task and aims

Small-scale variations of mineral precipitates imply similar formation conditions of the secondary minerals or changes of parameters (e.g. pH, temperature, fluid composition, redox potential) in the system. The genesis of mineral precipitations in active hydrothermal discharges will be assessed considering the influence of geochemistry and fluid dynamics. The occurrence of a gray smoker and certain mineral associations suggests a genetical similarity of mineral precipitation in the hydrothermal system of Panarea and processes in deep sea black smoker environments. To analyze oxidation processes and consequent alterations of the minerals which mainly develop in reducing settings, a comparison of conventional sampling with a sampling method using a protective atmosphere to prevent further alterations is necessary. In this case, nitrogen is used because it is an inert, harmless gas, ensuring safe handling. The processes and resulting features are presented by genetical and/or depositional models. It is beyond doubt that microorganisms are involved in the formation of these deposits, but the investigation of this topic was not in the scope of this work.

Field-methods include sampling (under protective atmosphere) and preparation of rock samples using scientific diving and standard geological techniques. All field work was done during the excursion of SDC to Panarea in September 2017. Suitable lab-methods including geochemical and mineralogical analysis are optical microscopy, µXRD and SEM-EDX. Sample material from previous expeditions (2006-2017) was checked for relevance and was included to the investigations.

The acquired data are combined to genetical models in respect to mineral precipitations in the system and their impact on the surrounding sedimentary system.

2   Description of the investigation area

2.1   State of research – hydrothermal system Panarea

The island Panarea is one of the Aeolian Islands in the south of the Tyrrhenian Sea, which is part of the Mediterranean Sea (Fig. 1). In this area, the subduction of the African Plate under the Eurasian Plate results in a calc-alkaline volcanism and the development of a back-arc system which is known as the Aeolian Arc. This volcanic province is made up of seven major islands (Alicudi, Filicudi, Lipari, Panarea, Salina, Stromboli and Vulcano) and several seamounts, in particular Palinuro and Marsili (Gamberi et al., 1997; Calanchi et al., 2002). The activity of numerous arc volcanos shows that the system is still dynamic. Due to the ongoing subduction, hydrothermal systems developed which are associated with the calc-alkaline volcanism.

Panarea is located about 50 km north of Sicily and belongs to the active volcanic system of Stromboli. The island is the emergent part of a submarine stratovolcano with more than 1700 m in height and with an area of roughly 3.5 km² it is the smallest Aeolian Island (Esposito et al., 2006). Also, the group of islets to the east of Panarea, namely Basiluzzo, Bottaro, Dattilo, Lisca Bianca, Lisca Nera and Panarelli, emerged from a submarine platform eroded at the top of the volcano, and developed, in general, between 150 and 24 ka before present (Esposito et al., 2006; Lucchi et al., 2013).
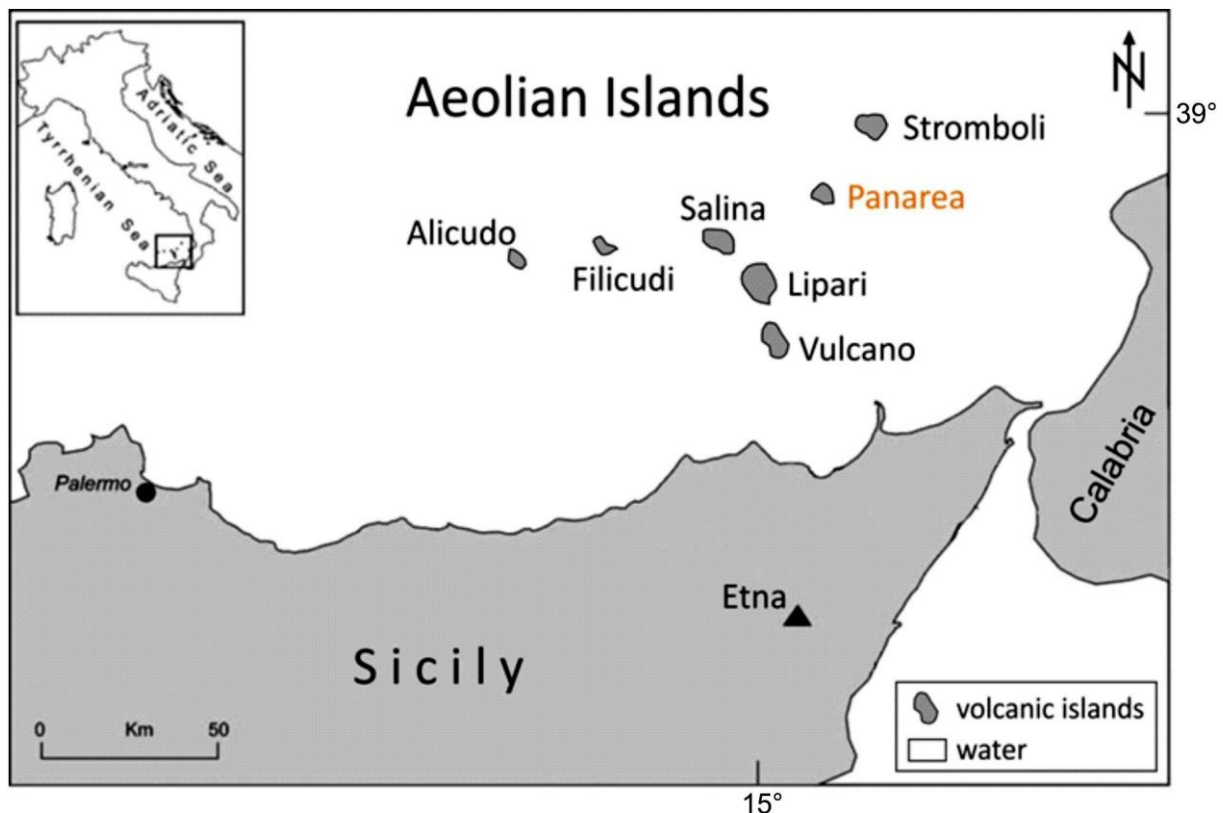
Fig. 1:   *Location of the southern Tyrrhenian Sea and Aeolian Islands (modified after Esposito et al., 2006).*

The presence of gas exhalations in the area around Panarea was noticed by Dumas and d'Austria for the first time at the end of the 19th century followed by a report written by Mercalli in 1891 (Italiano and Nuccio, 1991). At a depth of up to 30 m, several gas discharges have occurred, especially in the area between the islets to the east of Panarea Island. Those gases discharge from fractures that probably represent the main tectonic trends described in chapter 2.2.

Hydrothermal systems need a continuous supply of thermal energy. The hydrothermal energy of the Panarea system comes from a hot, shallow magmatic intrusion which causes a positive gravimetric anomaly in this area (Italiano and Nuccio, 1991). The thermal energy emitted by the magmatic intrusion heats circulating water in the seafloor, forming the driver for the hydrothermal activity in the area around Panarea Island (Fig. 2).
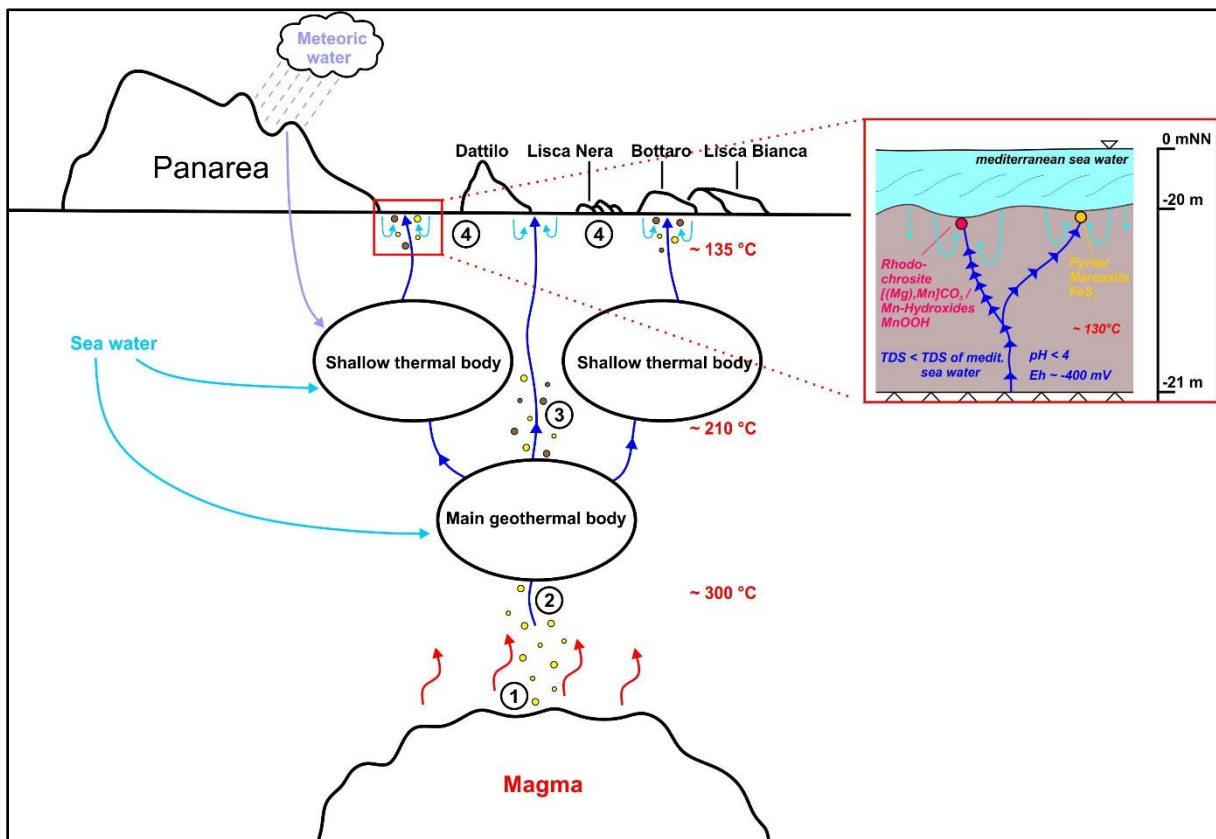
Fig. 2: *Sketch of the hydrothermal system of Panarea (modified after Italiano and Nuccio, 1991; Stanulla et al., 2017), not to scale. (TSD = total dissolved solids). (1) Degassing of magma; (2) Fluid-rock interaction; (3) Condensation and water-rock interaction, phase separation likely; (4) Contamination with sea water and precipitation of secondary minerals, phase separation likely.*

Magma degases in a depth of a few kilometers setting free volatiles such as CO_2, HCl, H_2S and SO_2. Those deep fluids, being thermally fed by energy release from the local magmatic heat source, have temperatures of 350 °C and above (Italiano and Nuccio, 1991). During their ascent to the surface, fluid-rock interaction takes place resulting in an increased concentration of Al, Fe, Mn, Si and other elements due to the acidic and aggressive

character of the hydrothermal fluids (Stanulla et al., 2017). The main geothermal body, defined as a deep water reservoir with a temperature of about 240 °C, is recharged by both cooler, circulating sea water and hot fluids. Pressure and temperature of the hydrothermal fluids decrease continuously with their ascent. If the ascent is fast and the pressure relatively low, ascending water starts to boil which causes phase separation resulting in the formation of brine and steam. Further up the water vapor condenses and mixes with geothermal, meteoric and/or sea water. Phase separation can take place at every depth if the boiling temperature of the fluid lies above the required pressure. Evidence for phase separation, in terms of water with lower electric conductivity (EC) than sea water, is found in nearly every diving location, but especially at 'Black Rock' in La Calcara (personal communication with B. Merkel, SDC Freiberg). However, the lower EC-values at this location can be caused by the influx of meteoric water as well. According to Italiano and Nuccio (1991) and Capaccioni et al. (2007), ascending fluids are separated into two shallow thermal bodies (temperature ranges from 170 to 210 °C). These thermal waters locally emerge from the seafloor with temperatures up to 135 °C (close or at boiling point). Within this mixing zone of hot geothermal water and colder ocean water pH, redox potential (Eh), and temperature change abruptly which initiate the precipitation of secondary (post-sedimentary) minerals (Stanulla et al., 2017). One of the shallow thermal bodies is located beneath the islets and gets recharged only by cold sea water. The second one is most likely situated beneath Panarea Island and is recharged by marine waters as well as meteoric water, as measurements of electric conductivity suggest (Appendix: Tab. 12).

In November 2002, a violent gas outburst occurred in the east of Panarea near Bottaro. It was interpreted as the expression of a local and sudden input of magmatic-related fluids which chemical composition has changed since the end of 2002 (Capaccioni et al., 2007; Tassi et al., 2009; Aliani et al., 2010). In advance of this degassing event, fluids, especially gases, were dominated by CO_2 and H_2S. During that crisis however, the fluids were a result of mixing of the CO_2-rich gas phase and condensed water. High water-rock interaction results in an intensive acidification of the mixture by dissolved magmatic components like SO_2 and HCl (Lowell et al., 1995; Capaccioni et al., 2007; Tassi et al., 2009).

Temperature, redox potential and pH-values are the most important physico-chemical parameters of mineral precipitation. The temperature of the emitted fluids mainly depends on gas content, salinity, and pressure in consequence of the water depth (Pichler, 2009). That implies: the higher the salinity the deeper the discharge at the seafloor, and the lower the gas content the higher the temperature of the fluid. On the other hand, pH-values are largely controlled by the fluid composition because of high water-rock interactions as previously mentioned.

The precipitation of secondary mineral phases is a spontaneous but periodical process. Due to the formation of new minerals from thermal waters and the depletion of certain elements that pass over from these fluids to precipitates, the chemistry of the fluids change. Those secondary minerals occur as cements or disseminated minerals in clastic sediments and/or crusts around pre-existing clasts. The type of mineral that is formed depends significantly on fluid composition and boundary conditions (temperature, Eh and pH).

Formation of discharge structures and precipitates

The volcanoclastic sediments in the 'Panarea system' are affected by processes of hydrothermal alteration. A common feature is the cementation of those sediments by hydrothermal mineral precipitates. Three major types are presently known: sulfide minerals occurring as ore aggregates in water-dominated discharges like in La Calcara, iron(hydr)-oxide cements prevailing in discharge features of the Fe-tube facies especially at Basiluzzo, and sulfuric cements in gas-dominated discharges, e.g. Point 21 (Stanulla et al., 2017).

Emanations of gas and hot water are typical characteristics of an active volcanic system. The gas comes from a source beneath the sediment either from magma in a depth of several km, from hydrothermal reservoirs in depths of some hundreds of meters or both (Italiano and Nuccio, 1991; Lowell et al., 1995). These volatiles find their way through an initial pathway to the surface. Such initial pathways can be pore spaces of the overlying sediment or primary fractures and faults through which gas comes from a hydrothermal reservoir in the Earth's crust. Fluids can react with existing substances and form mineral precipitates. This occurs if the fluid contains appropriate chemical substances at specific environmental conditions.

Hydrothermal discharge structures are a result of gas and water emissions and can be subdivided into secondary mineral precipitation, mostly in form of cementation, and erosive structures. The formation of these features is caused by a mixture of hydrothermal water, sea water and emanated gas while water acts as transport agent for dissolved elements. Two main types of discharge structures are common in the Panarea system: tubes and cones. As pictured in Fig. 3, a cone resembles a small crater or column, depleted of its fine-grained material due to a gas flow from an initial source through pathways in the sediment (Stanulla et al., 2017). Mineral precipitation is responsible for the solidification of an unconsolidated cone and occurs because of changes in environmental conditions, like pH, water temperature or Eh.
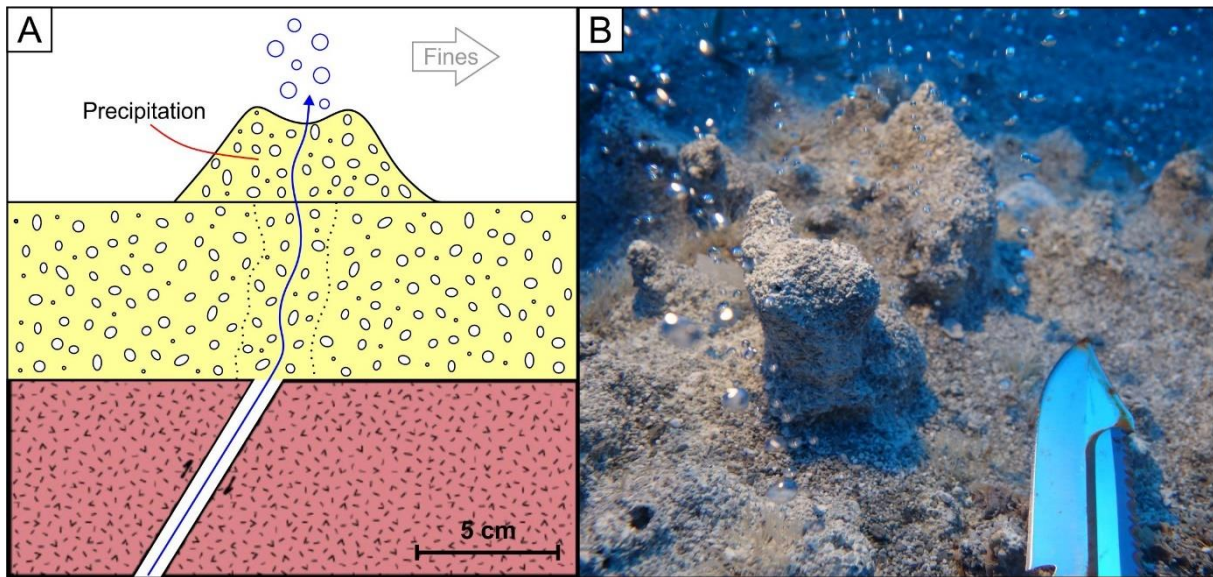
Fig. 3: *A: Section of the formation of a cone (modified after Stanulla et al., 2017); B: Cones, made of coarse sand to fine gravel (photo by R. Stanulla), Area 26 – 'Brodor'.*

The formation of a tube (Fig. 4) also starts with fluids that migrate through the sediment and cause an initial ring-shaped structure, which defines the dimension of a tube. Commonly, tubes do not develop immediately, but in events. The number of events can be seen in distinct layers or laminae, so multistory tubes and clogging are possible features (Stanulla et al., 2017).
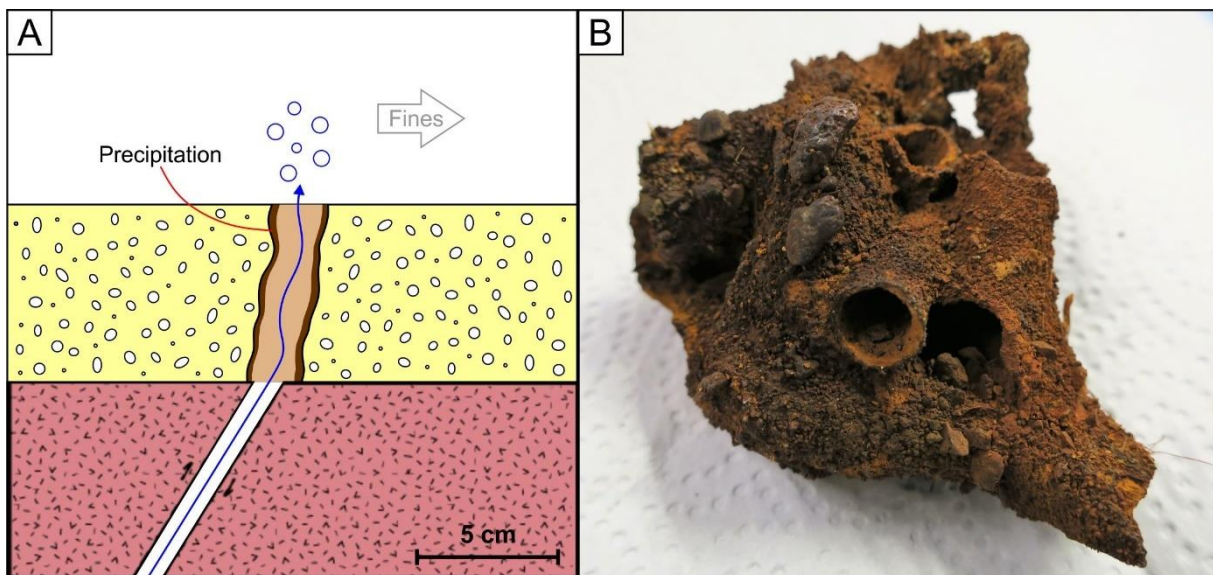
Fig. 4: *A: Section of the formation of a tube (modified after Stanulla et al., 2017); B: Iron tubes (TFe) from La Calcara – 'Black Rock'.*

The formation of fluid discharge features is further elaborated in Stanulla et al. (2017) and will not be further discussed in this thesis.

2.2   Lithostratigraphy and tectonics

The island Panarea is mainly composed of andesitic to dacitic lavas formed during the period from ca. 149 to 127 ka before present (Esposito et al., 2006). Between the volcanic layers pyroclastic deposits were embedded. The smaller islands to the east of Panarea, which are dated back to ~130 ka, are remains of lava domes that are composed of high potassium calc-alkaline dacitic and andesitic lavas (Calanchi et al., 2002; Esposito et al., 2006). Three lithostratigraphic units have been recognized in the immediate vicinity of the islets by Esposito et al. (2006) and were verified by Lucchi et al. (2013). These units are pictured in Fig. 5.
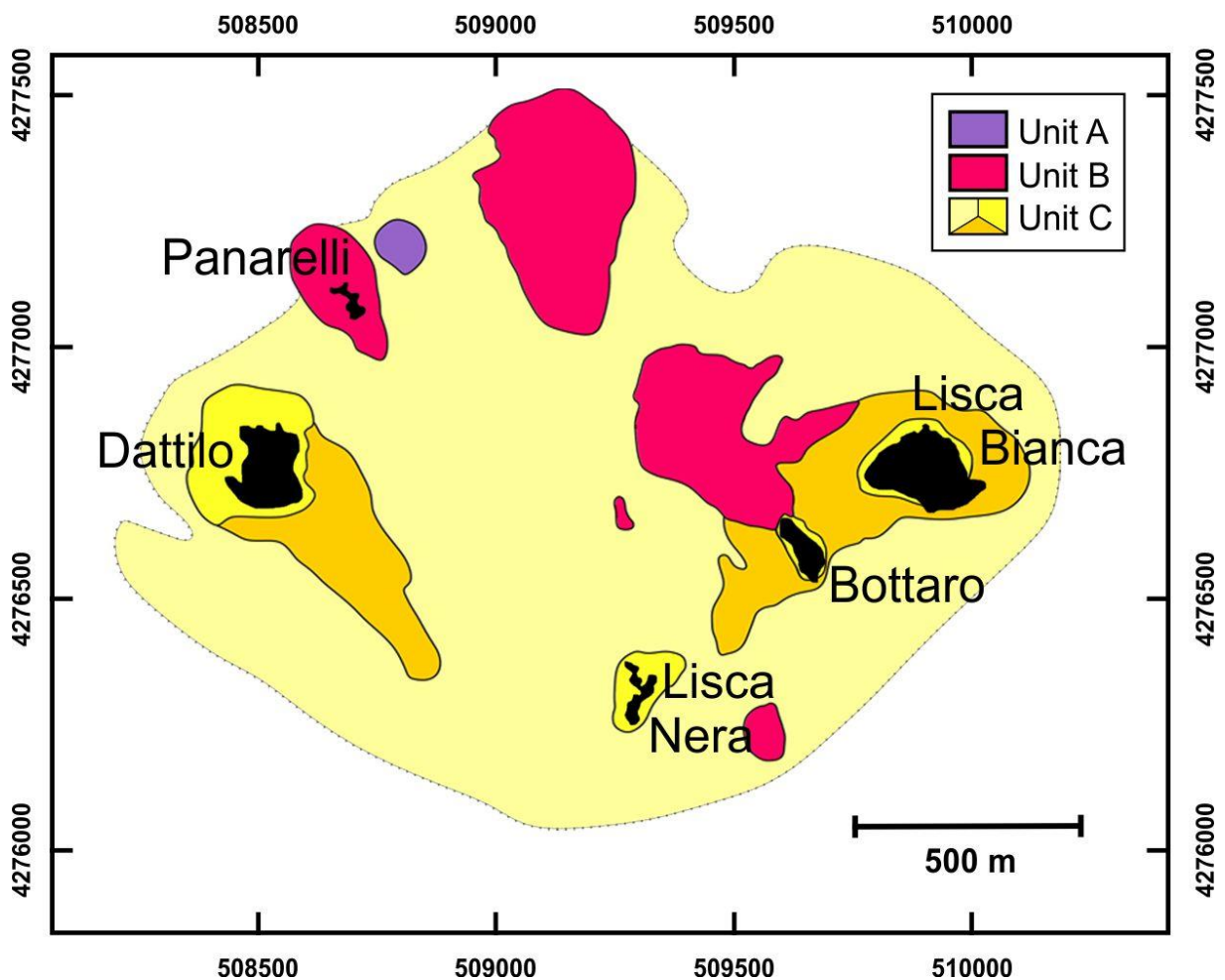
Fig. 5: *Simplified map of the lithostratigraphic units in the area of the islets in the east of Panarea (modified after Esposito et al., 2006), coordinates are given in UTM WGS 84.*

<u>Unit A:</u> The lava of the oldest unit is a usually dark highly porphyritic lava of andesitic composition with amphiboles and plagioclases of mm in size. Unit A itself is located in 26 to 30 m water depth to the east of Panarelli, but clasts of this unit are found in unit B as well.

<u>Unit B:</u> The porphyritic lava of this unit has a basaltic to andesitic composition. It comprises euhedral plagioclase phenocrysts, a few clinopyroxenes, relatively small amounts of biotite, and olivine as well as oxides and dispersed grains of volcanic glass. From the perspective of mineralogy and texture, the lava of this unit is comparable with the lava which builds up the islets. Hence, this lava (unit B) belongs with high probability to the eroded part of merging lava domes and contains xenoliths of older lavas from mm to dm size. The unit partly shows the original characteristics of a lava flow but is also highly overprinted due to massive hydrothermal alteration.

<u>Unit C:</u> The youngest unit of this area consists of sediments that cover the seafloor around Panarea and its islets and is estimated to be Holocene in age. The sediments are composed of stratified sand and gravel as well as conglomerate, partly transitional to breccia. The sediments of this unit were formed because of the (marine) erosion of Panarea and the small islands explaining the presence of porphyritic basaltic-andesitic clasts from unit A and B. Because of the short distance of transportation and scarce reworking, proximal fanglomerates and conglomerates were encountered. Further afar (distal), sand is found as a result of wave reworking and re-sedimentation of clasts.
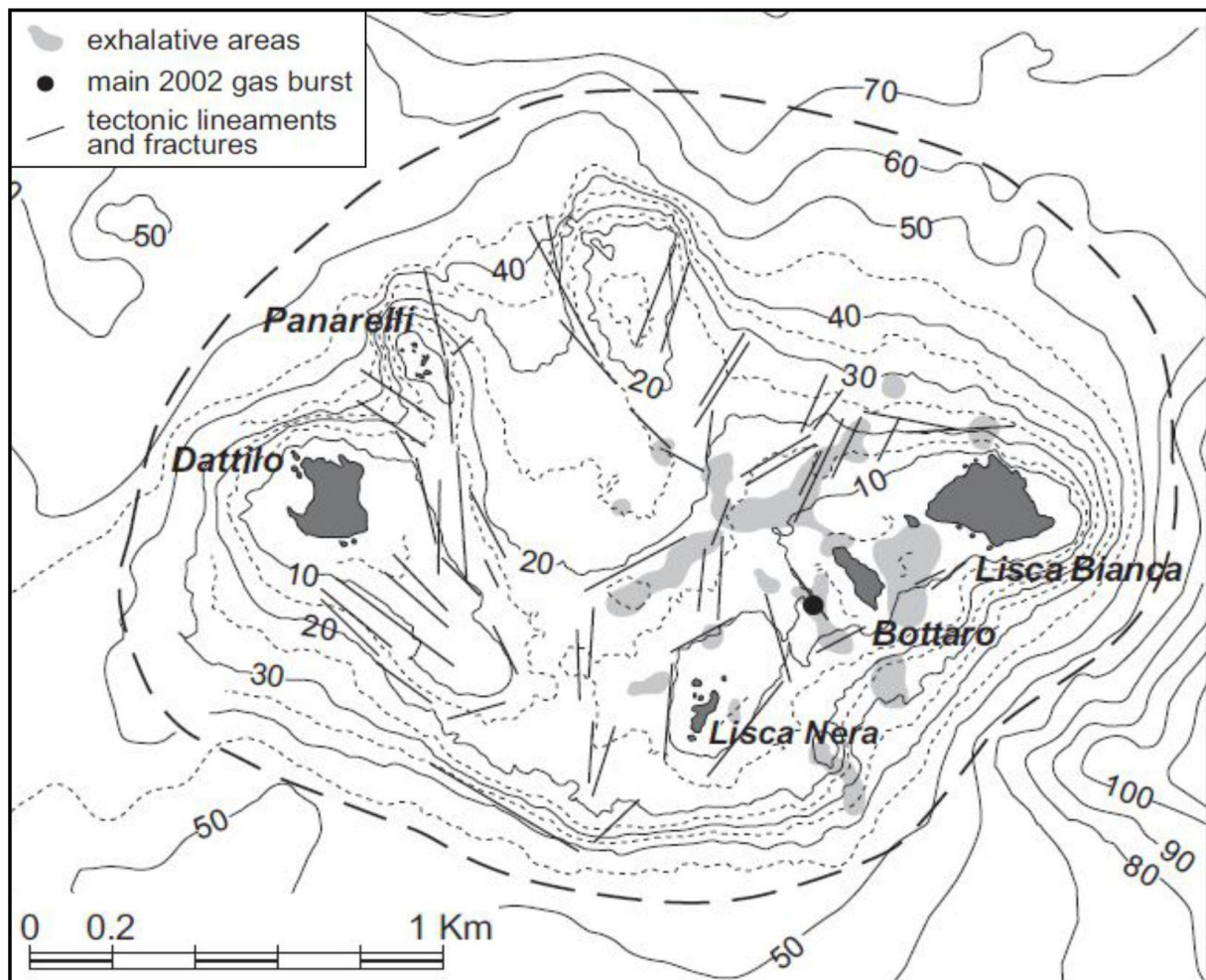
Fig. 6: *Structural features within the small islands in the east of Panarea (Lucchi et al., 2013).*

The major fault in this regional system extends from NNE to SSW. It is connected to the development of the volcanic belt to which Stromboli and Panarea also belong, together with its smaller islands (Esposito et al., 2010; Pohl et al., 2009). A second structural system, extending from NW to SE, controls the development of the volcanic dykes and their orientation (Lucchi et al., 2013). Additionally, numerous minor fractures, which follow the two main tectonic trends, are assumed to act as pathways for the fluid discharge that occurs in the area in form of several gas exhalations (fumaroles) and hydrothermal vents, known as fumarolic fields (Fig. 6). Due to the varying intensity of all those fumaroles in the investigation area, they were divided into five classes from A (weak) to E (very strong) with respect to their gas output rates (Steinbrückner, 2009). Further minor fractures are oriented perpendicular and 30° to the main tectonic trends, and feather joints occur.

2.3   Diving sites

The shallow-marine hydrothermal system of Panarea Island has been in the focus of geoscientific research for many years. The system is known as a natural field laboratory on a diversity of environmental issues such as ocean acidification and volcanic activity (Stanulla et al., 2017). Due to shallow water depths of up to 30 m, the location is reachable by scientific divers, and is well suited for different types of in-situ investigations.
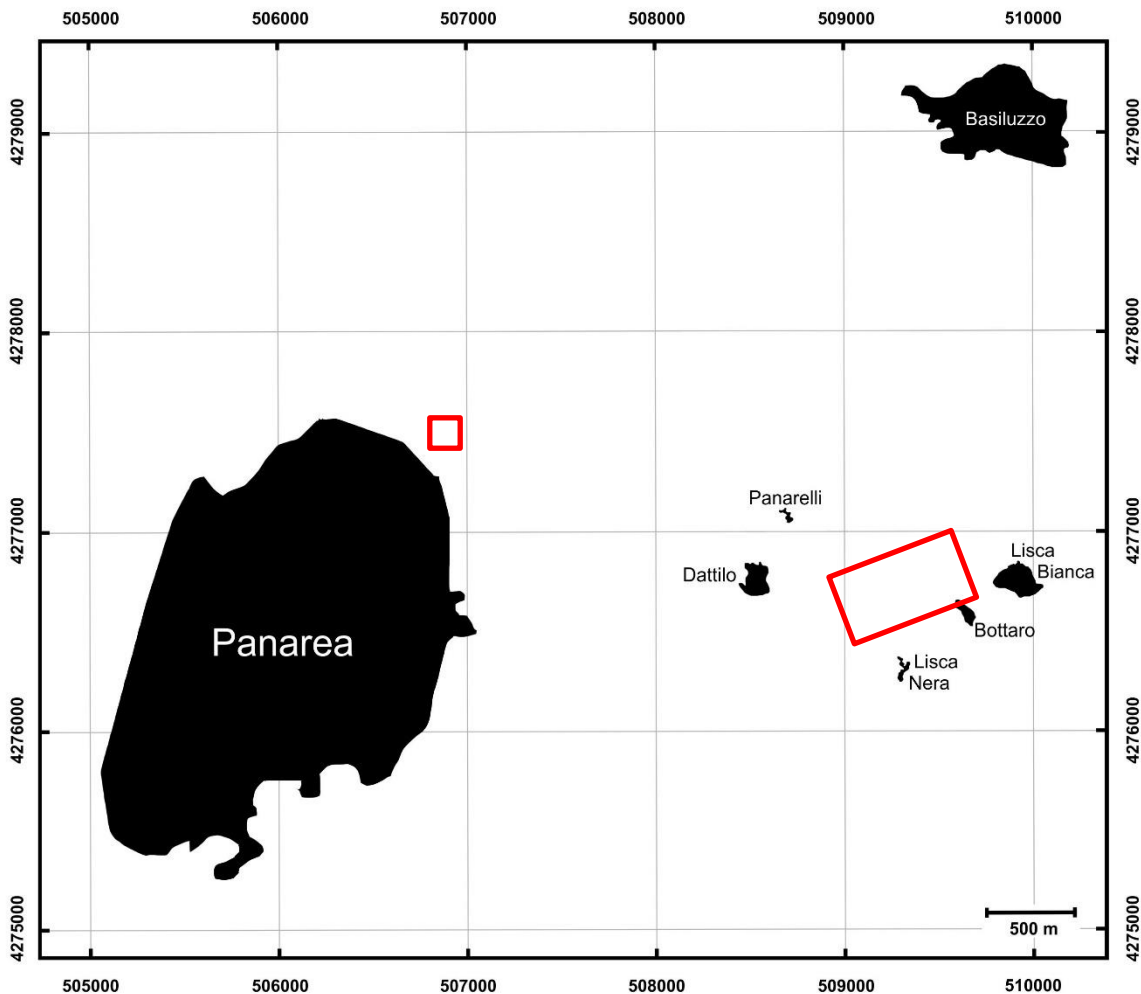
Fig. 7:   *Map of Panarea and its surrounding islets; the red squares indicate the location of the diving sites (coordinates are given in UTM WGS 84).*

Between the minor islands, which are located about 2.5 km to the east of Panarea, is a shallow plateau with maximum depths of 25 to 30 m. Primary volcanic features in this area are covered by a layer of volcanoclastic sediments. These sediments are suggested to be the result of the erosion of the surrounding lava domes and were deposited during the Last Glacial Maximum (Lucchi et al., 2013). The highest fumarolic activity is in this shallow area and minor exhalative areas are known in the NE of Panarea near La Calcara and around Basiluzzo.

A map of the different diving spots is shown in Fig. 8. Due to earlier studies it is known that Area 26, Black Point, and La Calcara are potential areas of interest in respect to precipitates and cements. Therefore, the following diving spots were chosen because of the knowledge about occurring precipitates gained in previous field trips.
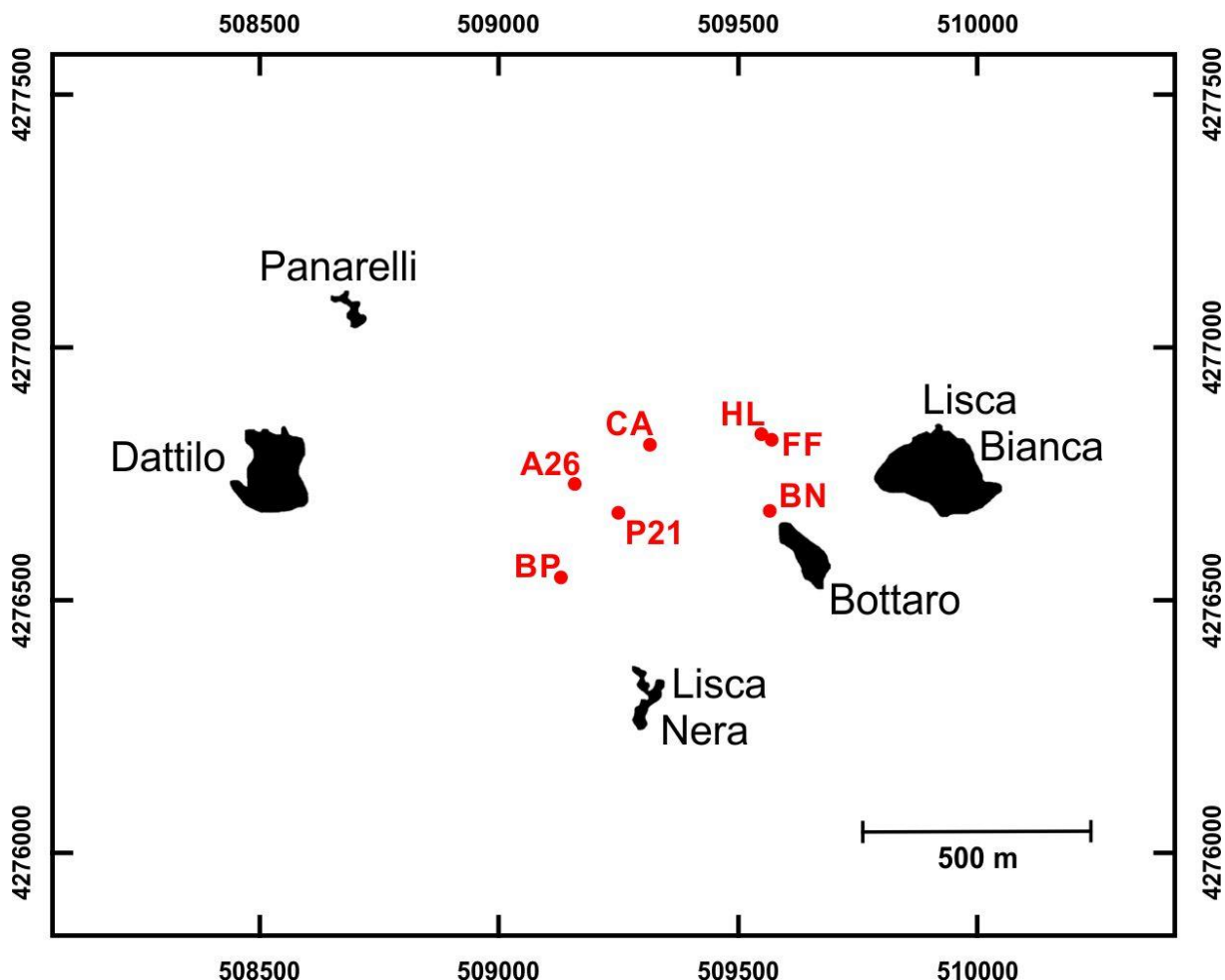
Fig. 8: *Simplified map of the islets in the east of Panarea and locations of the diving sites (coordinates are given in UTM WGS 84); A26 = Area 26, BN = Bottaro North, BP = Black Point, CA = Cave, FF = Fumarolic Field, HL = Hot Lake, P21 = Point 21.*

Area 26

The diving spot Area 26 (A26) is situated in the center of the small islands. With an average water depth of 26 m, it is the deepest diving spot at this plateau. The major type of sediment is a pyroclastic mass flow deposit with medium- to coarse-grained sand and clasts of gravel size. Sulfur cementation and precipitation, wide-spread and as filling of vertical openings, are common. Partly, ore sheets are found as loose plates covered with sediment. In respect to different types of mineral precipitates, significant locations are 'Mini Black Point', 'Brodor' and '3-bowls'. In 'Mini Black Point' sulfide ore mineralization takes place due to the emanation of H_2S and metal ion enriched fluids. 'Brodor' is a newly discovered location where sulfur

13

cemented cones and tubes are the main discharge features in consequence of gas emanations. The '3-bowl' feature is interpreted as concealed discharge structure indicating sulfur and sulfide cemented walls and is filled with recent sediments. Beneath these sediments at the bottom of the bowls alunite was found. Additional to the geological features, biological material plays a role as well. Posidonia growing in this area obviously stabilize the sediment and act as possible pathway for fluids.

Fig. 9: *Lineament structures with sulfur cemented walls (photo by R. Stanulla).*

Black Point

Black Point (BP) is a shallow marine gray smoker where sulfide ore minerals precipitate because of the contact of hot, mineral-rich water with the colder surrounding sea water (Fig. 10). Galena, sphalerite, pyrite/marcasite, and strontio-barite are the most common minerals (Becke, 2009). Black Point is located in the SSW of Area 26 and has a water depth of 24 m. The dynamic of the hydrothermal system is seen in the change of fluid composition through the years (Tassi et al., 2009). Until 2004, Black Point was a black vented smoker and during the first research diving expeditions from SDC Freiberg the chemistry of Black Point was very stable. Significant changes were observed in 2016 and 2017. Now, the emanated fluids are grayish in color with constant temperatures of ~130 °C (Dekov et al., 2013).
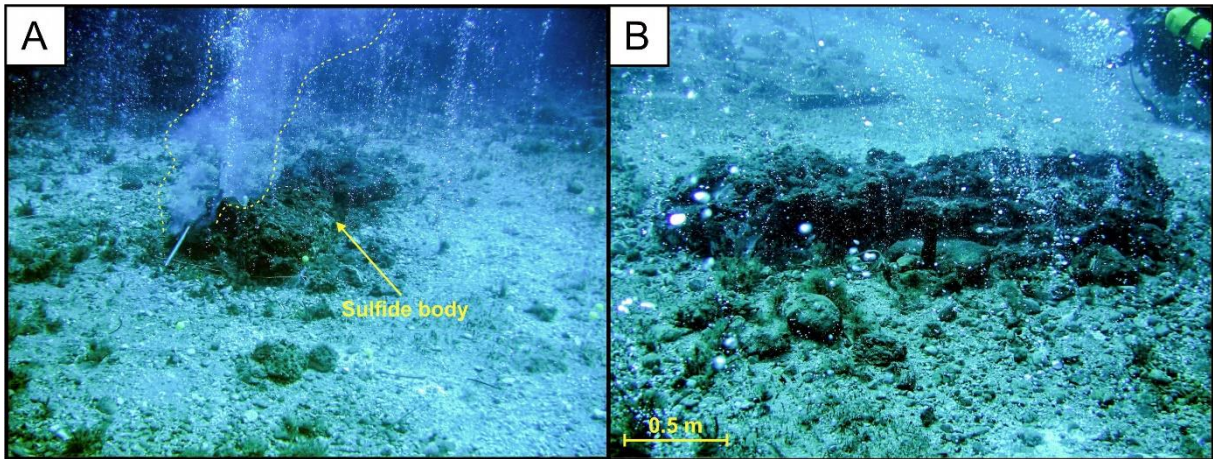
Fig. 10: Hill-shaped gray smoker (photos taken by T. Pohl in 2010); *A:* Inclined top view, smoke is marked by dashed lines; *B:* Sulfide body with 2.5 m in length, today it has a length of ~1.8 m because it was rip to pieces during a severe storm.

Bottaro North

As it is shown in Fig. 8, Bottaro North (BN) is the most proximal location to an islet of the investigation area. Big boulders cover the seafloor in consequence of landslides. The sediment is mainly composed of gravels cemented by sulfuric precipitations and weak to strong gas vents occur (Fig. 11). A thin sulfide coating is visible at some bigger clasts.
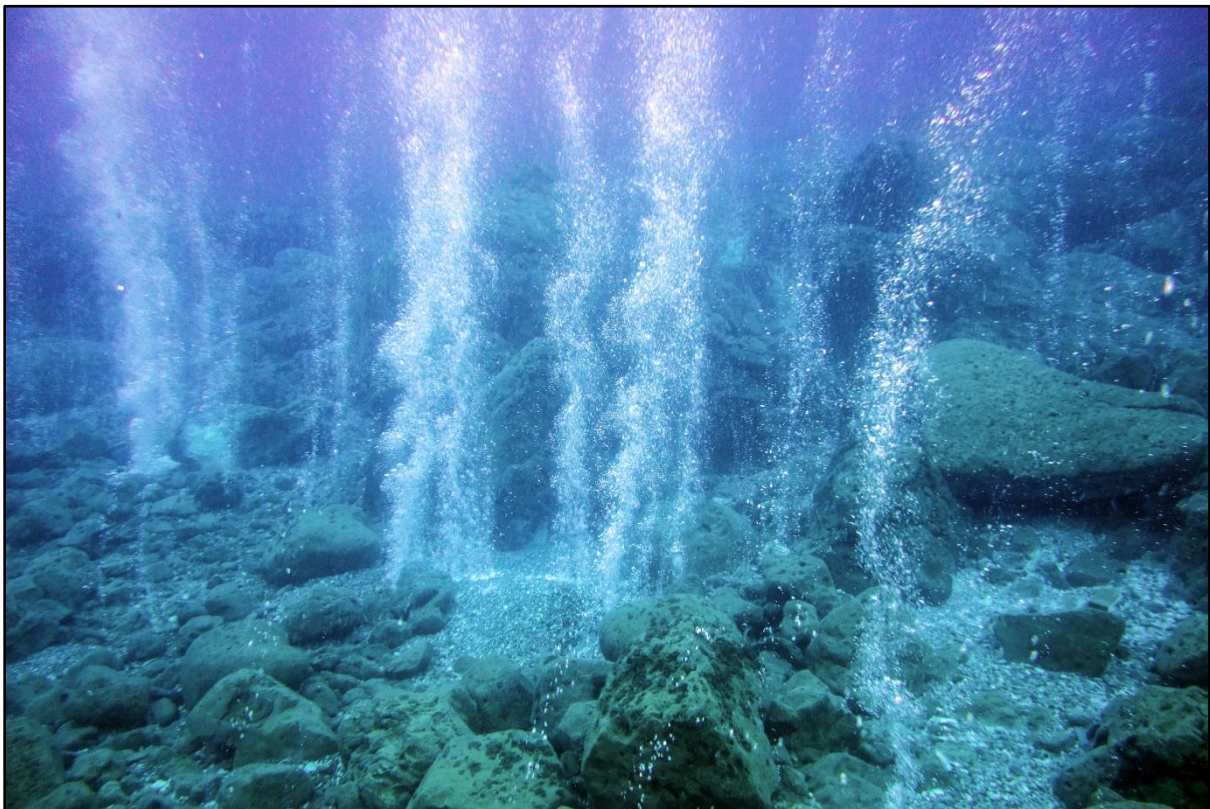
Fig. 11: Strong gas discharges (class A to C) at BN site (photo by R.Stanulla), big boulders up to 2-3 m in size.

Cave

In 2016, Cave (CA) was involved in the diving researches for the first time. It is situated in a water depth of 23 m and provides moderate exhalations. A conglomerate with fine crystalline sulfur as cement is found as sedimentary rock. Cave is a location characterized by a hollow structure where autotrophic and extremophile bacteria mats are residing, and sulfur precipitation takes place.
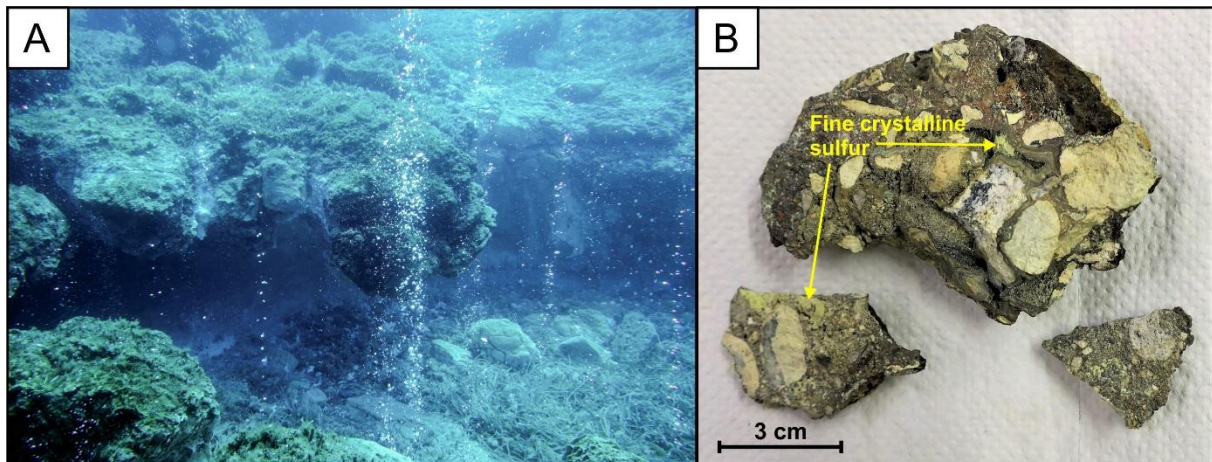
Fig. 12: **A:** *Cavity in the location CA with several gas vents and whitish bio mats (photo by R. Stanulla);* **B:** *Handpieces of the 'sulfur conglomerate' in CA, silicified areas and sulfide ore minerals around single clasts.*

Fumarolic Field

The sediment of Fumarolic Field (FF) is coarse grained, mainly gravel, and covers the entire ground of this location. Here in a water depth of 17 m, numerous weak gas emanations occur so that the sediment is affected by sulfur precipitation. The result is a sulfur cemented conglomerate as it is pictured in Fig. 13, B.
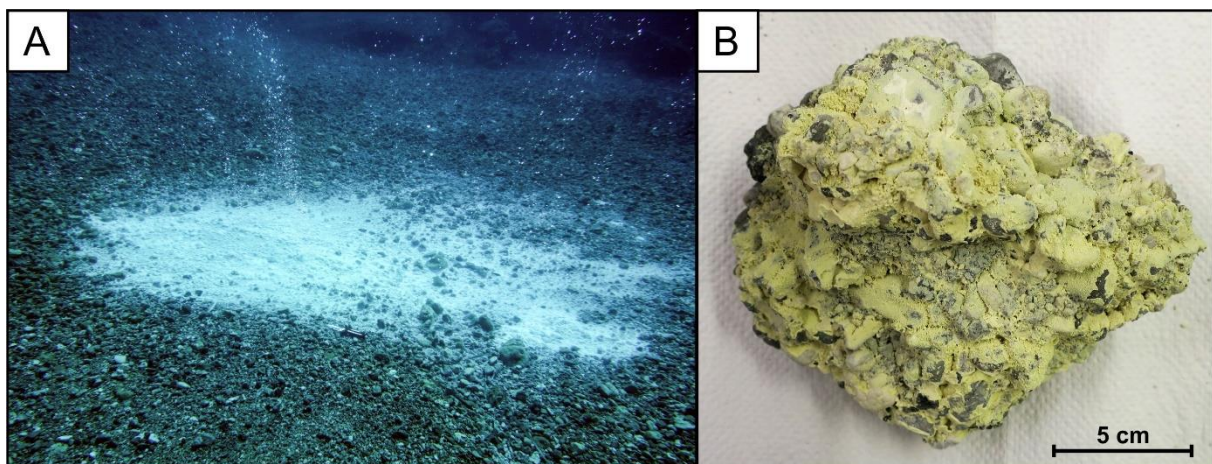
Fig. 13: **A:** *Sulfur cemented area of FF with minor (class A to B) gas vents (photo by R. Stanulla);* **B:** *Conglomerate with sulfur cement.*

Hot Lake

The diving spot Hot Lake (HL) is located next to Fumarolic Field at the NE side of the shallow plateau. Like the '3-bowls' in Area 26 but much greater, Hot Lake is a basin-shaped concealed discharge structure which comprises sulfur precipitates similar to those from Area 26 (Fig. 14). Since 2006, gas emanation was always very low. However, the amount of discharging water decreases over time and is close to zero since 2016. The sediments of this site mainly consist of tuffs with clay lenses in between which are called 'dragon eggs' due to their ovate shape.
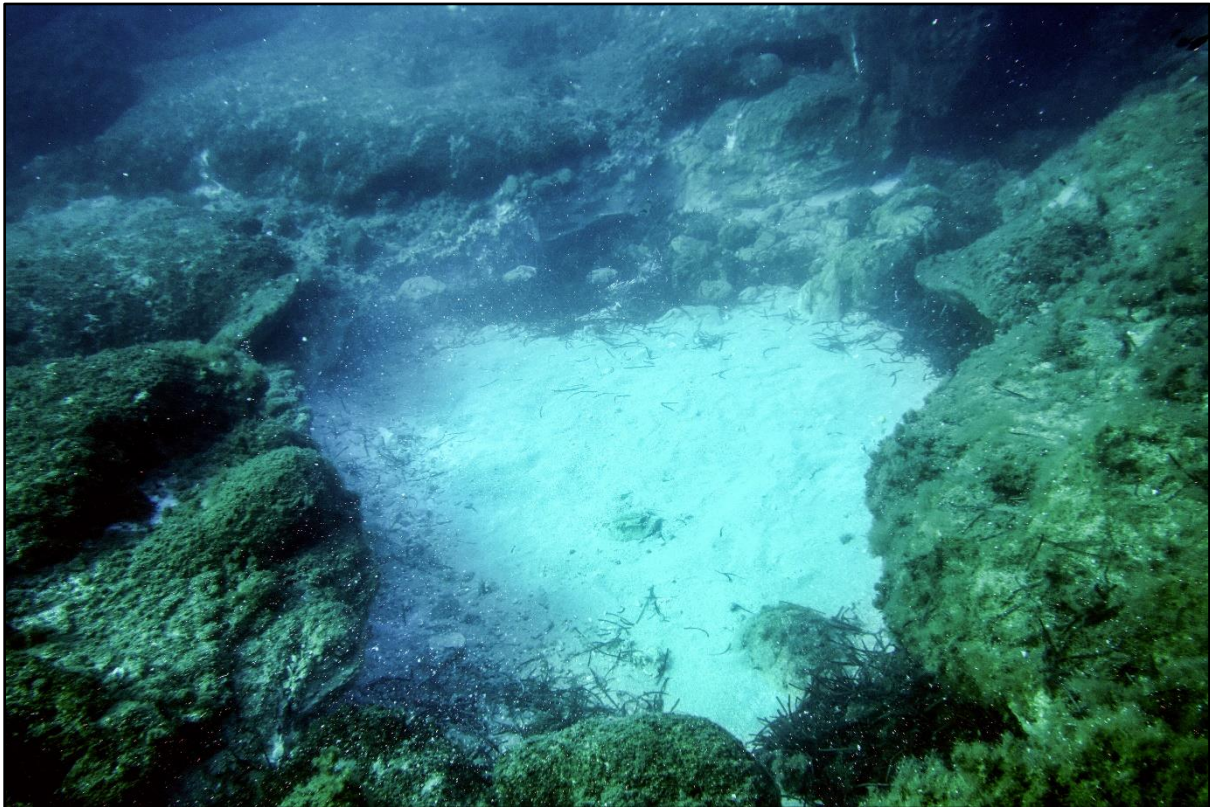
Fig. 14: *Basin-shaped structure of HL filled with sediment (photo by R. Stanulla).*

La Calcara

Next to Panarea in the NE of the island the location La Calcara (LC) is in a depth of 23 m below sea level. Recent medium- to coarse-grained, relatively well-rounded sands cover gray clays which are probably widely distributed, i.e. alunite (Prautsch et al., 2013). Previous investigations in this area have documented the existence of Mg-rich rhodochrosite [$MnCO_3$] which is unlikely in such a milieu because of the instability of carbonates in reducing environments (Kakuk, 2016). Iron(hydr)-oxide precipitations occur in sediment cemented tubes near 'Black Rock' (Fig. 15). Pyrite and marcasite occur as disseminated, sediment-hosted ore aggregates wherever gas or water are emitted from the sea floor occur or as ore sheets and crusts adjacent to and at 'Black Rock'.

Fig. 15: *'Black Rock' in LC with minor (class A to B) gas discharges (photo by R. Stanulla).*

Point 21

In Point 21 (P21), dacite is found as bedrock. This volcanic rock is characterized by a scarp-wall of about 5 m in height which is traversed by fissures. This location is probably a crossing of two faults, thus the scarp represents likely one fault. The volcanic rock is highly altered because of five very strong (class E), continuous gas vents and minor ones (class A to C) in the vicinity. White bio mats and extreme sulfur precipitation are common wherever stronger gas and water discharges occur (Fig. 16).

Fig. 16: Steep scarp of altered dacite (in the background) and two strong gas vents with sulfur precipitation (in the foreground). Photo by R. Stanulla.

3 Methods

This thesis is focused on the relationship between the fluid emanations and the hydrothermal precipitation and cementation. Hence, it is important to figure out at which environmental conditions, e.g. pH-value, water temperature, and redox potential, previously mentioned minerals precipitate around the Panarea island. Rocks and mineral precipitates were sampled with hammer and chisel and stored in transport boxes or sampling bags. Due to the possible oxidation of certain minerals like pyrite, a technique for sampling and handling under protective atmosphere with nitrogen was developed. To identify the composition of minerals, polarizing microscopy, Micro X-ray Diffraction (µXRD), and Scanning Electron Microscopy with Energy Dispersive X-ray Analysis (SEM-EDX) were used.

3.1 Field work

The cements and precipitates which were formed in the submarine area around Panarea mostly develop in reducing environments. If those precipitates get exposed to ambient air or oxygenated water, oxidation takes place and changes may occur in some properties of distinct mineral phases. To analyze these processes and consequent mineral alteration, a comparison of normally taken samples with unaffected ones is necessary and possible because of working under protective atmosphere. In this case, nitrogen is used because it is an inert, inexpensive, harmless gas, ensuring safe handling.

3.1.1 Preparation for sampling with nitrogen

Deionized water was purged with nitrogen to eliminate oxygen and subsequently filled in a 450 ml syringe with a three-way-valve.

Two sampling bags were used. One to hold the sample in the protective atmosphere, the other to hold the inflated sample bag acting as backup. Cable ties were used to close these bags to prevent escaping of nitrogen. However, the sampling bags were not closed completely to allow degassing during ascending.

The nitrogen tank (1.5 l in volume), prepared with an inflator hose and a nozzle, was attached to the lifting bag with a short rope (fixing knot = Webeleinstek) and a carbine. An elastic band was used to fixate the inflator hose to the nitrogen tank. Furthermore, two sampling nets, one for the samples, the other one for the materials (the water-filled syringe, cable ties, and the labeled sampling bags) were fastened, each one with a carbine, to the lifting bag; also attached: a hammer and a chisel for the direct (rock) sampling under water.

Lead weights were used as counterbalance for the nitrogen filled sampling bags. According to the Boyle-Mariotte law ($p \cdot V = $ constant), volume increases with decreasing pressure. The buoyancy (F_A) of the sampling bags had to be in equilibrium with the weight force (F_G) of the nitrogen and the lead at the sea surface to inhibit a fast ascending. The amount of lead by weight can be calculated as in the following example:

Example: Sampling at 20 m water depth in the Mediterranean Sea;
1.5 l nitrogen in one bag

Given: $\rho_{N_2} = 1.25 \frac{g}{l}$ $p_1 = 3 \, bar$

$\rho_f = 1025 \frac{g}{l}$ $p_2 = 1 \, bar$

$V_{N_2} = 1.5 \, l$

Searched: m_{Pb}

1. $p_1V_1 = p_2V_2$ → $\frac{p_1V_1}{p_2} = V_2$

$$\frac{3 \, bar \cdot 1.5 \, l}{1 \, bar} = 4.5 \, l$$

2. $F_A = F_G(N_2 + Pb)$ → $\rho_f V_2 g = g(\rho_{N_2}V_2 + m_{Pb})$

$$V_2(\rho_f - \rho_{N_2}) = m_{Pb}$$

$$4.5 \, l \left(1025 \frac{g}{l} - 1.25 \frac{g}{l}\right) = 5770 \, g = \mathbf{5.77 \, kg}$$

As previously mentioned, degassing occurs due to the partial opening of the cable tie, so the nitrogen filled sampling bags will have approximately the same volume at the sea surface as at depth. Therefore, it applies:

3. $V_2(\rho_f - \rho_{N_2}) = m_{Pb}$

$$1.5 \, l \left(1025 \frac{g}{l} - 1.25 \frac{g}{l}\right) = 1540 \, g = \mathbf{1.54 \, kg}$$

Hence, for one sample a weight of 1.54 kg lead is needed to balance the buoyancy. As backup it is better to take along 2 kg of lead because the volume and the buoyancy of the lifting bag have to be considered.

3.1.2 Sampling under N$_2$ protection

Each sample, taken with hammer and chisel, was put in a sampling bag and fixed with a cable tie, but left half open. The bag was filled with nitrogen. Afterwards, the sample was cleaned with purged deionized water to remove possible salt remains of the Mediterranean sea water. The sampling bag had to be refilled and purged again with nitrogen (Fig. 17). Now the cable tie was closed completely. Another bag was put over the bag with the sample, was filled with nitrogen, and closed with a second cable tie. A short video of sampling with nitrogen under water is available in the appendix. All samples taken under protective atmosphere will be referred to as N$_2$-samples.
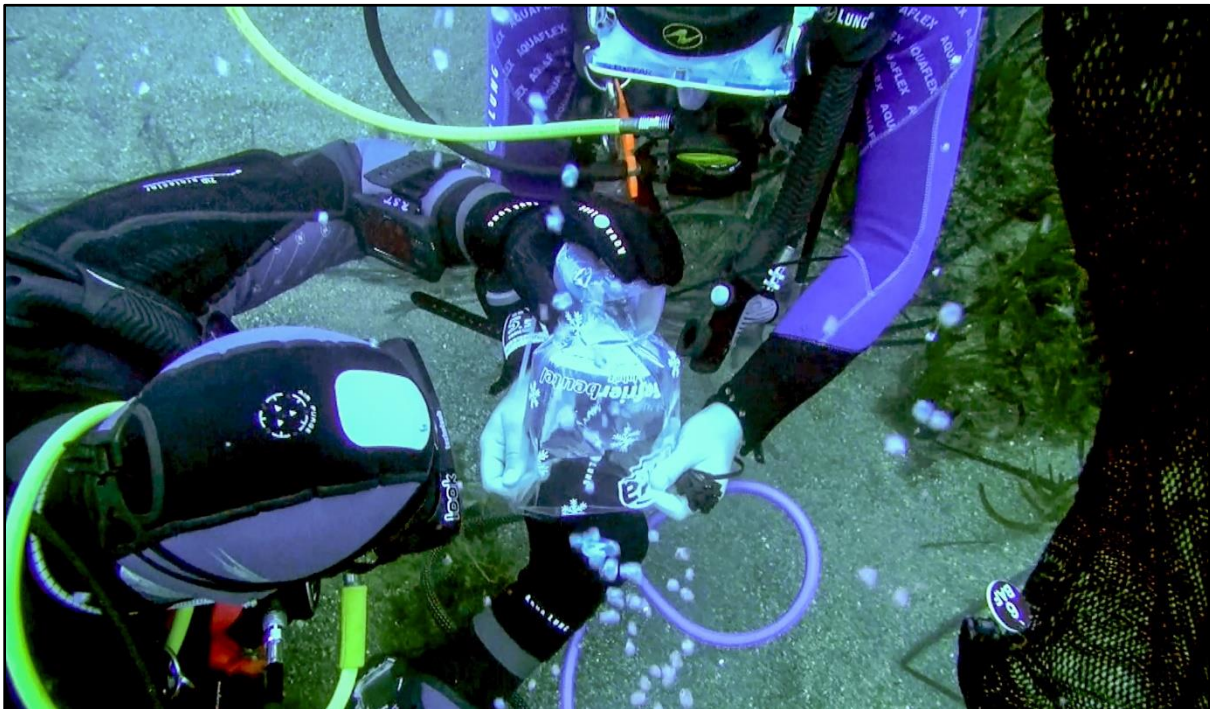
Fig. 17: *Sampling under water - filling of the half-closed sampling bag with nitrogen (photo by S. Kluge).*

3.2   Laboratory work

3.2.1   Handling of the N$_2$-samples

For further processing and safe storage of the samples taken under protective atmosphere, a mobile glovebox (*SPILFYER* "Hand-in-bag" No. 690323, 39"W x 48"L) was used. In the box, the items were required which are listed in Tab. 1 (Fig. 18):

Tab. 1: *Sampling tools and application*

Sampling tools	Reason of use
N_2-samples	had to be put in gas- and waterproofed boxes
new sampling bags	for clean and dry wrapping
cable ties	for closing the sampling bags
gas- and waterproofed boxes	used for transport and storage of samples
pair of scissors	to open 'old' sampling (plastic) bags
a bowl with salt	to keep samples dry and eliminate moisture
deoxygenized, deionized water	samples had to be cleaned again
packing material (tissue)	protection of the samples
camera and a ruler	first photo documentation

Fig. 18: *In the field laboratory: mobile glovebox equipped with material.*

An inflator hose and a three-way-valve as regulator for overpressure were connected to the glovebox. Both inlets were sealed with tapes and after that, the box was filled with the above-mentioned materials. The packing material, the boxes, all the new sampling bags, and the entire glovebox had to be purged with nitrogen. The box was sealed then with a special tape and again filled with N_2 (total usage: ~ 1300 L), but still with open valve because the

remaining oxygen had to be replaced. Only when the valve was closed and the box was filled completely with nitrogen, the samples were taken out of their bags, were cleaned with purged water and documented by photos. After 16 hours drying (overnight), the samples were photographed again and put in the new bags (with labeling). Cable ties were used to close them, and the repacked N_2-samples were stored in the click-boxes.

3.2.2 Microscopy

A suitable approach for the identification of the distinct precipitates is optical, particularly reflected-light microscopy with respect to ore minerals. Therefore, thin and polished sections of some selected samples were produced in the rock preparation laboratory of the Helmholtz Institute in Freiberg under the direction of Andreas Bartzsch. According to the considering mineral precipitates, section positions of selected samples were decided beforehand so that the samples could be analyzed for sedimentological features and mineral identification under the microscope and with SEM-EDX.

To answer the question of the relationship between the emanated hydrothermal fluid and the mineral precipitation, geochemical and mineralogical analyses are necessary. Samples from previous field trips were checked for relevance and were included in the investigations. To determine the distinct mineral precipitates polarizing microscopy is a suitable method. Structural and sedimentological features carrying information on the mineral genesis can also be investigated via optical microscopy. In addition, reflected-light microscopy is commonly used for the determination of opaque minerals, especially ore minerals. For this purpose, anisotropic effects reveal useful information.

Optical anisotropy is an effect based on the atomic arrangement in a crystal, mineral or other material. It occurs when materials either reflect or transmit light in different directions with different velocities (Leng, 2013). Only the cubic crystal structure, also known as isotropic, exhibits the same properties in all directions, thus, most minerals and materials show anisotropic effects.

Light has wave properties and vibrates in every direction perpendicular to its propagation direction. A polarizer is used to change the direction of vibration if light passes through it. As a result, polarized light vibrates in planes different from the incident plane. A second polarizing filter, called analyzer, is arranged with a variance of 90° to the polarizer to create a crossed position that only allows plane-polarized light to transmitted (Leng, 2013).

For reflected-light microscopy it means that anisotropic minerals can show variances in color or brightness when the polarized light waves change their orientation in respect to the crystal structure while isotropic materials cannot change the orientation of polarizing light and will be extinguished.

An appropriate example for this application is the distinction between pyrite and marcasite because both minerals have identical chemical composition, but different crystal structures.

For high-resolution images of each thin section, single pictures (image tiles) were taken by scanning the thin section and were stitched together. These MOSAIX pictures were made by Dr. Michael Magnus from the TU Bergakademie Freiberg. A *ZEISS Discovery V12* stereomicroscope with a microscope camera *AxioCam MRc5* was used for this purpose. Additionally required was the image analysis software *AxioVision* from *ZEISS*, especially the MOSAIX-module. All the other pictures and detail images (transmitted- and reflected-light) were taken with a *LEICA DMRX* microscope of the Institute of Geosciences at the University Bremen. A *LEICA DFC320* microscope camera and the software *Leica Application Suite (Version 2.8.1)* were used.

3.2.3 Micro X-ray Diffraction

The micro X-ray Diffraction (µXRD) is a non-destructive, analytical technique used for the assignment of the crystal structure of a mineral. The knowledge about the possible or expected chemical composition were obtained from appropriate sample material from previous field trips and water chemistry data allowing a pre-selection of possible minerals to be made.

For the analysis of the N_2-samples a protective atmosphere was needed to avoid any contact with ambient air. A purpose-built, small air-tight box was able to be used for the µXRD. For that reason and from a financial point of view, µXRD was preferentially used for the N_2-samples.
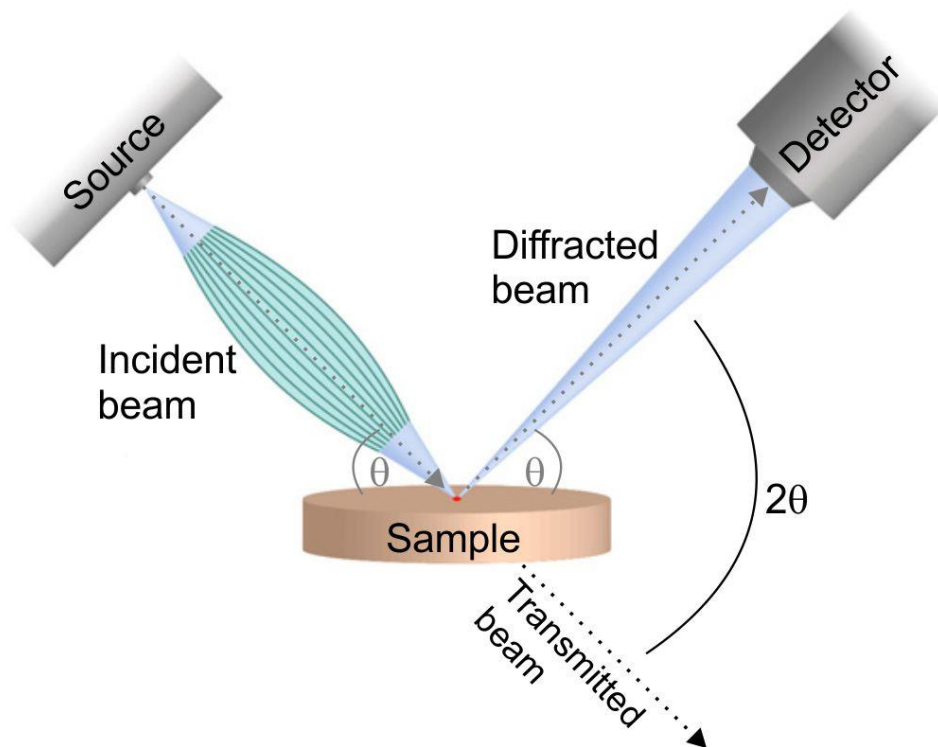
**Fig. 19:** *Arrangement of the µXRD analysis (modified after Anon., access date 08/09/2018).*

In Fig. 19, a simplified illustration of the µXRD analysis is shown. A Montel mirror arrangement is used to direct X-rays as a narrow beam at the sample. A *BRUKER axs D8-II DISCOVER Diffractometer* with an *Incoatec IµS Co* tube in the institute for Energy Process Engineering and Chemical Engineering of TU Bergakademie Freiberg was used with the help of Dr. Marcus Schreiner. At the surface of a sample, the X-ray beam is scattered with the same wavelength as the incoming beam. The diffraction patterns are a consequence of the spatial, atomic distribution and intensities of scattered X-rays and are uniquely defined by the crystal structure (He, 2004).

Bragg's law is used to describe X-ray diffraction of crystals in a wimple manner. X-rays hit the sample surface with an angle θ [theta] which is equal to the diffracted angle (He, 2004). The Bragg's law is an expression of the wavelength λ of the X-rays, the order of diffraction n as an integer, the Bragg angle θ and d as the distance between two adjacent crystal planes:

$$n\lambda = 2d\ sin\theta$$

The diameter of the X-ray beam from the named diffractometer amounts to 700 µm. At the surface of the sample, the beam is diffracted and measured with a detector. If the Bragg condition is compiled, a diffractogram is created that shows several diffraction peaks as impulses at angles of *2θ* (Fig. 20).
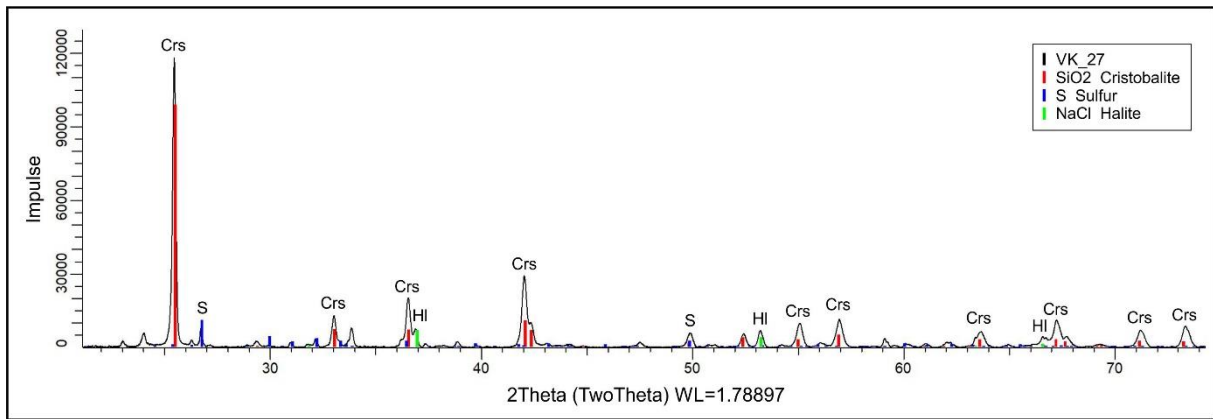
Fig. 20: *Diffractogram of the sample VK_27 from the location P21.*

The µXRD results have to be critically evaluated because the peaks of a diffractogram are correlated with distinct crystal structures, not with the mineral itself. Therefore, the identification of a certain mineral is only possible with additional information about the chemical composition. Hence, it is necessary to have a rough idea which elements likely occur. Finally, each peak with its position, width, and intensity can refer to a mineral by comparing the diffractogram to known diffraction angles and intensities of mineral phases. The software *Bruker GADDS* and *Bruker EVA* were used together with the data base *ICDD PDF-2*.

3.2.4 SEM-EDX

The Scanning Electron Microscopy with Energy Dispersive X-ray Analysis (SEM-EDX) is a non-destructive technique. It is used for quantitative information about the geochemical composition of a sample and to provide the elemental identification. Furthermore, morphological features up to nm-scale can be visualized which is useful for mineral shapes and crystals. A primary electron beam allows a high spatial resolution because it can be focused to a very small area. The EDX analysis records the elements ranging from beryllium to the radioactive elements in percent by mass. Considering that the samples were covered by carbon, thus, some measurements show a higher carbon content. The SEM-EDX measurements were supported by Mrs. Anja Obst from the TU Bergakademie Freiberg. A *Bruker Nano (GmbH, Germany; Quantax) Scanning Electron Microscope* was used.

3.3   Fluid data

A team of the Scientific Diving Center took fluid samples and temperature readings from all locations, determined the field parameters (pH-value, redox potential, electric conductivity, O_2-content, sulfide, and Fe^{2+}) and prepared the samples for the shipment to the laboratory. In Freiberg, the main anions and cations of these samples were analyzed with an ion chromatograph (IC; *Metrohm*). The carbon content (HCO_3^- and CO_2) was determined as total inorganic carbon (TIC) by use of a nondispersive infrared sensor (NDIR). All the other elements like alkali or alkaline earth metals were measured with an Inductively Coupled Plasma - Mass Spectrometry (ICP-MS; *Thermo Element2*). The calculations of possible mineral precipitations from fluids by means of the saturation index (SI) were executed with the computer programs PHREEQC and EQ3/6. These programs are useful to verify the plausibility of occurring precipitates at given pH-values, pressures, and temperatures. However, results have been handled with care, because the element concentrations were measured after secondary minerals have already started to precipitate. Thus, the measured concentration is depleted in those elements that are transitioned into the precipitates.

Extreme values from previous expeditions and current data were used (attached in Tab. 12) in combination with geochemical data in the data base *minteq.v4.dat* and the *LLNL* data base developed for EQ3/6.

4   Results

The distinction of several minerals is possible due to their varying chemical composition, expressed as the percentage of element contents. Chemical formulas, known mineral compositions and the variation in element contents of specific minerals were selected from literature and online data bases. In the appendix an EXCEL file of the analyzed minerals, their chemical composition, and threshold values of their element content is attached (Appendix: Tab. 15). Furthermore, in this thesis the optical properties such as color and anisotropy of the minerals named below were examined under a microscope using reflected light.

The cements and mineral precipitates occurring around Panarea and the surrounding islets can be divided into four types: (1) sulfide and sulfate minerals, (2) iron-oxides and -hydroxides, (3) elemental sulfur, and (4) manganese precipitates mainly as coating of gravels. Additionally, clay as hydrothermal alteration product occurs. Therefore, existing sample material and its results could be used and were included to further research.

All types of the named precipitates were found in the entire area of investigation where the discharge of hydrothermal fluids occurs. Sulfuric cementation and precipitation are to be found almost everywhere where minor or massive fluid discharges appear: in Area 26, Bottaro North, Cave, Fumarolic Field, La Calcara and Point 21. Iron(hydr)-oxide cementation is merely found forming tubes near 'Black Rock', Basiluzzo, in patches in 'Mordor' (La Calcara) and as crust in Point 21. For the first time, iron precipitates were also found in cones of the discharge formation 'Brodor' of Area 26. Sulfide minerals are represented by pyrite, marcasite, galena and sphalerite. Pyrite/marcasite are predominantly found in Area 26, Black Point, and La Calcara whereas the mineralization of galena and sphalerite is restricted to Black Point and less at 'Mini Black Point' in Area 26. The methods mentioned in this thesis, namely light microscopy, µXRD and SEM-EDX, indicate the precipitation of marcasite, pyrite and, in higher concentration, galena and sphalerite at this site.

4.1 Sulfide and sulfate minerals

4.1.1 Pyrite and marcasite

The appearance of marcasite [Mrc] and especially pyrite [Py] varies from location to location. The distinction between pyrite and marcasite is problematic as both minerals have an identical chemical composition, thus a differentiation with chemical analysis methods is almost impossible. However, a distinguishing feature of the named sulfides is the optical anisotropy being based upon the atomic arrangement in a mineral. Pyrite belongs to the cubic crystal system therefore it is isotropic. In contrast, marcasite crystallizes in the orthorhombic system. It shows a very strong anisotropism which changes from yellow through pale green to dark green while pyrite is extinct under crossed polarized light or may show a slight dark green to blue anisotropism.

In La Calcara the main precipitated mineral is marcasite. Examined under reflected-light this mineral phase often shows an iridescent tarnish which is a common feature of marcasite. Using acetone or repolishing the thin section, this tarnish usually can be removed and a fresh surface with a tin-white color is generated (Fig. 21). This was done with some of the thin and polished sections for the illustration of fresh, unaltered samples, but due to the time limitation it was not possible for all samples.
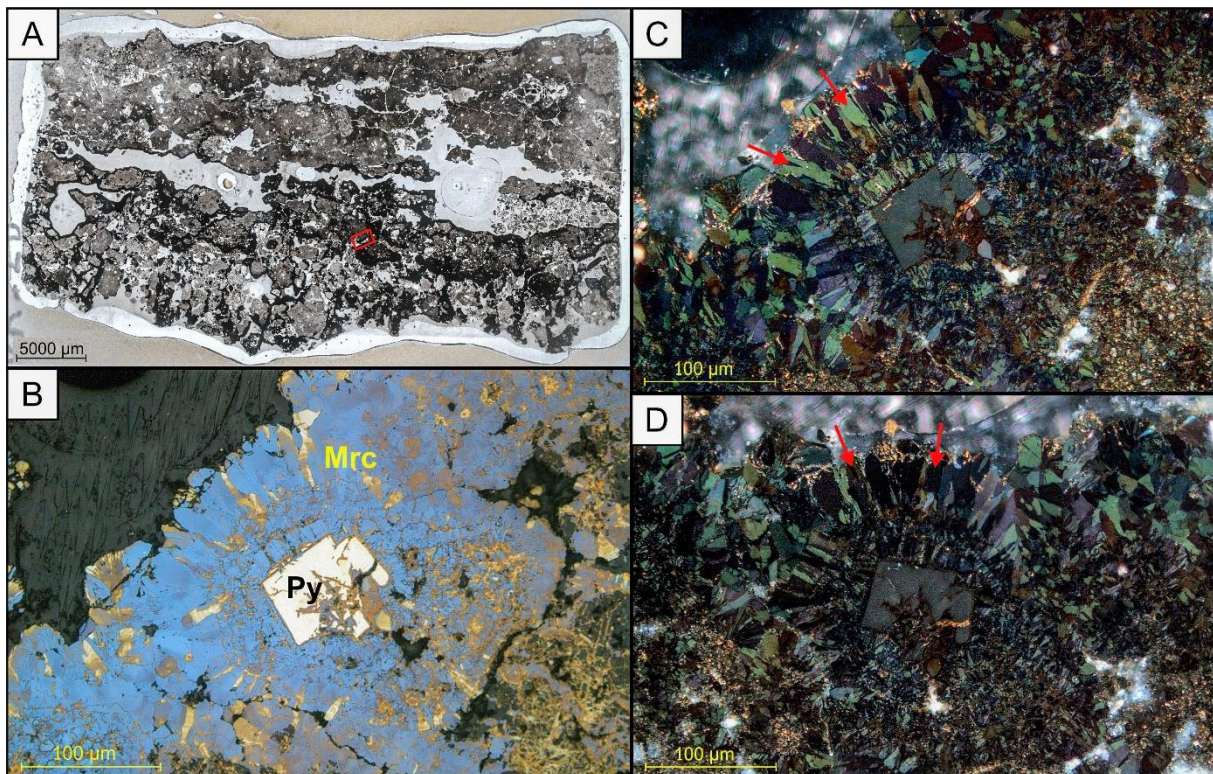
Fig. 21: *Thin section VK_20 from LC – 'New Rock'; **A:** Survey of entire thin section (transmitted light, ll-pol), the red rectangle denotes the image detail; **B:** Well-formed pyrite crystal surrounded by iridescent-colored marcasite (reflected light, ll-pol); **C:** Same image detail as B, but with crossed polarizers; red arrows pointed to marcasite crystals; **D:** Same image detail as C, but with 45° clockwise-turned stage; color change of the pointed marcasite crystals and therefore the anisotropic effect is seen, pyrite shows just a very slight variation in color.*

Marcasite is more susceptible to tarnishes than pyrite and darkened on exposure to oxygen, but pyrite can show such iridescent colors as well. In thin or polished sections, the distinctive color of marcasite is often a pale yellow or creamy white which is similar to pyrite. The anisotropy, however, enables the distinction of these minerals as above mentioned.

Marcasite crystalizes in typical cockscomb and sheaf-like shapes as it is shown in Fig. 21 and 22. Spherulitic textures and twin slats in radial orientation are also common crystal forms for this mineral. Only pyrite occurs in patches as well-formed, cubic grains in some of the radial-oriented marcasite crystals.
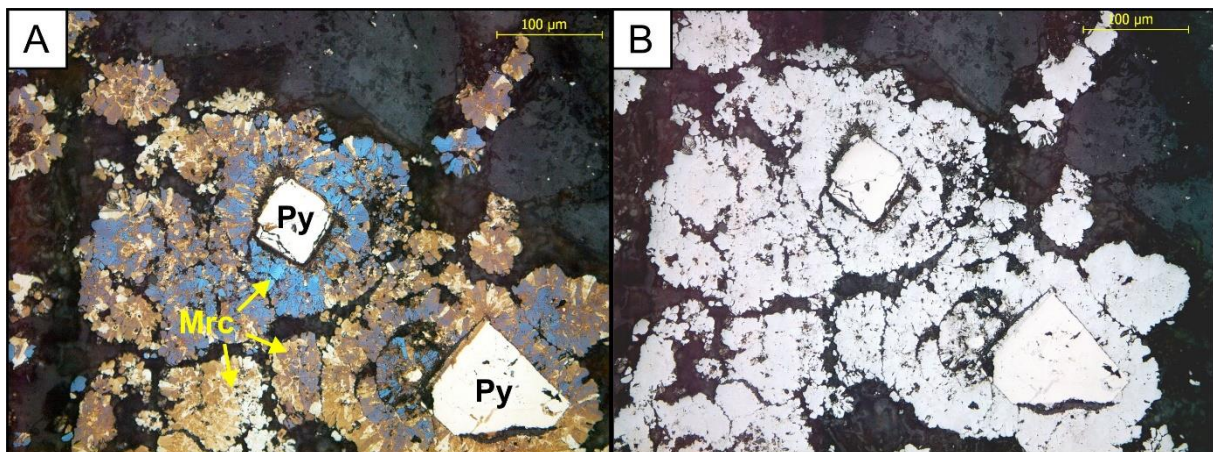

Fig. 22: Image detail of thin section VK_20 from LC, well-formed, cubic pyrite crystals surrounded by radial-oriented aggregates of marcasite (reflected light, ll-pol); *A:* Pyrite with its typical pale yellow color, marcasite shows an extreme iridescent tarnish; *B:* After repolishing: the color of pyrite did not change, but marcasite has now a tin-white color due to the freshly generated surface.

In the thin section VK_05 the distinction between pyrite and marcasite is obvious. Homogeneous, creamy-whitish precipitates as crusts around single grains are pyrite whereas marcasite shows its typical iridescent tarnish. This was verified by use of anisotropy. Considering marcasite, color changes from pale to dark green are observable while turning the stage (Fig. 23).

Pyrite was not identified with reflected-light microscopy at Black Point. Marcasite merely occurs as component of the mineral crust at this location as pictured in Fig. 24.
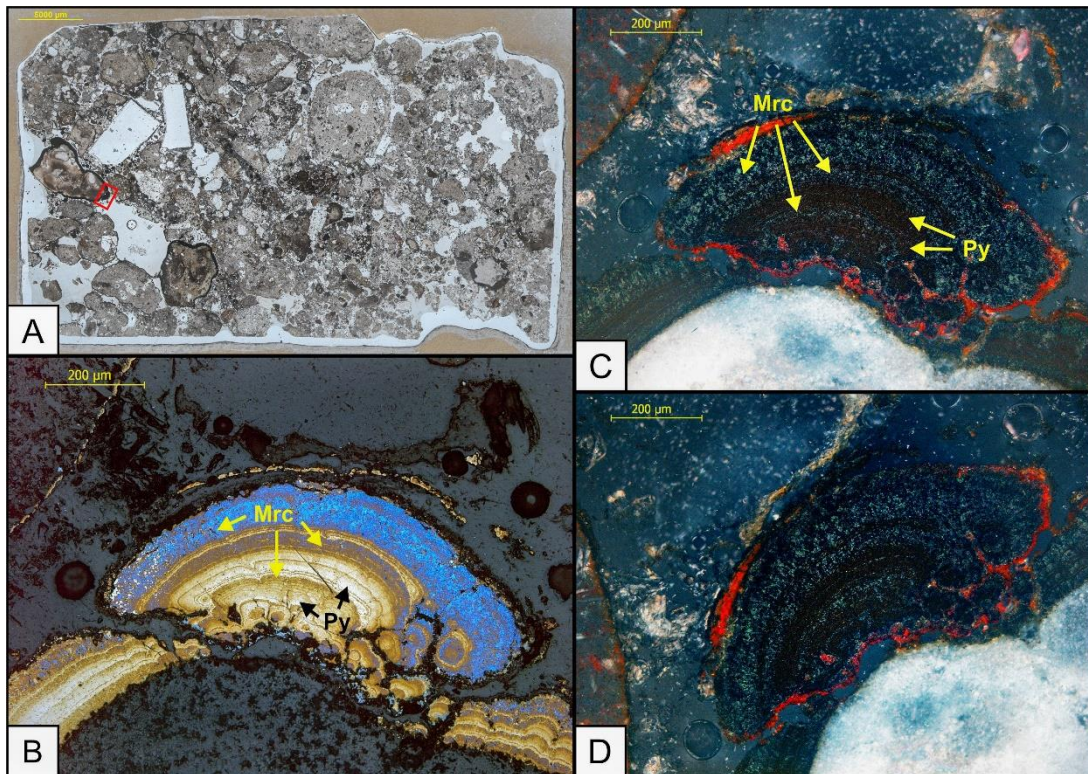
Fig. 23: *Thin section VK_05 from LC; **A:** Survey of entire thin section (transmitted light, ll-pol), the red rectangle denotes the image detail; **B:** Pyrite (pale, but distinctly yellow) with iridescent-colored marcasite as alternate layers (reflected light, ll-pol); **C:** Same image detail as B, but with crossed polarizers; **D:** Same image detail as C, but with 45° anticlockwise-turned stage; color change of marcasite crystals and therefore the anisotropic effect is seen, pyrite remains extinct.*
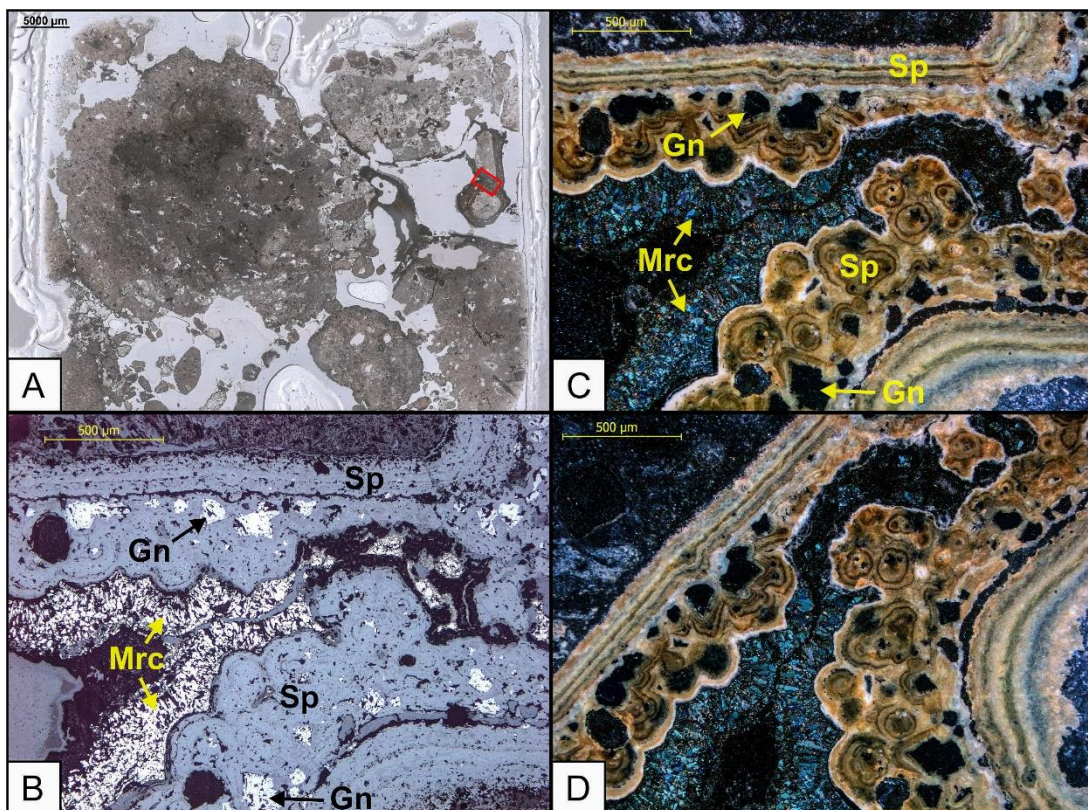

Fig. 24: *Thin section BP2 from BP; **A:** Survey of entire thin section (transmitted light, ll-pol); **B:** Well-formed galena crystals (gray-white) surrounded by sphalerite (gray) and marcasite at the outer part (reflected light, ll-pol); **C:** Same image detail as B, but with crossed polarizers; galena extinct, sphalerite occurs in botryoidal faces with layered appearance; **D:** Same image detail as C, but with 45° anticlockwise-turned stage; marcasite shows strong anisotropism ranging from pale green to bluish colors.*

32

The mineral phases were analyzed by µXRD and SEM-EDX. Both diffractograms of the samples VK_03_N$_2$ and VK_05 from La Calcara confirm the presence of pyrite and marcasite (Fig. 25 and 26). These two samples were chosen to compare a sample taken under normal conditions with a N$_2$-sample. Comparing the two sampling methods it was assumed that the samples handled under normal conditions show distinct differences in the mineralogy due to obvious changes in color and luster. It was presumed to be a result of the oxidation of the diverse minerals while being exposed to air or ambient sea water (O$_2$-enriched relative to the fluids).
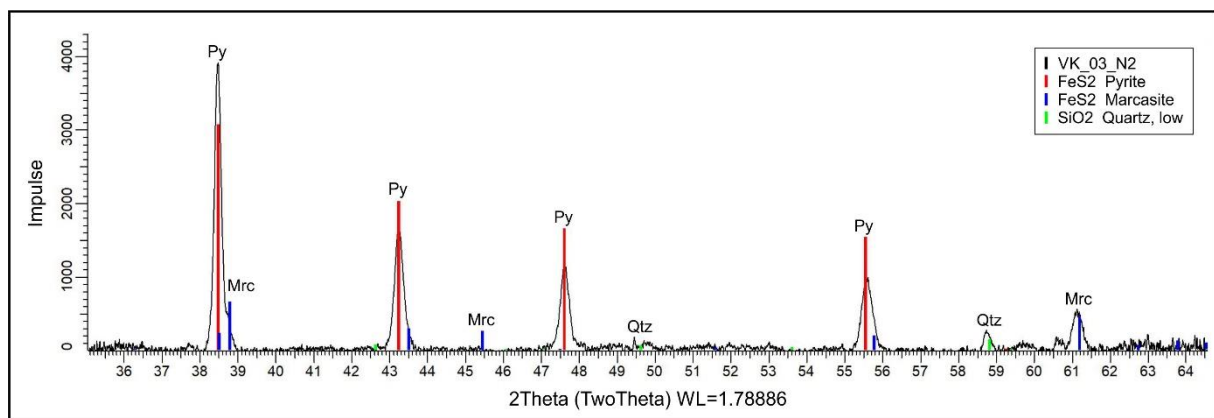

Fig. 25: *Diffractogram of the N$_2$-sample VK_03 from LC ('Black Rock').*
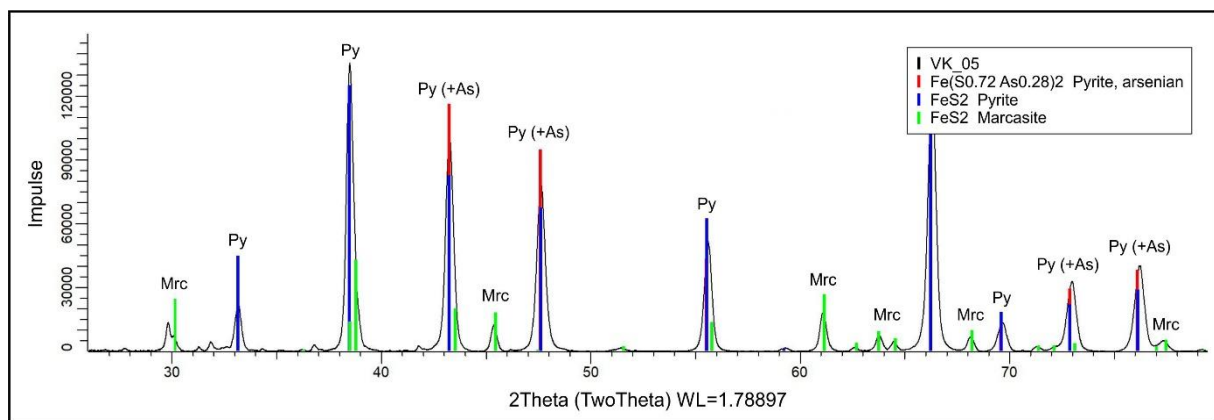
Fig. 26: *Diffractogram of VK_05 from LC – 'Mordor'; pyrite with arsenic traces.*

The EDX analysis supports the results of the light microscopy by confirming the presence of pyrite and/or marcasite. As a characteristic feature, very small pyrite crytals (framboidal occurrence) were detected within the marcasite precipitates of Area 26 (Fig. 29, B). Due to the large number of diagrams, images and tables, a selection of some analysis results is shown below. All further results and pictures as well as the profiles of all samples can be found in the appendix. In Fig. 27-29 with the corresponding tables Tab. 2-4 the EDX results and their interpretation are shown. Near by the chosen location of the microscopy section of BP2, the EDX measurement was carried out (Fig. 27). The results are registered in Tab. 2 below. The other samples were processed in the same way.
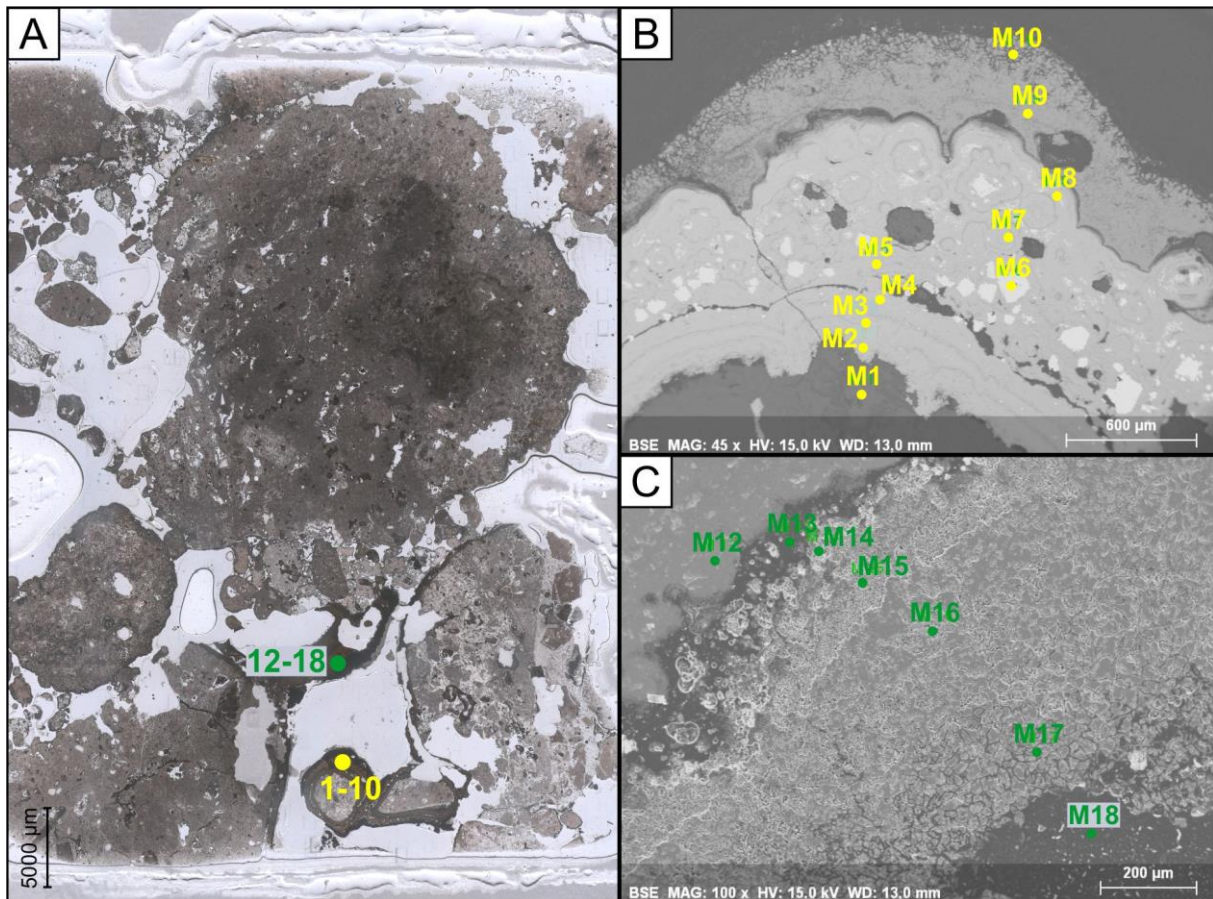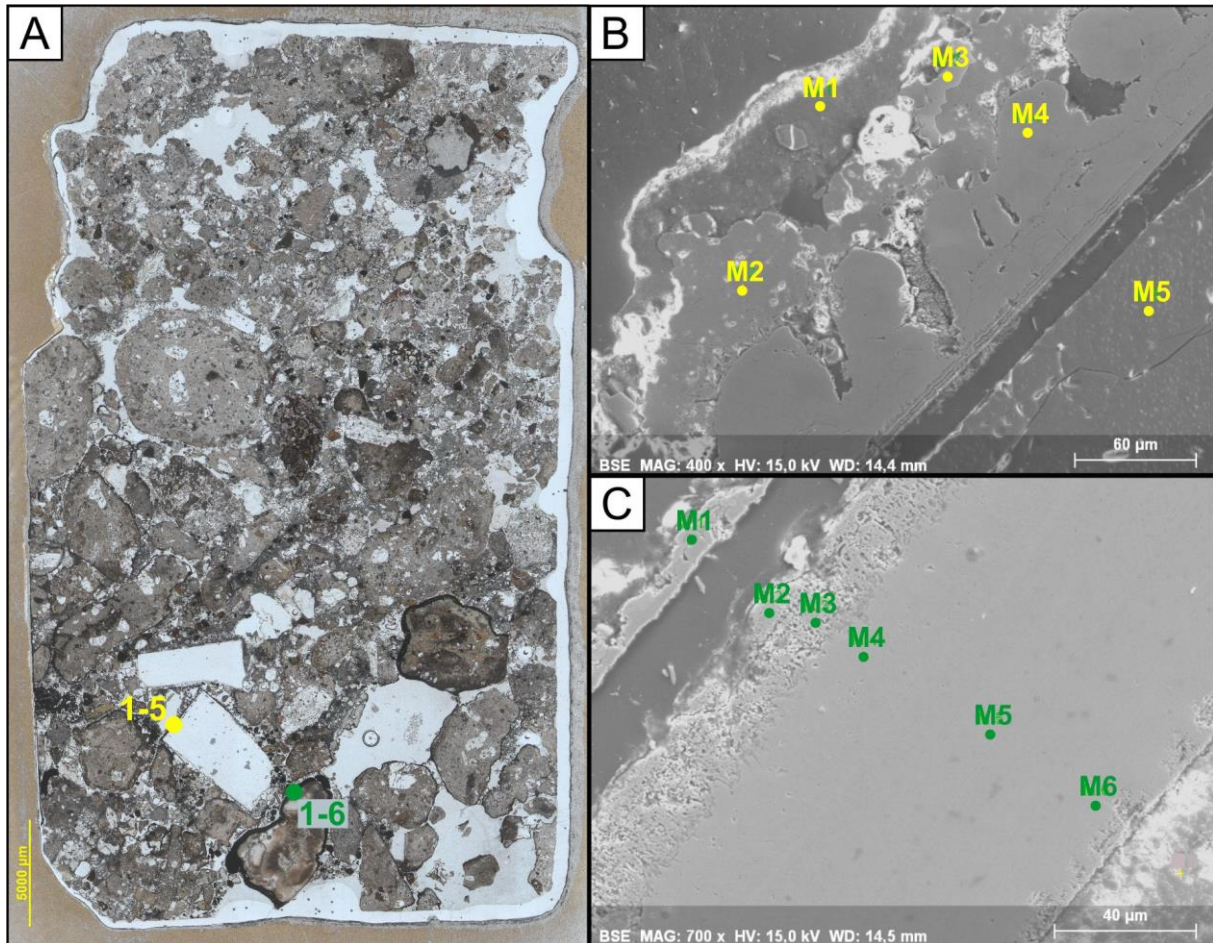
Fig. 27: *Thin section BP2 from BP; **A:** Survey of entire thin section (transmitted light, ll-pol); **B:** SEM image with EDX measuring points M1-10; **C:** SEM image with EDX measuring points M12-18. These points were chosen to show possible differences in chemistry and to test the microscopy results.*

Tab. 2: *Quantitative element analysis: EDX results of the associated measuring points (M) in Fig. 27, in red: FeS$_2$ minerals.*

[wt-%]	C	O	Si	S	Fe	Zn	As	Pb	Result
M 1		53.7	46.3						Quartz
M 2		2.0		28.5		68.6			Sphalerite
M 3		1.1		28.7		70.1			Sphalerite
M 4		1.7		30.2		68.1			Sphalerite
M 5	22.2	3.2	0.4	22.6		50.8			Sphalerite
M 6		0.8		13.1			0.3	85.7	Galena
M 7		1.0		29.9		69.1			Sphalerite
M 8		1.0		30.6		68.4			Sphalerite
M 9		7.6		43.8	48.2		0.4		**Py/Mrc**
M 10		3.8	1.2	47.1	46.7		0.4		**Py/Mrc**

| [wt-%]	C	O	Si	S	Cl	Fe	Zn	As	Result
M 12		1.5		29.2			69.3		Sphalerite
M 13	79.9	9.8		8.9	1.4				Crack/hole
M 14	73.2	6.9	0.3	14.4	2.0	0.6		2.5	Crack/hole
M 15		1.3	0.4	48.9		49.4			**Py/Mrc**
M 16		4.8	0.4	45.1		49.6		0.1	**Py/Mrc**
M 17		4.8		43.8		50.8		0.5	**Py/Mrc**
M 18	76.7	12.1	8.7	1.6	0.4	0.3			Crack/hole

Fig. 28: *Thin section VK_05 from LC – 'Mordor'; **A:** Survey of entire thin section (transmitted light, ll-pol); **B:** SEM image with EDX measuring points M1-5; **C:** SEM image with EDX measuring points M1-6 of a layered crust with a red outer part (cf. Fig. 23, images C and D). These points were chosen to test the microscopy results and give information about the chemical composition of the red outermost layer.*

Tab. 3: *Quantitative element analysis: EDX results of the associated measuring points (M) in Fig. 28, in red: FeS_2 minerals.*

[wt-%]	C	O	Na	Mg	Al	Si	S	Ca	Mn	Fe	Result
M 1		42.6	1.8	14.2	8.7	20.6	0.6	0.4	8.7	2.3	Clay
M 2	10.1	47.9		1.5			0.3	8.2	31.9		Rds
M 3		4.9	0.5				44.8		1.1	48.7	**Py/Mrc**
M 4		1.3					46.9		0.9	50.9	**Py/Mrc**
M 5		48.3	6.8	1.2	1.4	33.6		8.8			Feldspar

[wt-%]	O	Na	Mg	Al	Si	S	Mn	Fe	Result
M 1	18.4	0.5	0.5	0.5	0.4	27.2	0.4	52.2	n.e.i.
M 2	30.9		0.1	0.2	0.3	0.3	0.8	67.4	Hem/Gt
M 3	26.2		0.3	0.3	0.5	1.3	0.7	70.8	Hem/Gt
M 4	1.8					47.5		50.7	**Py/Mrc**
M 5	1.4					48.9		49.7	**Py/Mrc**
M 6	1.8					46.1		52.2	**Py/Mrc**
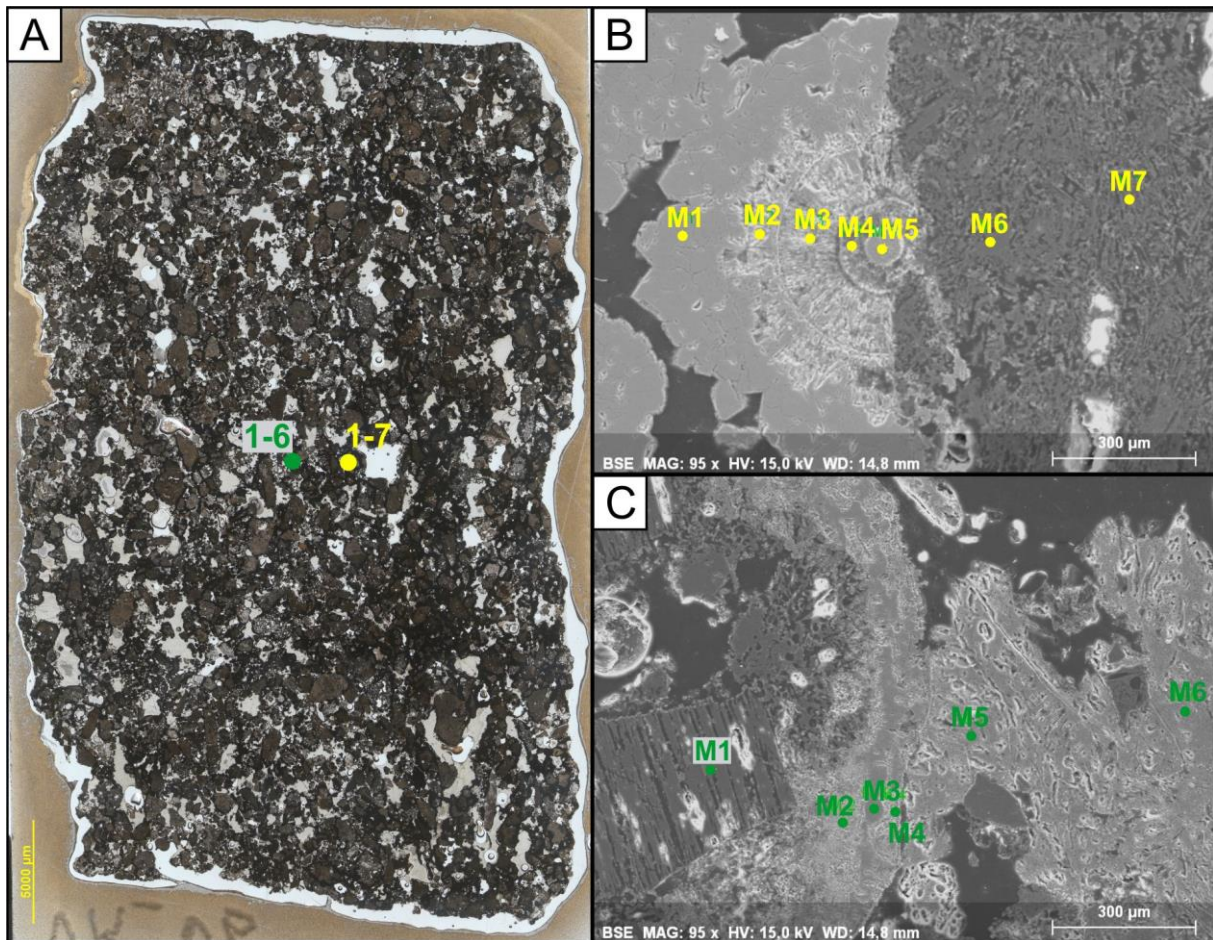
Fig. 29: *Thin section VK_06 from A26 - '3-bowls'; **A:** Survey of entire thin section (transmitted light, ll-pol); **B:** SEM image with EDX measuring points M1-7, points were chosen to show possible differences in chemistry of the flowered mineral precipitate, very small crystals in the center of the flower-shaped mineral aggregate; **C:** SEM image with EDX measuring points M1-6.*

Tab. 4: *Quantitative element analysis: EDX results of the associated measuring points (M) in Fig. 29, in red: FeS_2 minerals.*

[wt-%]	O	Na	Al	Si	S	Ca		Fe	Result
M 1	3.3				47.0			49.6	**Py/Mrc**
M 2	7.9			0.7	44.7	1.1		45.5	**Py/Mrc**, quartz
M 3	14.9	0.3	0.1	1.9	42.6	2.1		38.1	**Py/Mrc**, quartz
M 4	9.3	0.4		0.8	49.9			39.6	**Py/Mrc**, quartz
M 5	2.6			0.2	45.6			51.5	**Py/Mrc**
M 6	55.6		0.4	44.0					Quartz
M 7	48.9	0.1	0.8	49.4	0.5	0.3			Quartz

| [wt-%]	O	Na	Al	Si	S	Cl	Ti	Fe	Result
M 1	50.5	1.8	0.6	21.1	6.1	0.5	1.9	17.3	Biotite, **Py/Mrc**
M 2	9.3			0.2	54.2			36.3	**Py/Mrc**
M 3	4.3				44.6			51.1	**Py/Mrc**
M 4	13.5	0.4		0.1	48.8			37.2	**Py/Mrc**
M 5	2.3				97.7				Sulfur
M 6	1.0				99.0				Sulfur

4.1.2 Galena and sphalerite

Sulfide ore mineralization especially the precipitation of galena [Gn] and sphalerite [Sp] mainly occurs at Black Point.

Galena crystallizes in the cubical system. Hence, the crystal shape is mostly cubic. In the polished sections the color is gray-white. With crossed polarizers galena extinguishes. Sphalerite, like galena and pyrite, belongs to the cubic crystal system and therefore it is isotropic. The crystals commonly show curved, shell-shaped and botryoidal faces, which is pictured in Fig. 30. The color can vary strongly, ranging from nearly white to dark brown, gray, yellow and red, depending on the Fe-content.

In Fig. 30, galena occurs only in patches as cubical crystals surrounded by botryoidal shaped sphalerite. Similar to Fig. 24, marcasite forms the outer part of the sphalerite coating whereas pyrite is absent.
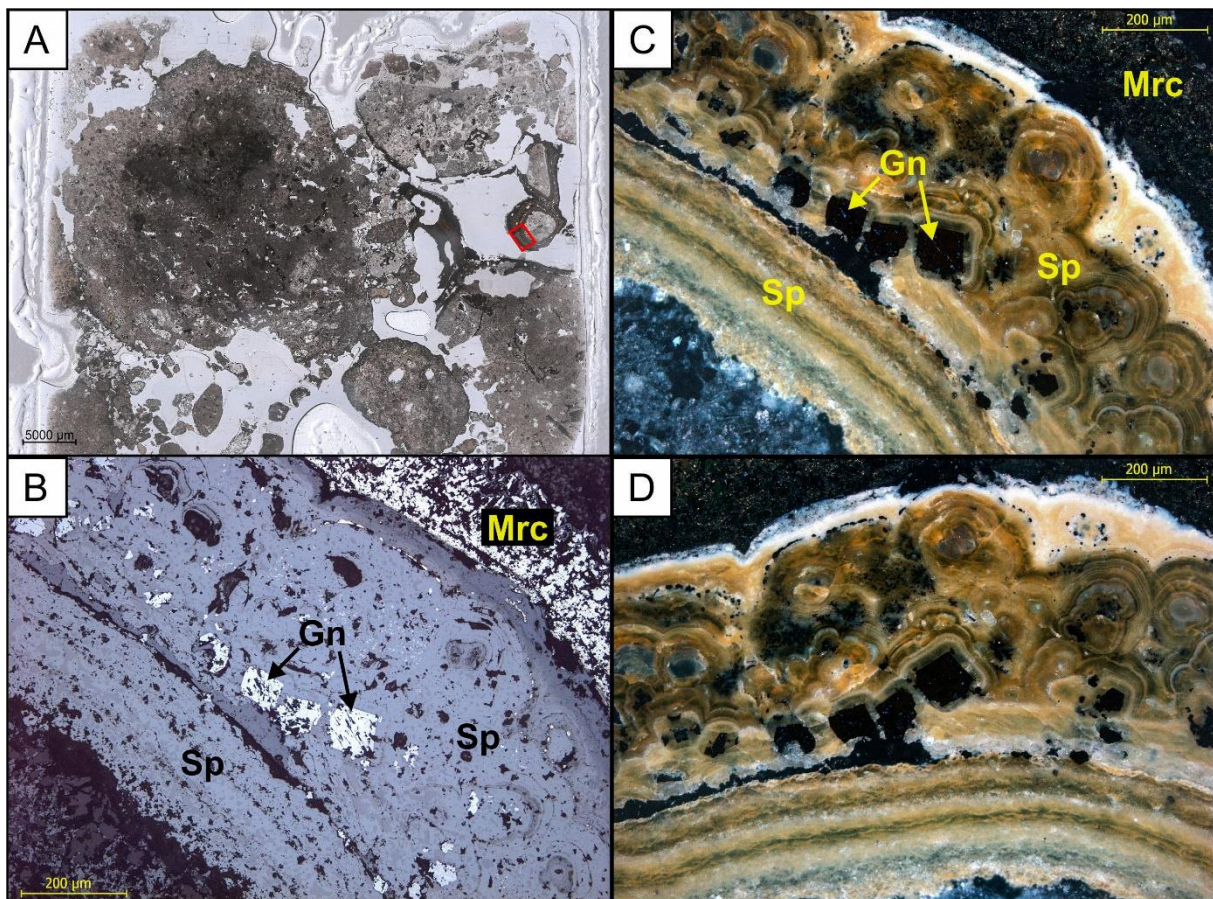
Fig. 30: *Thin section BP2 from BP; **A:** Survey of entire thin section (transmitted light, ll-pol), the red rectangle denotes the image detail; **B:** Well-formed galena crystals (gray-white) surrounded by sphalerite (gray) and marcasite at the outer part (reflected light, ll-pol); **C:** Same image detail as B, but with crossed polarizers; galena extinct, sphalerite occurs in curved, shell-like faces; **D:** Same image detail as C, but with 45° anticlockwise-turned stage; no color changes are seen due to the isotropy of both minerals.*

Every sample that contains sphalerite is associated with galena and vice versa. The occurrence of these two minerals is highly localized. They were only found at Black Point and in Area 26 at the location 'Mini Black Point'. In the thin section of this location (Fig. 31), galena reveals its typical whitish color. Different from Black Point, the Pb-sulfide did not crystallize in a well-formed cubic shape. It is found at the outer part of the precipitated minerals and as inclusions within the sphalerite.
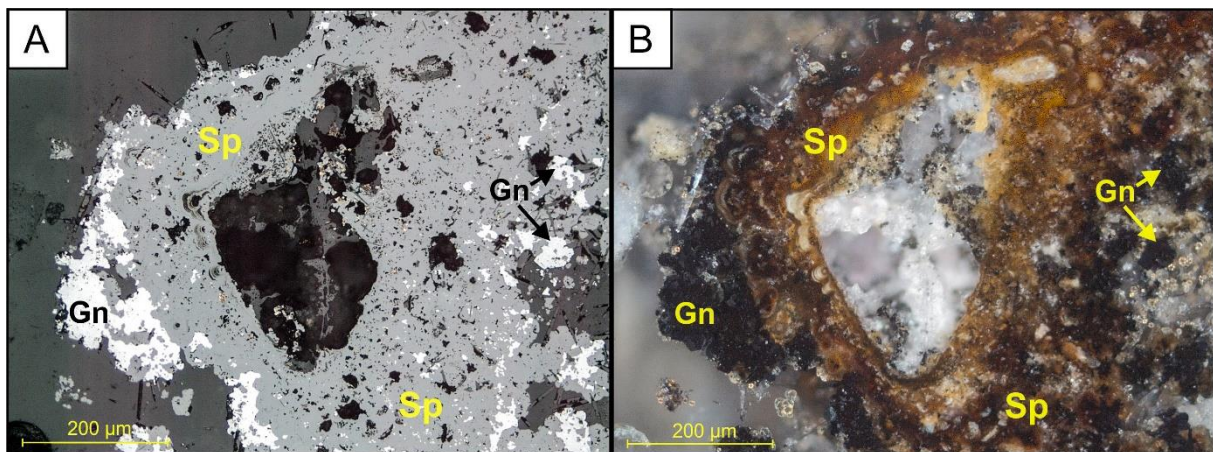

*Fig. 31: Detailed view of thin section VK_14 from 'Mini Black Point' in A26; **A:** Galena and sphalerite precipitates (reflected light, II-pol); **B:** Same image detail as A, but with crossed polarizers, galena and sphalerite with the appearance like at Black Point (cf. Fig. 30, images C and D).*

In both diving spots, Black Point and 'Mini Black Point' (A26), sphalerite appears as banded reniform and botryoidal aggregates with an obvious layered structure.

Chemical analyses support the microscopy results. In the following images and diagrams (Fig. 32 and 33) the results of the µXRD and SEM-EDX analysis are pictured.
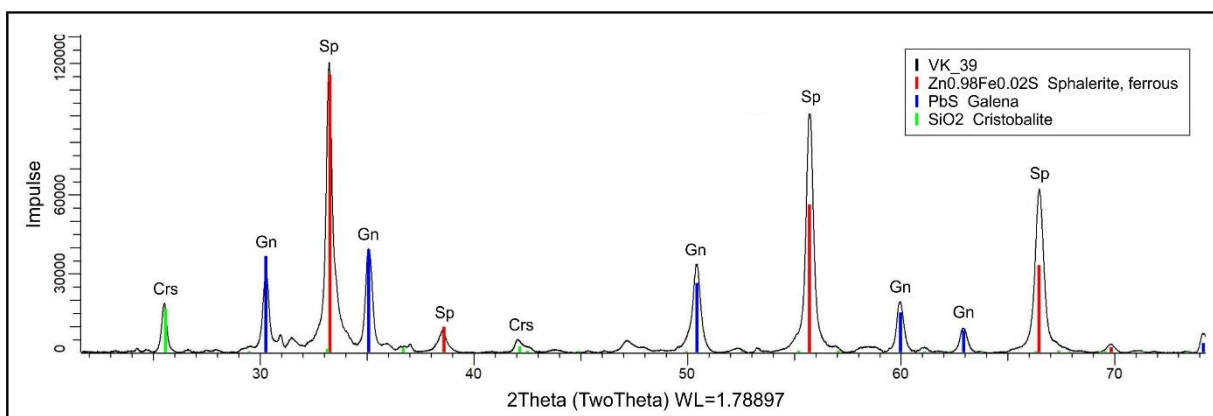
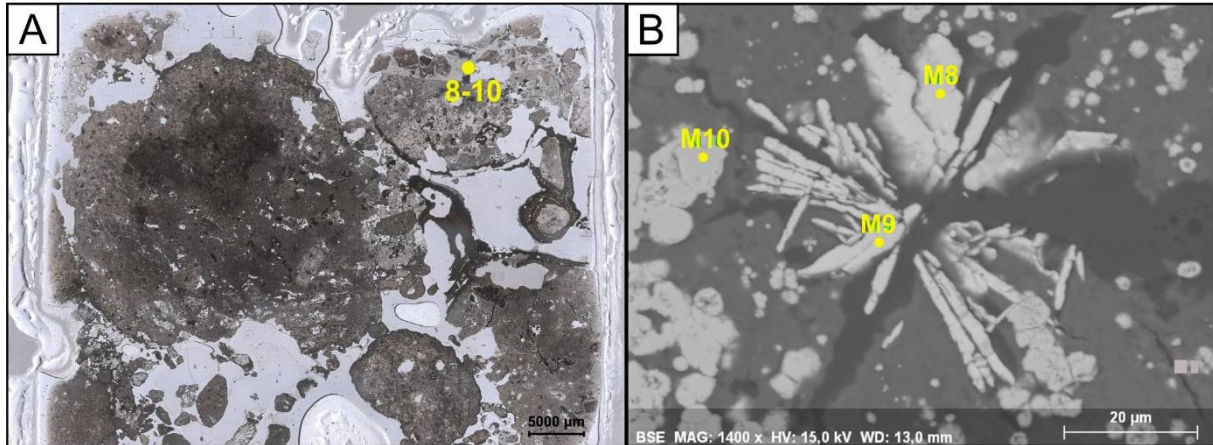*Fig. 32: Diffractogram of the sample VK_39 from BP.*
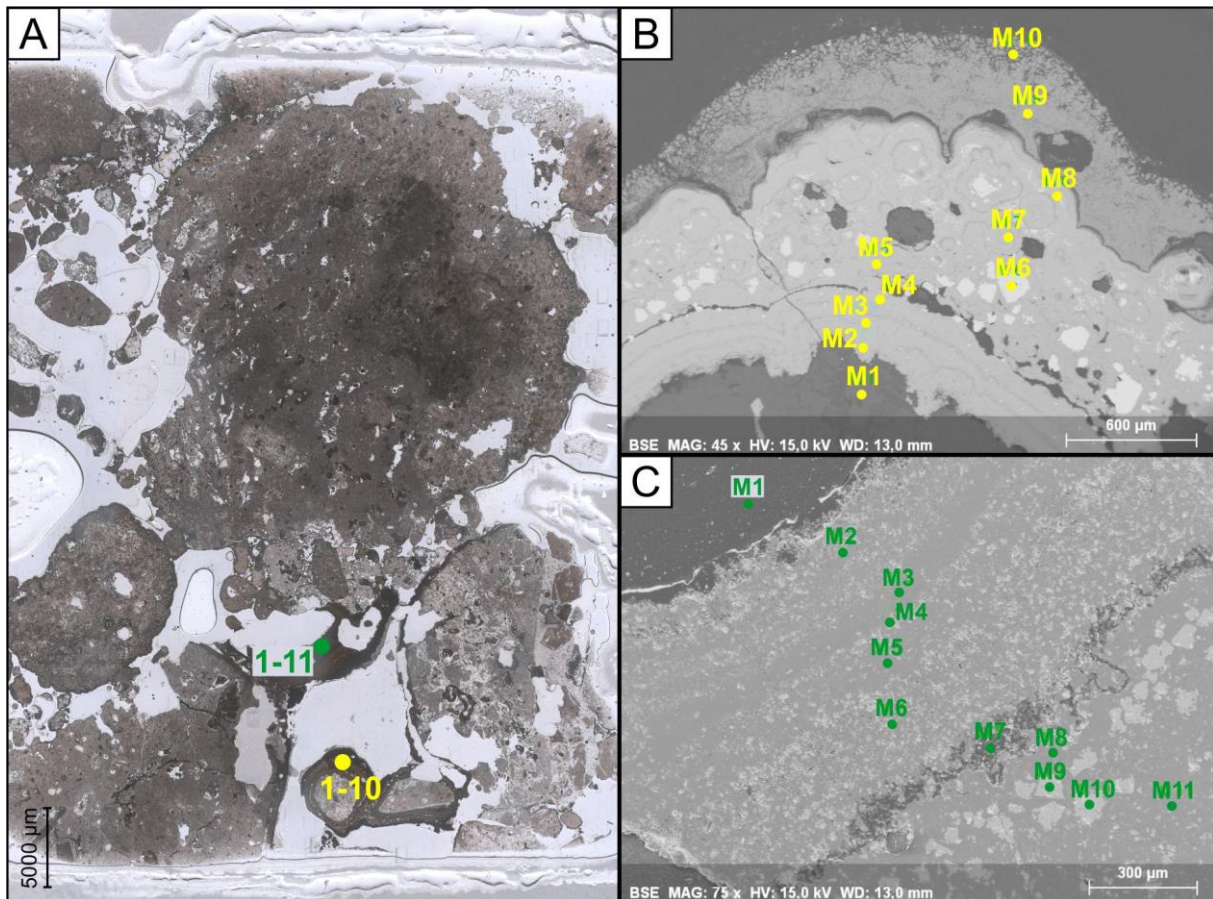
**Fig. 33:** *Thin section BP2 from BP; **A:** Survey of entire thin section (transmitted light, ll-pol); **B:** SEM image with EDX measuring points M1-10; **C:** SEM image with EDX measuring points M1-11. These points were chosen to show possible differences in chemistry because of the different brown hues and to test the microscopy results.*

Tab. 5: *Quantitative element analysis: EDX results of the associated measuring points (M) in Fig. 33, in red: Pb- and Zn-sulfides.*

[wt-%]	C	O	Si	S	Fe	As	Zn	Pb	Result
M 1		53.7	46.3						Quartz
M 2		2.0		28.5			68.6		**Sphalerite**
M 3		1.1		28.7			70.1		**Sphalerite**
M 4		1.7		30.2			68.1		**Sphalerite**
M 5	22.2	3.2	0.4	22.6			50.8		**Sphalerite**
M 6		0.8		13.1		0.3		85.7	**Galena**
M 7		1.0		29.9			69.1		**Sphalerite**
M 8		1.0		30.6			68.4		**Sphalerite**
M 9		7.6		43.8	48.2	0.4			Py/Mrc
M 10		3.8	1.2	47.1	46.7	0.4			Py/Mrc

[wt-%]	C	O	Al	Si	S	Cl	Zn	Pb	Result
M 1	73.8	15.6		7.4		3.3			Crack/hole
M 2		1.7	0.6	0.4	28.4		68.8		**Sphalerite**
M 3		1.5			28.0		70.5		**Sphalerite**
M 4		1.2			30.4	0.7	67.7		**Sphalerite**
M 5		2.3			26.6	1.0	70.1		**Sphalerite**
M 6		1.8		0.4	29.0	0.6	68.3		**Sphalerite**
M 7		8.3	20.6	19.5	18.7	2.6	28.7		n.e.i.
M 8		1.9			28.5	0.7	68.9		**Sphalerite**
M 9		0.6			12.8			86.7	**Galena**
M 10	9.9	3.9		0.8	10.6			74.4	**Galena**
M 11		0.9			29.6		69.5		**Sphalerite**

4.1.3 Barite

Barite was merely found at Black Point in form of lath-shaped minerals. The occurrence of the aggregate is rosette-like which is a common appearance of this sulfate (Fig. 34).

Fig. 34: *Thin section BP2 from BP; **A:** Survey of entire thin section (transmitted light, ll-pol); **B:** SEM image with EDX measuring points M8-10*

Tab. 6: *Quantitative element analysis: EDX results of the associated measuring points (M) in Fig. 34, in red: mineral of interest*

[wt-%]	O	S	Cl	Zn	Sr	Ba	Result
M 8	24.8	14.4			5.4	55.4	**Sr-Barite**
M 9	24.8	14.4			4.9	55.9	**Sr-Barite**
M 10	1.5	28.6	0.7	69.2			Sphalerite

4.2   Iron(hydr)-oxides

The occurrence of iron(hydr)-oxide precipitates is confined to only a few locations. Hematite [Hem]/goethite [Gt] occur(s) in Point 21 and in La Calcara in the area of 'Mordor' as a black to dark brown crust around the altered dacitic clasts (Fig. 35, Tab. 7; Fig. 36, Tab. 8). Iron tubes were found as tubes in Basiluzzo in previous diving excursions (see Stanulla, 2012), but are not further considered in this thesis, as no dives were realized last time.
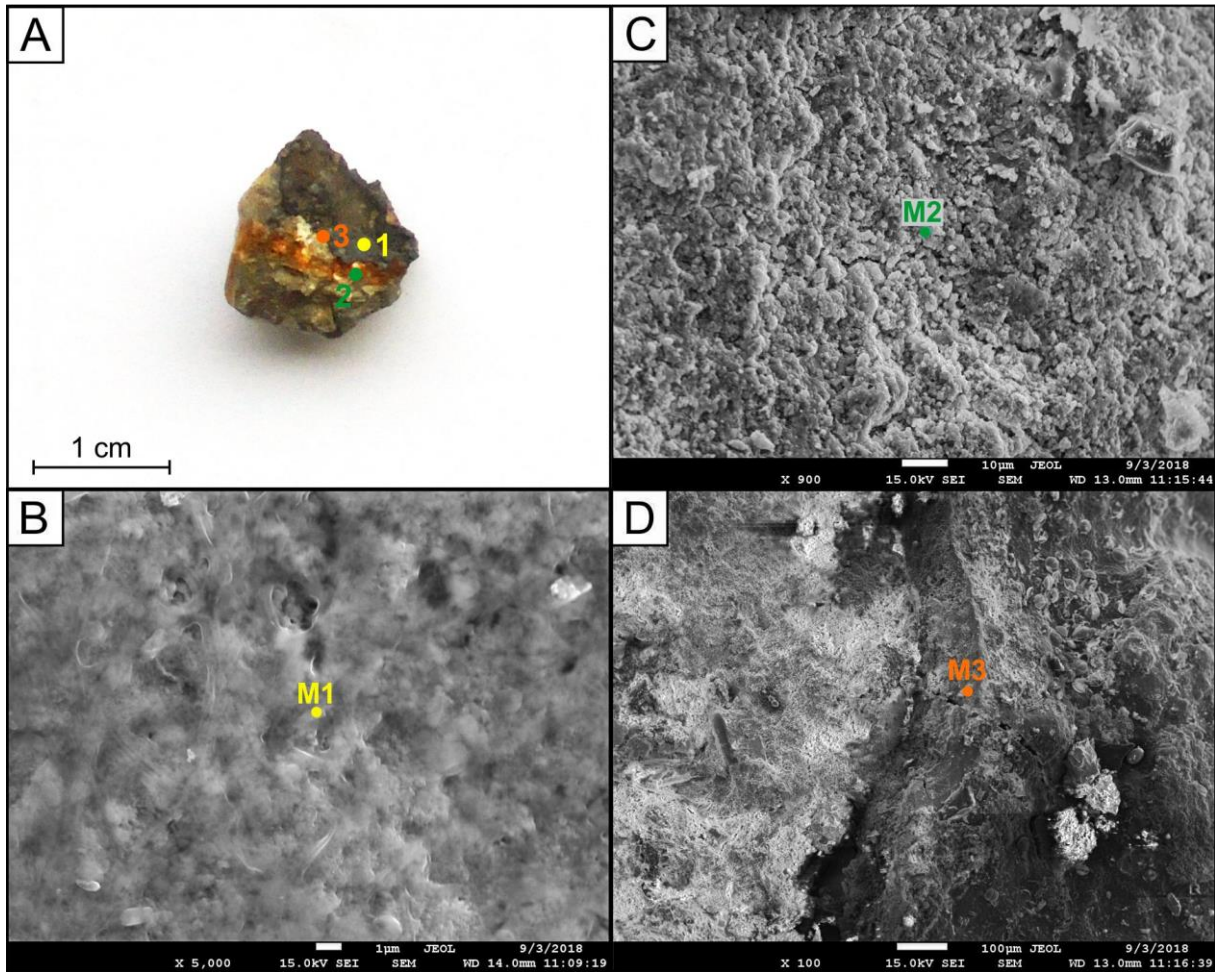
Fig. 35: *A: Small proportion of the sample VK_29 from P21; **B:** SEM image with EDX measuring point M1 of the brown crust; **C:** SEM image with EDX measuring point M2 of the orange-colored layer; **D:** SEM image with EDX measuring point M3 on the plane surface of the crusts edge. These points were chosen to get information about the chemical composition of the crust and the orange-colored layer.*

Tab. 7: *Quantitative element analysis: EDX results of the associated measuring points (M) in Fig. 35, in red: iron(hydr)-oxides.*

[wt-%]	O	Na	Mg	Al	Si	S	Cl	V	Fe	Zn	Result
M 1	28.5	0.3	0.9	1.8	0.1	3.1	2.2	0.8	59.7	2.6	**Hem/Gt**
M 2	38.7	2.0	1.1	0.4	9.1	1.6	6.3		36.3	4.5	**Hem/Gt**
M 3	41.8	0.8	1.3	1.4	0.3	1.5	1.8	0.5	48.1	2.4	**Hem/Gt**
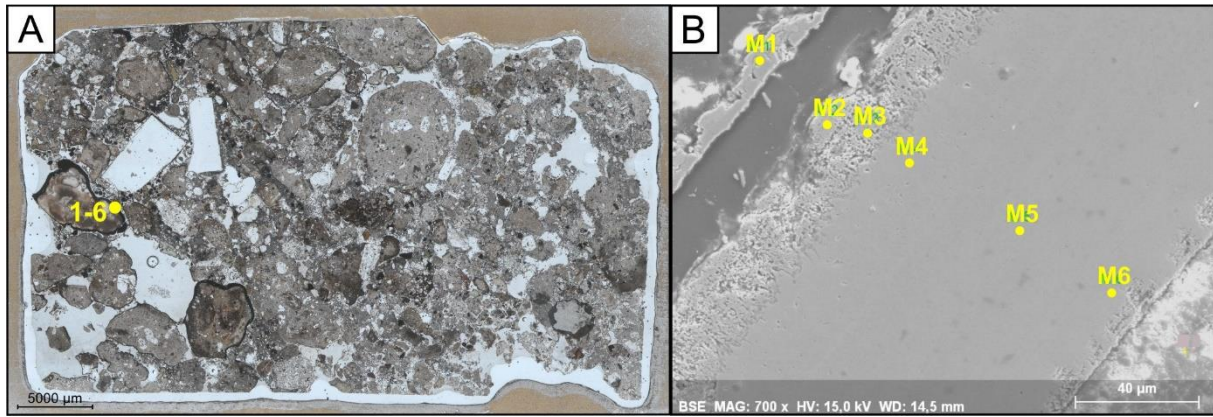
Fig. 36: *Thin section VK_05 from LC – 'Mordor'; **A:** Survey of entire thin section (transmitted light, ll-pol); **B:** SEM image with EDX measuring points M1-6 (cf. Fig. 28, image C). They were selected to give information about the chemical composition of the red outermost layer.*

Tab. 8: *Quantitative element analysis: EDX results of the associated measuring points (M) in Fig. 36, in red: iron(hydr)-oxides.*

[wt-%]	O	Na	Mg	Al	Si	S	Mn	Fe	Result
M 1	18.4	0.5	0.5	0.5	0.4	27.2	0.4	52.2	n.e.i.
M 2	30.9		0.1	0.2	0.3	0.3	0.8	67.4	**Hematite/goethite**
M 3	26.2		0.3	0.3	0.5	1.3	0.7	70.8	**Hematite/goethite**
M 4	1.8					47.5		50.7	Pyrite/marcasite
M 5	1.4					48.9		49.7	Pyrite/marcasite
M 6	1.8					46.1		52.2	Pyrite/marcasite

Hematite and goethite are hard to distinguish with the SEM-EDX analysis due to the similar chemical composition. Hydrogen, the distinguishing element, cannot be detected by EDX. Furthermore, both minerals show reddish to brownish colors under reflected light. However, a distinctive feature is the streak color of these minerals. Hematite has a blood red to reddish-brown streak whereas goethite shows yellowish, orange to brownish colors. Obviously, the streak color cannot be identified because of the minerals size. In La Calcara it is merely visible in thin sections as a small proportion of the mineral crust. But in Point 21 the iron(hydr)-oxide forms the outermost part of the clasts so that the color of the streak could be ascertained. As shown in Fig. 37 the streak is orange-brown (tested with both small samples of VK_29). This color indicates that the iron(hydr)-oxide is goethite because shades of red are absent.

It can be assumed that the iron(hydr)-oxide of the sample VK_05 from La Calcara is hematite. Usually, hematite has a higher Fe concentration than goethite but as a result of the size and the penetration depth of the EDX measuring field the element concentration has to be handled with care.
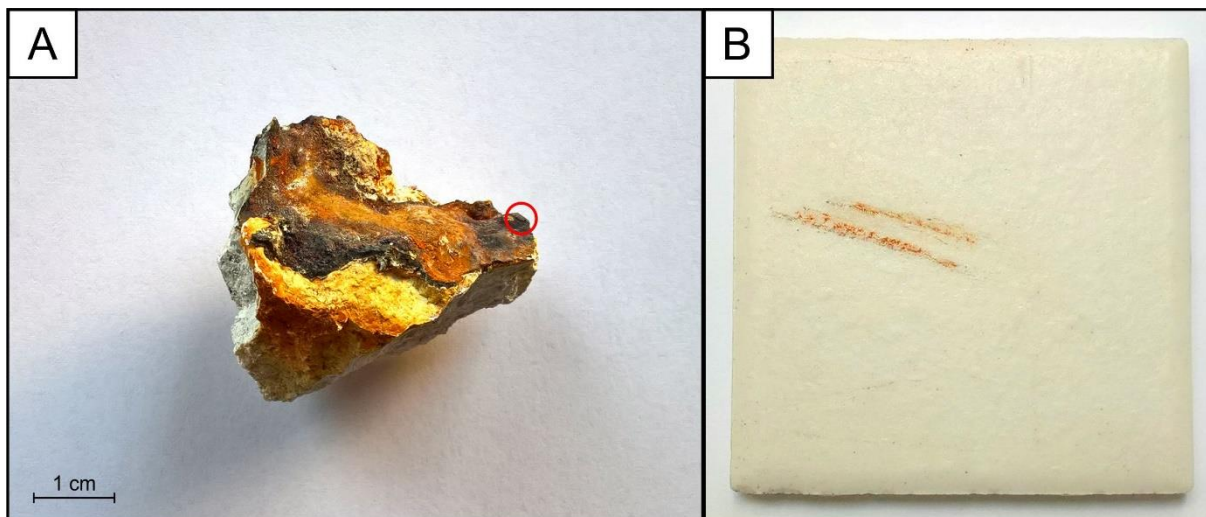
Fig. 37: Sample VK_29 from P21; *A:* Iron(hydr)-oxide crust (thickness of ~1 mm) around the clast; *B:* Ceramic tablet with the orange-brown streaks of the sample.

4.3 Sulfur

Sulfur occurs almost everywhere and with different forms of appearances: around gas and water emanations as fine-grained precipitates, as crystalline sulfur, as cement of conglomerates, and as crusts around boulders. Sulfur cemented cones and tubes are a common discharge feature of 'Brodor', the newly excavated spot in Area 26 (Fig. 38). In Bottaro North, Cave and Fumarolic Field, sulfur acts as cement of the conglomerates (Fig. 39).
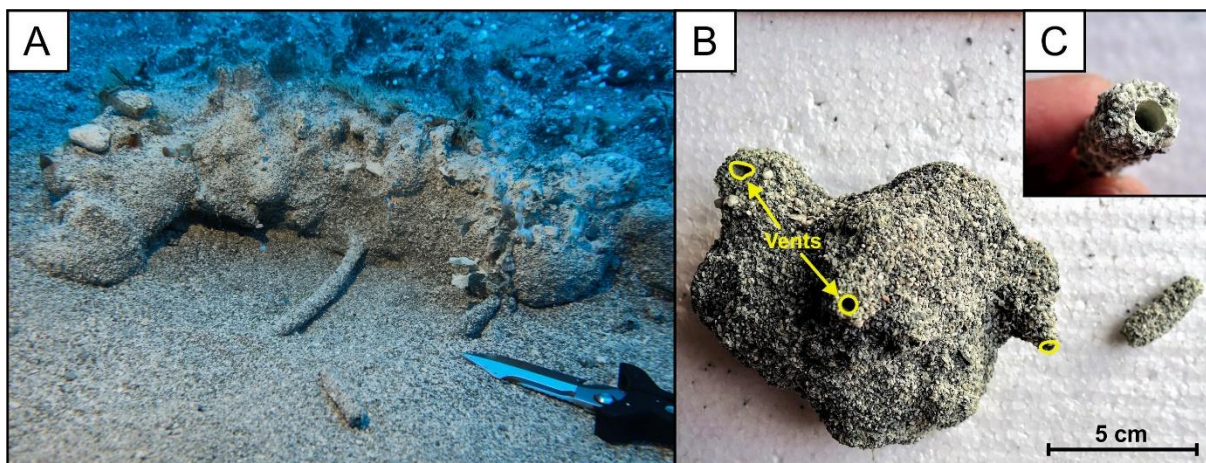
Fig. 38: Discharge features of 'Brodor' - A26, knife as scale (blade with a length of 15 cm); *A:* Section of the east part of 'Brodor' with cones and tubes (photo by R. Stanulla); *B:* Sulfur cemented cone and tube; *C:* Detail image of the cross-section of the tube.
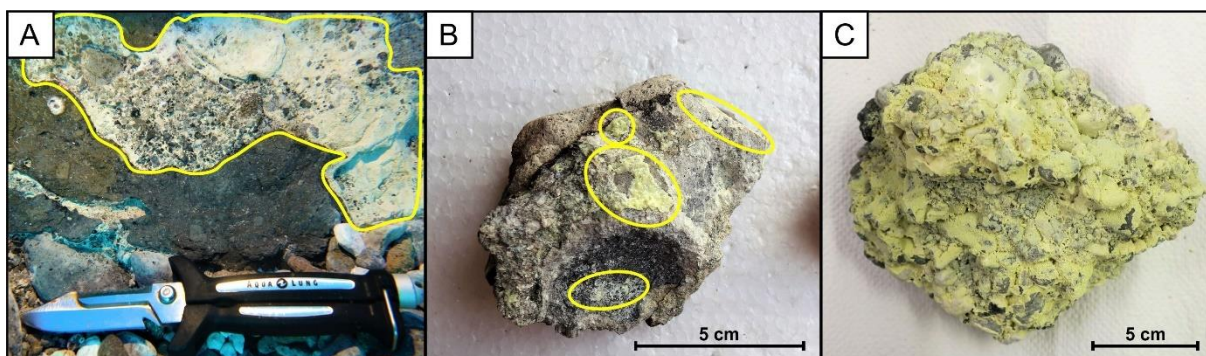
Fig. 39: *'Sulfur conglomerates' from different locations;* ***A:*** *Sulfur cemented coarse-grained sediment of BN (photo by R. Stanulla), knife as scale (35 cm);* ***B:*** *Fine-crystalline sulfur as cement in CA;* ***C:*** *Conglomerate with sulfur cement from FF.*

Elemental sulfur also occurs at Black Point. There, it acts as cement of the coarse-sandy to fine-gravelly sediment (already mentioned in Hildebrand, 2013). The results of the EDX measurements are given in Tab. 9.
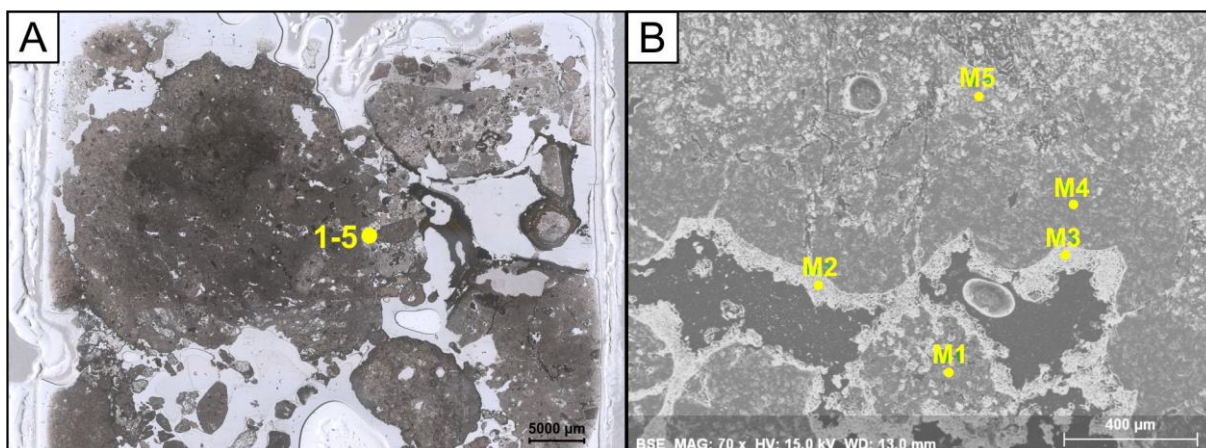
Fig. 40: *Thin section BP2 from BP, focus was set on sulfur precipitation;* ***A:*** *Survey of entire thin section (transmitted light, ll-pol);* ***B:*** *SEM image with EDX measuring points M1-5.*

Tab. 9: *Quantitative element analysis: EDX results of the associated measuring points (M) in Fig. 40, in red: elemental sulfur.*

[wt-%]	O	Na	Al	Si	P	S	K	Fe	Result
M 1	54.9	2.1	17.5	0.1	0.1	15.6	3.5	6.2	n.e.i.
M 2	2.9			0.4		96.7			**Sulfur**
M 3	5.9			0.3		93.8			**Sulfur**
M 4	55.3	0.2	0.5	44.0					Quartz
M 5	52.2	0.2	0.5	47.2					Quartz

Sulfur crusts composed of multiple sulfur layers (each ~ 1 mm thick) are found at Point 21 where strong gas venting occurs. With a total thickness of ~ 1.5 cm, the crust forms a coating with a homogeneous surface around the boulders (Fig. 41).

Fig. 41: *Sulfur crust (layered) around dacite at P21 (photo by R. Stanulla), knife as scale (35 cm in length).*

4.4 Manganese

Manganese was detected at the location Fumarolic Field. Furthermore, it was found with very low concentrations within Fe-bearing minerals in La Calcara at 'Mordor' and, according to Kakuk (2016), at the same location as rhodochrosite (see Tab. 3 and 8). In Fumarolic Field it occurs as dark brown coating around the gravel (Fig. 42).
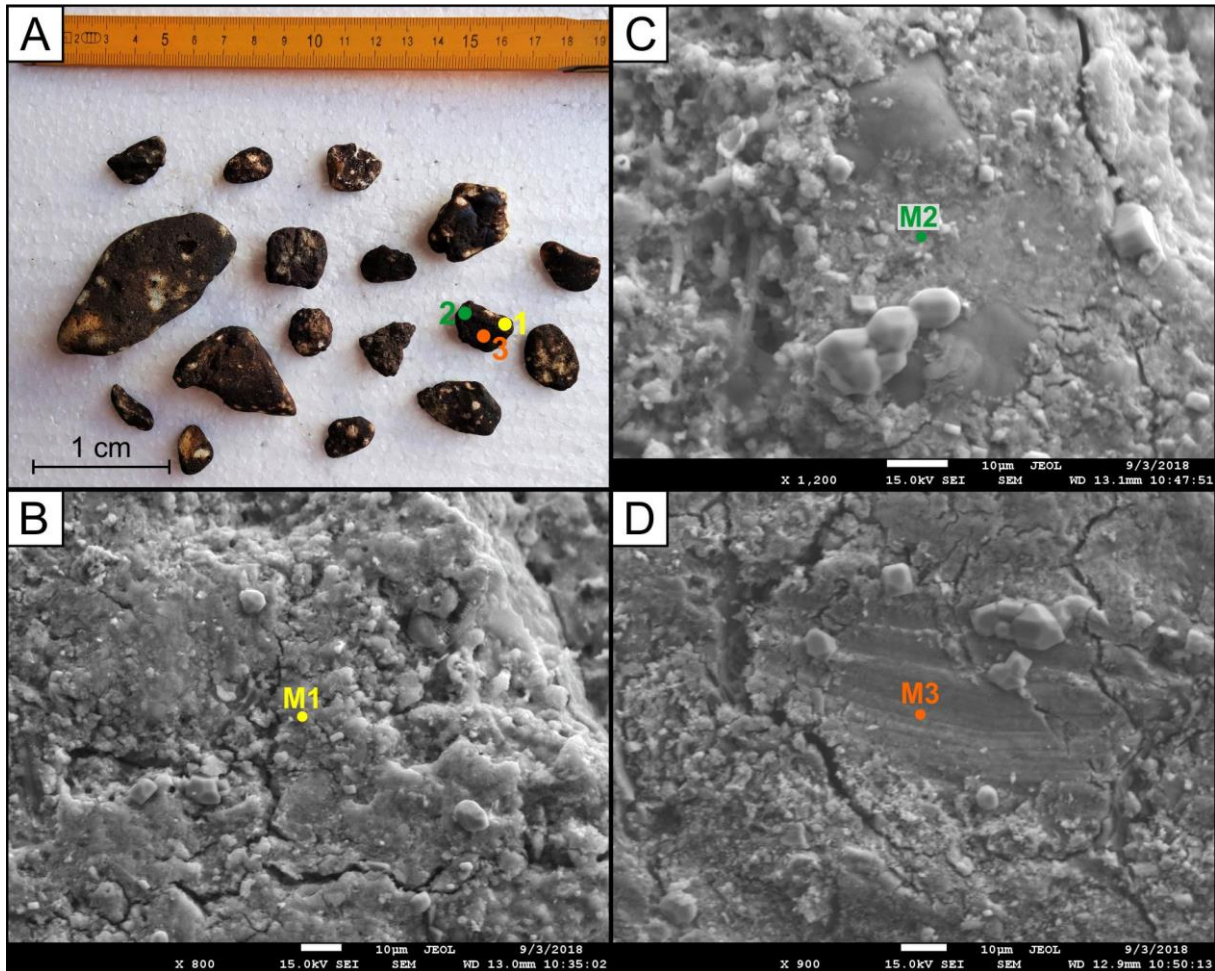
Fig. 42: *A: Pebbles of the sample VK_07 from FF; **B:** SEM image with EDX measuring point M1 of the dark brown coating; **C:** SEM image with EDX measuring point M2, well-shaped halite [Hl] crystals (as result of evaporation of sea water) are visible; **D:** SEM image with EDX measuring point M3 on the plane surface of the coating. These points were chosen to get information about the chemical composition.*

Tab. 10: *Quantitative element analysis: EDX results of the associated measuring points (M) in Fig. 42, in red: Mn-oxide.*

[wt-%]	O	Na	Mg	Al	Si	S	Cl	K	Ca	Mn	Fe	Result
M 1	41.2	8.6	3.2	0.4	0.6	0.8	11.2	0.6	0.7	27.7	4.7	**Mn-oxide** (+Hl)
M 2	35.9	13.3	3.0	0.4	2.2	1.1	13.0	1.0	1.0	26.8	2.1	**Mn-oxide** (+Hl)
M 3	39.9	3.9	3.5	0.4	0.4	1.0	5.0	1.4	0.8	39.1	1.9	**Mn-oxide**

5 Interpretation and discussion

The results show that the precipitation of various minerals took and still takes place in the investigation area of Panarea and its surrounding islets. Some of the mineral associations occur in other submarine hydrothermal systems which are found all over the world. Hence, a comparison of the genesis between these systems is likely and will be considered and explained in this chapter. Furthermore, possible mineral precipitations from fluids were calculated and modeled with PHREEQC (by B. Merkel) and EQ3/6. The results are attached in Tab. 13, 16 and 17. Please note: a positive SI (oversaturation) indicates only the possibility of precipitation of a certain mineral. Sudden changes in temperature, pH and redox potential as a consequence of mixing with sea water have to be considered as well.

5.1 Sulfuric species

The processes of the precipitation of sulfide minerals in the investigation area near Panarea are genetically comparable to processes in Volcanogenic Massive Sulfide (VMS) deposits. The sulfide minerals around Panarea are deposited in the form of crusts (mm to cm in thickness) and as disseminated grains or cement in the sediment.

Volcanogenic massive sulfides of VMS deposits occur at mid-ocean ridges, along island arcs and in (continental) back-arc basins of subduction zones, as in Panarea. Sea water penetrates the seafloor along faults and fractures. The cold water is heated by the releasing heat of magma and is mixed with hot acidic fluids. Transition metals (e.g. Cu, Fe, Mn, Pb, Zn, etc.) and sulfur compounds were mobilized out of the surrounding rock, commonly mafic to intermediate volcanic rocks, because of the aggressive character of the ascending waters and gases (James et al., 2014). The sudden cooling of these hydrothermal fluids due to mixing with cold sea water (in the deep sea ~ 2 °C) causes the re-precipitation as metal sulfides directly beneath or at the seafloor (Robb, 2005). Black smokers are a special case where immediate chemical reactions between the discharging hydrothermal fluids and the surrounding sea water in form of chimney-shaped precipitates can be observed. Temperatures of up to 400 °C can occur and pH-values of 4-6 are characteristic (Lowell et al., 1995; Gamo et al., 1996; Robb, 2005). Anhydrite is the main mineral that builds up the chimney at the very beginning of the mineral precipitation. Typical massive sulfide ore minerals in such environments are chalcopyrite, pyrrhotine, pyrite/marcasite, sphalerite and galena.

The precipitation of sulfide minerals at Black Point is comparable with the formation processes of black smokers. As a result of the analogy to black smokers, the fluids of Black

Point are named 'smoker type fluids', but differences in chemical composition and fluid properties are obvious. Maximum temperatures of 134.1 °C and a minimum pH of 2.4 were measured at this gray smoker (Appendix: Tab. 12). Such a temperature is too low for the precipitation of Cu-minerals or anhydrite (see Robb, 2005). For this reason, only galena, sphalerite, marcasite (due to the low pH), and a small amount of barite occur as minerals of the low-temperature zone.
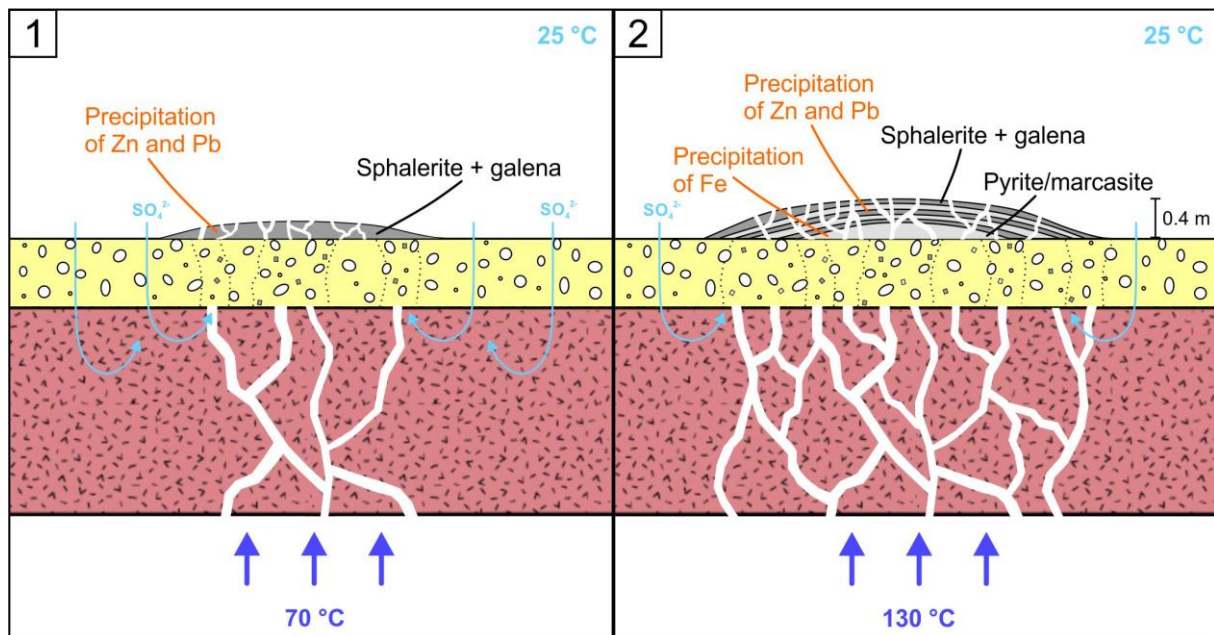

Fig. 43: Sketch of the development of sulfide minerals at BP as described in the text; sediment thickness and underlying rock are not in scale.

The precipitation of sulfides starts with the ascent of metal-enriched, hot black smoker type fluids along faults and fissures. The surrounding host rock is gradually altered so that ore minerals can precipitate within newly formed fissures and as disseminated grains in the sediment. At relatively low temperatures, sphalerite, galena, and barite precipitate at first (Fig. 43, 1). At the beginning of the mineral precipitation, sea water can penetrate deeper into the sediment and cools the ascending black smoker type fluids. With ongoing precipitation of the sulfide minerals, the penetration area of sea water decreases in size. Therefore, the fluids can reach higher temperatures near the seafloor because they were not cooled down as much as before. The formation of a small hill-shaped gray smoker takes place with continuous precipitation. Marcasite occurs near the surface only when the temperatures of the discharging fluids reach 77 °C or more (Fig. 43, 2). Also, SiO_2 can occur within a wide temperature range as a residual of the hydrothermal altered silica minerals (Okrusch and Matthes, 2014). For the formation of barite, dissolved SO_4^{2-} ions are contained in the sea water or were supplied by the fluids itself. The sulfide minerals occur mainly as sediment-

hosted, disseminated ore aggregates, but also in form of porous crusts as it is the case at Black Point (Pohl et al., 2009).

Possible mineral precipitations at various temperatures and mixing ratios were calculated with EQ3/6. The results are attached in Tab. 16 and 17. At the beginning, high ratios of sea water mixing into the fluid cause a significant decrease in temperature. In all calculations, galena favors to precipitate at low temperatures (up to ~ 45 °C) while sphalerite occurs over a wide temperature range. With decreasing mixing ratios temperatures increase and trigger the precipitation of FeS_2.
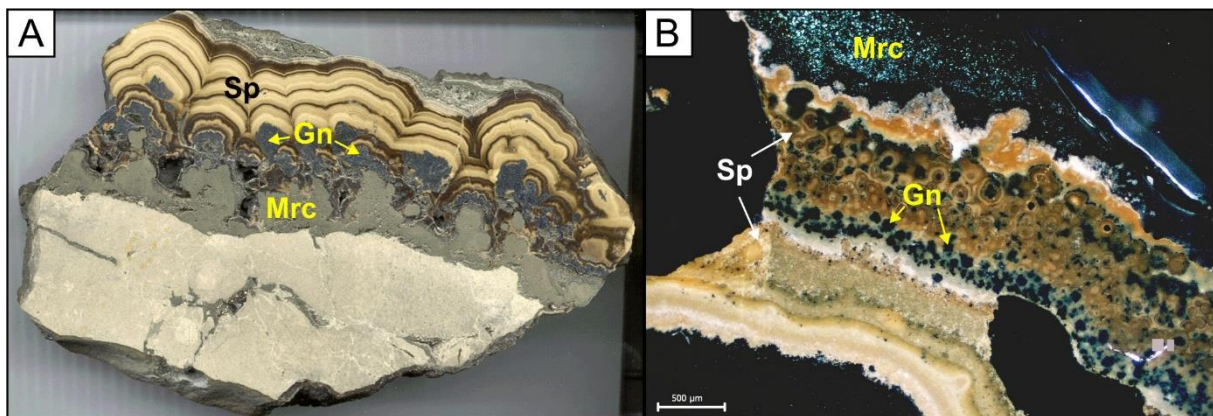
Fig. 44: *Similar appearance of sulfide ore mineral precipitates from BP and massive sulfides of black smokers; A: Fossilized black smoker (Dutrow, access date 19/11/2018), mineral layer can reach a thickness of up dm; B: Same minerals occur as crust at BP, but with only a few mm in thickness.*

Black smoker fluids usually do not contain magnesium whereas sea water has an average magnesium concentration of 1300 mg/l (Lowell et al., 1995). The higher Mg-concentrations of the measured fluids (Tab. 12 in the appendix) originate from the increased mixing of the hydrothermal water with ambient sea water. Elevated Na- and Cl-values in these fluids indicate that phase separation took place in greater depth. Ascending water starts to boil if the ascent is fast and the pressure relatively low. Thereby, H_2O gets lost in the form of steam and brine remains which causes the high salt concentration in the emanated water (personal communication with B. Merkel, SDC Freiberg).

In the literature, elemental sulfur is not named as typical mineral in black smoker environments. At Black Point, however, it is found dispersed in the sediment or as cement of the coarse-grained fraction and affects the porosity of the sediment. Hence, it is highly probable that the black smoker type fluids of Black Point are rather acid sulfate fluids. This kind of fluids occur in back-arc hydrothermal environments and are further explained by Seewald et al. (2015). Acid sulfate fluids are distinguished from black smoker fluids by physico-chemical parameters. Relative to black smokers, they show higher Mg^{2+} and SO_4^{2-} concentrations in the liquid phase and are more acidic. Additionally, the temperature is much

lower compared to black smoker fluids (Seewald et al., 2015). Typical magma-related volatiles are CO_2, HCl, H_2S, and SO_2 whereas SO_2 preferentially stays in the aqueous fluids as solution. With decreasing temperatures, magmatic SO_2 reacts with water to produce reduced sulfuric compounds and elemental sulfur (James et al., 2014; Seewald et al., 2015):

$$4\ SO_{2\ (aq)} + 4\ H_2O \quad = \quad 3\ H_2S_{\ (aq)} + H_2SO_{4\ (aq)} \qquad (1)$$

$$3\ SO_{2\ (aq)} + 2\ H_2O \quad = \quad S^0 + 2\ H_2SO_{4\ (aq)} \qquad (2)$$
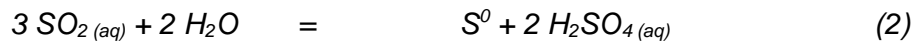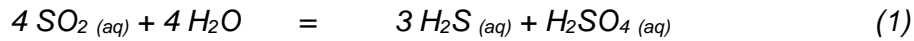
Sulfuric acid as a product of the reaction equations (1) and (2) dissociates into hydrogen and sulfate:

$$H_2SO_4 \quad = \quad 2\ H^+ + SO_4^{2-} \qquad (3)$$

Consequently, these reactions are strongly dependent on temperature, redox potential, and the amount of dissolved SO_2 in the fluid. The more the reaction is pushed in the direction of the products the more acidic the fluid becomes. This increasing acidity leads to the increasing solubility of sulfide mineral forming metals of the surrounding rock as a result of hydrothermal alteration (Seewald et al., 2015). When these fluids are emitted at the seafloor at Black Point, sphalerite, marcasite, galena, barite, and elemental sulfur precipitate.

Ore mineral precipitations are strongly connected to tectonic features like faults and minor fractures. At some sites, e.g. Point 21, sulfide minerals occur as small-scale mineralization in only a few fractures (Becke, 2009).

In all locations where FeS_2 precipitates, it occurs as pyrite and marcasite. At Black Point, however, marcasite is merely present. The essential criteria of the formation of either pyrite or marcasite are temperature and pH. Stability relations between these two minerals are still not totally understood. Marcasite is noted for low formation temperatures. It represents the metastable phase of pyrite above 150 °C and is transformed into pyrite at temperatures higher than 400 °C (Okrusch and Matthes, 2014). As already mentioned, the pH-value plays an important role for the formation of marcasite and pyrite. Marcasite preferentially precipitates out of acidic solutions (pH < 4) while under neutral and alkaline conditions (pH > 6) only pyrite is formed (Schoonen and Barnes, 1991; Schoonen, 2004).

Black Point is characterized by the highest temperatures and lowest pH-values of the entire investigation area. With fluid temperatures of up to 134 °C and an extreme pH of 2.4, this site provides the required conditions for the formation of marcasite.

Acidic and sulfidic fluids are not solely responsible for the sulfide species occurring nearly in the entire investigation area. Bacteria are an important part of the sulfur cycle in respect to the formation of elemental sulfur or FeS_2 (pyrite). Bio mats composed of diverse bacteria are

found wherever hydrothermal gas and water discharge from the seafloor. With increasing distance to the vents bacterial activity significantly decreases. In the area around Panarea the bacteria domain *Acidithiobacillus ferrooxidans* as sulfur oxidizer is responsible for the formation of elemental sulfur due to the oxidation of H_2S (Fig. 45). In contrast, the bacteria species *Desulfuvibrio* drives the reduction of sulfates and catalyzes the transformation of FeS to FeS_2 (Robb, 2005; Manini et al., 2008).
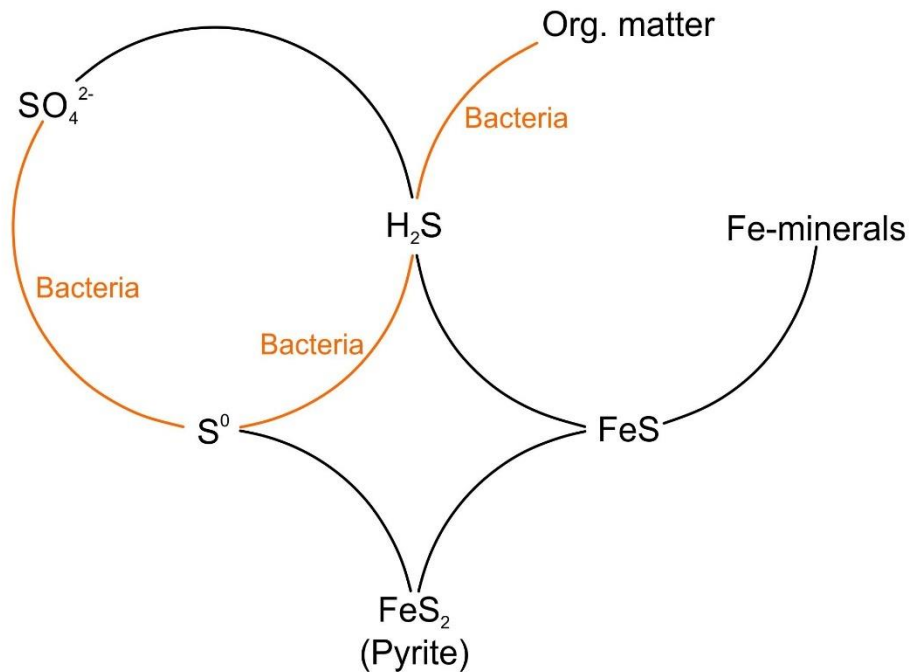
Fig. 45: *Sulfur cycle: pyrite formation in sediments (modified after Berner, 1985).*

According to van der Veen (2003) the bacterial formation of pyrite is subdivided into several steps. However, organic matter is not required for the formation of H_2S because it is provided by the fluids:

$$18\ CH_2O + 9\ SO_4^{2-} \quad = \quad 9\ H_2S + 18\ HCO_3^- \qquad (4.1)$$

$$6\ FeOOH + 9\ H_2S \quad = \quad 6\ FeS + 3\ S^0 + 12\ H_2O \qquad (4.2)$$

$$3\ FeS + S^0 \quad = \quad Fe_3S_4 \qquad (4.3)$$

$$Fe_3S_4 + 2\ S^0 \quad = \quad 3\ FeS_2 \qquad (4.4)$$

$$18\ CH_2O + 9\ SO_4^{2-} + 6\ FeOOH \quad = \quad 18\ HCO_3^- + FeS + 3\ FeS_2 + 12\ H_2O \qquad (4.5)$$
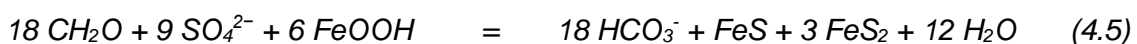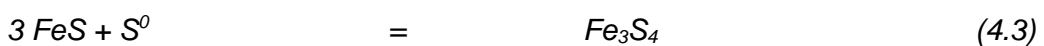
FeS is an intermediate product of the pyrite genesis. It is unstable under a sulfidic condition, due to a surplus of H_2S, which leads to the direct formation of pyrite without the intermediate step of Fe_3S_4 (van der Veen, 2003; Robb, 2005). Furthermore, bacterially formed FeS_2 is characterized by very small-sized crystals (tens of nm) and occurs as framboidal pyrite whereas chemical precipitated pyrite forms relatively big cubic crystals (van der Veen, 2003).

In the hydrothermal system of Panarea both pyrite shapes occur: cubic crystals in La Calcara and framboidal pyrite in Area 26 (Fig. 46). Therefore, it is reasonable to assume that the pyrite formation has an organic as well as hydrothermal origin. The central, cubic pyrites surrounded by sheaf-like and cockscomb shaped marcasite crystals in La Calcara indicate that marcasite was formed after the crystallization of pyrite. Such well-formed cubic crystals like those of pyrite and galena often require enough time and/or space to grow. Therefore, the crystal growth is time-dependent. It is likely that pyrite acts as nucleus for the crystallization of marcasite. Because mineral precipitation is a spontaneous and sudden process, the transition from one mineral to another would indicate altered circumstances and refer to sudden changes of formation condition like changes in pH, temperature, redox, and/or pressure. Okrusch and Matthes (2014) mentioned the uncertainty about the stabilities of pyrite and marcasite. Thus, the change in the system did not have to be rapidly or had been as quickly as the precipitation of the minerals because the transition from pyrite to marcasite and vice versa is a process merged into one another. Nevertheless, temperature and especially pH give a hint concerning the formation of either pyrite or marcasite.
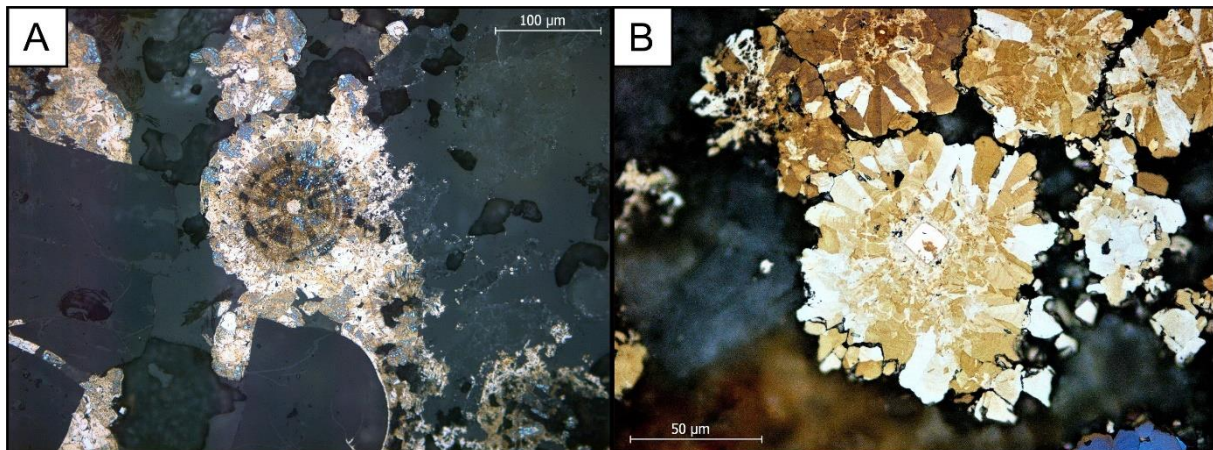
Fig. 46: *Image detail of thin sections VK_06 (A) and VK_20 (B); **A:** Spherical marcasite as cement in A26 with extreme iridescent tarnish, framboidal pyrite in the center; **B:** Radial-oriented marcasite crystals from LC, pyrite as nucleus for marcasite precipitation.*

Marcasite acts as cement in La Calcara and Area 26 pictured in the thin section images in Fig. 21 and 29. In both areas, this mineral precipitates in typical cockscomb shapes and spherulitic aggregates around pyrite, acting as nucleus of crystallization. In Area 26 marcasite shows a flowered structure around framboidal pyrite that differs from the crystallized aggregates of La Calcara. Such crystal and aggregate shapes are common for this mineral and could be related to the different origins (Okrusch and Matthes, 2014; Markl, 2015).

As the name implies, there certainly is a connection between the locations 'Mini Black Point' in Area 26 and Black Point. Also, the results show the same mineral associations in both locations. An assumption is, that these two locations were connected by a fracture following the dominant regional fault system. If a fluid uses the same fracture as pathway and discharges at nearly the same depth, similar mineral associations can be expected. Area 26 is located in the NNE of Black Point which is consistent with the NNE-SSW characterized striking of the major fault. Furthermore, the REE pattern of the fluids from Area 26 and Black Point show the same trends and concentrations indicating the same origin (Fig. 49). A master thesis about the tectonic features of Panarea and its islets is currently in progress. It will give new information about the orientation of minor small-scale fractures which are probably linked to the major fault system. Preexisting papers as the one written by Lucchi et al. (2013) contain information about tectonic features at much larger scales so that small fractures are not displayed on their maps.

5.2   Fe- and Mn- (hydr-) oxide precipitation

The precipitation of Fe and Mn as (hydr-) oxides takes place in nearly the same way. Both elements are closely related to each other because Mn and Fe have similar (geo-)chemical properties which are controlled by the oxidation potential (Robb, 2005). Under acidic and reducing conditions, as found in Panarea, manganese is soluble in form of Mn^{2+}. Under oxidizing conditions with higher pH-values, Manganese in form of Mn^{3+} and Mn^{4+} is less soluble and precipitates as Mn-oxides (Sato, 1992; Zhang and Millero, 1993; Robb, 2005). Furthermore, iron can exist in the oxidation stages II (as in pyrite or marcasite [FeS_2]) and III (as in goethite [$FeOOH$] or hematite [Fe_2O_3]). A comparison of the phase diagrams of manganese and iron in Fig. 47 shows that Mn^{2+} is more resistant to oxidation than Fe^{2+}. This implies that Fe precipitates while Mn rather stays in solution and needs strong oxidizing conditions for precipitation.
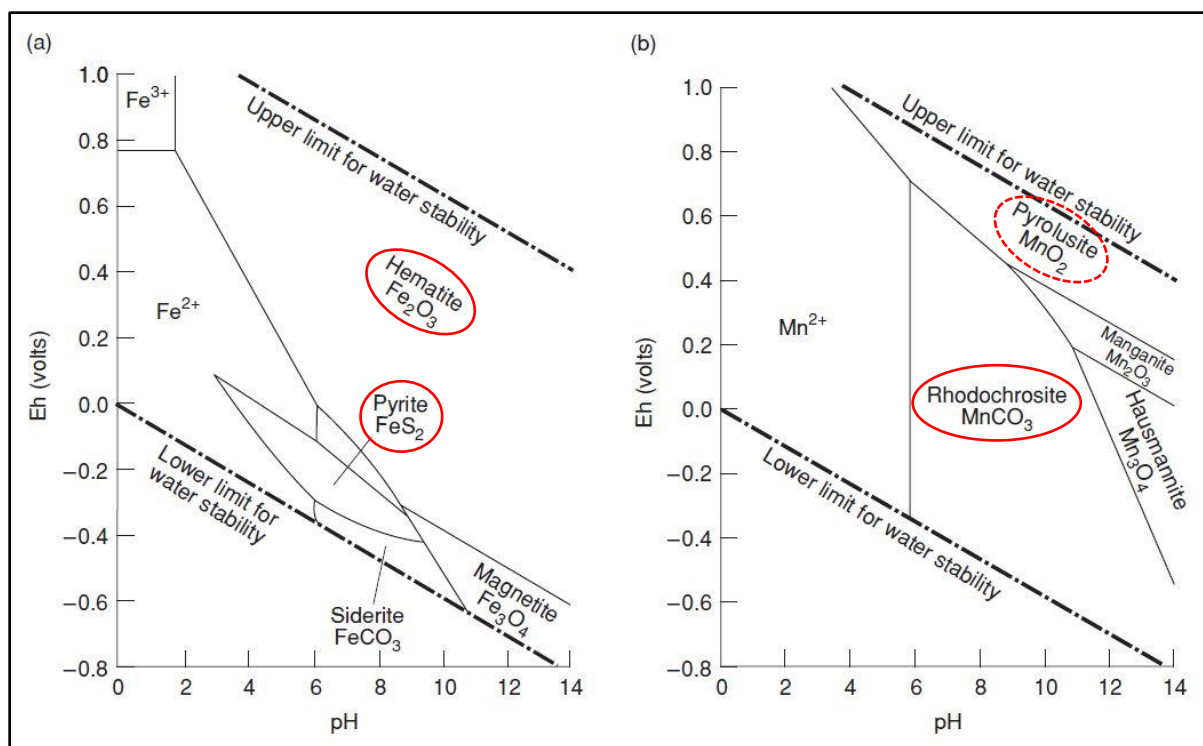
Fig. 47: *Eh-pH diagrams apply to standard conditions: T = 25 °C, p = 1 bar; molarities of Fe, Mn and S are, respectively, 10^{-6}, molarity of CO_3 is 1 (modified after Robb, 2005), marked with red: minerals of interest; **(a)** Eh-pH diagram with stability fields of common Fe species; **(b)** Eh-pH diagram with stability fields of common Mn minerals.*

Iron compounds like FeS_2 precipitate more readily in acidic and reducing environments than manganese oxides or carbonates. Such reducing conditions are present in the area around Panarea. First, the precipitation of Fe^{2+} in form of pyrite and marcasite takes place. With further mixing of the hydrothermal fluids with ambient sea water, dissolved iron is oxidized to Fe^{3+}. Later, goethite and/or hematite precipitate(s), which is the reason why these minerals form the outer part of the sulfide crust around single grains e.g. in Point 21 or La Calcara.

The exposed dacitic bedrock at Point 21 is in direct contact with the sea water. The ambient water is enriched in oxygen relative to the emitted fluids which leads to neutralization of the acid sulfate fluids due to sea water-fluid mixing. Furthermore, the volcanic rock is leached with respect to transition metals. The result is the formation of an iron(hydr)-oxide crust as well as the formation of elemental sulfur according to the reaction equation (2). In fissures, where the fluids are more protected against sea water mixing, precipitation of sulfide minerals at lower temperatures and acidic pH takes place.

Manganese precipitates were found as thin coating around pebbles at Fumarolic Field, as thin Fe-Mn-layers at Black Point (Becke, 2009) and as Mn-carbonate (rhodochrosite) in La Calcara at 'Mordor' and 'Black Rock' (Kakuk, 2016). Focused discharge at Fumarolic Field has a minimum pH-value of 5.4 (see table of extreme values in the appendix: Tab. 12).

Consequently, the fluids at this location have the highest pH-values of the investigation area. It is also a relatively shallow-situated location with 17 m of water depth.

Near-surface water is in direct contact to the atmospheric oxygen. Gas exchange takes place at the water surface so that the upper water layer is enriched in oxygen compared to water in greater depths. Tidal currents and wind carry oxygenated water with pH of 8.2 (measured value) to the depths of the hydrothermal environment. Fig. 48 displays a map of tectonic lineaments and fractures by Lucchi et al. (2013) including the location of the diving sites. Fumarolic Field is located within this tectonic zone on parts of a bigger fault. Consequently, sea water circulating within fault zones reaches deeper into ascending hydrothermal flows beneath the seafloor. Thus, discharging fluids at Fumarolic Field are continuously mixed with sea water. The elevated O_2 content leads to higher oxidation potentials and more neutral to alkaline conditions. This favors the oxidation of Mn^{2+} to Mn^{3+}/Mn^{4+}.
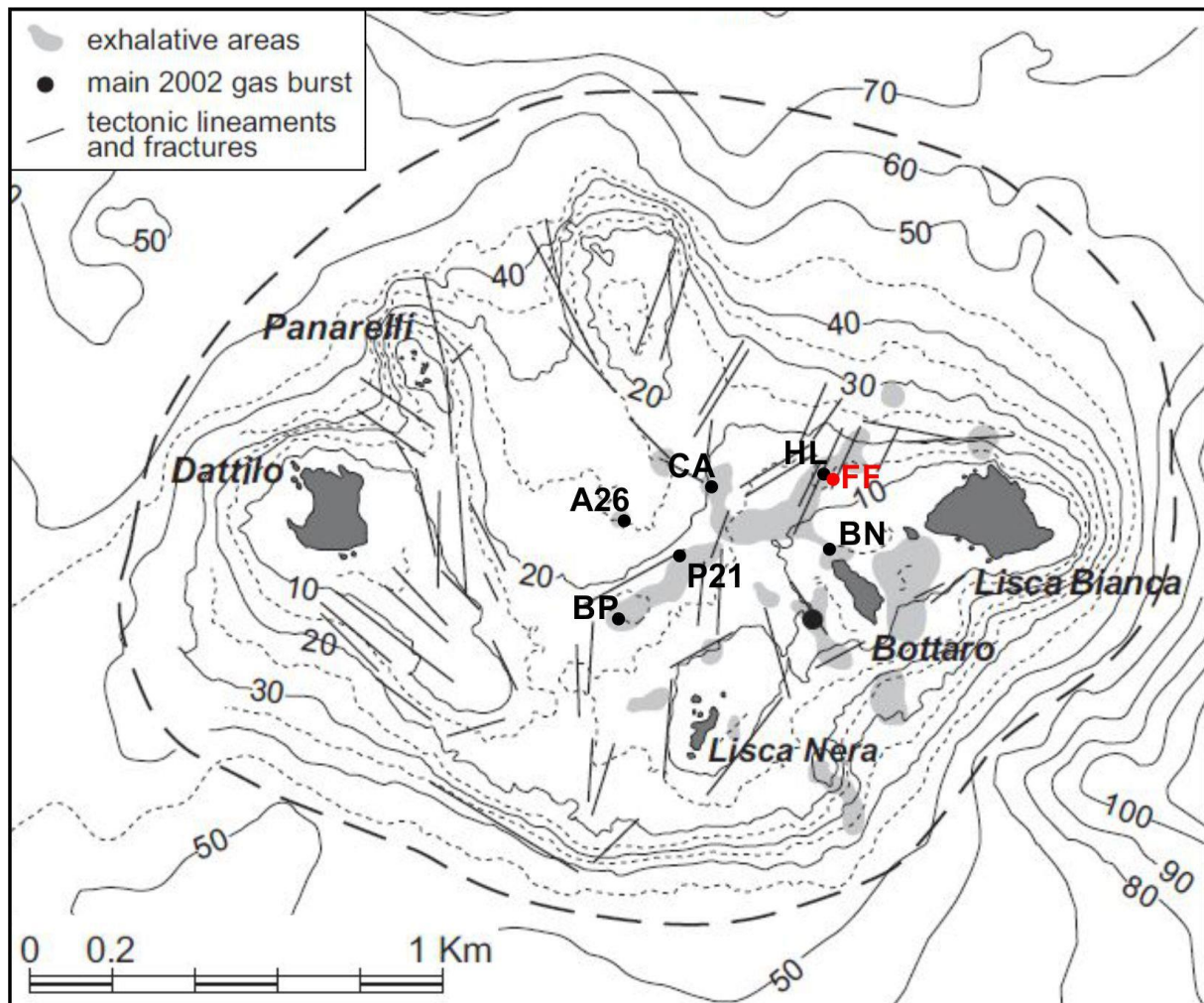
Fig. 48: *Structural features within the islets in the east of Panarea and locations of the diving sites (modified after Lucchi et al., 2013). A precise plotting of these sites was not possible due to the missing coordinates of the map, but according to exhalative areas the locations were plotted as accurately as possible.*

The oxidation and precipitation of Mn-minerals at Fumarolic Field as a consequence of fluid mixing with Mediterranean sea water was modeled with PHREEQC. Modeling results reveal a positive SI (saturation index) only for rhodochrosite at pH 7-8 (Tab. 11). An oversaturation of manganese(hydr)-oxide with PHREEQC was not possible, but the EDX results have proven the Mn existence as (hydr-) oxide coating (cf. Fig. 42, Tab. 10). It is likely that $MnCO_3$ precipitates at circum-neutral pH-values due to the mixing of the fluids with sea water and later subsequent oxidation and alteration to Mn-oxides.

Tab. 11: *SI values for Mn minerals calculated with PHREEQC (with the aid of B. Merkel), first column contains mixing ratio of sea water with hydrothermal fluid from FF (e.g. 0.05 = 5 %); in red: positive SI (oversaturation) can cause mineral precipitation.*

	pH	pe	SI_Mn_2O_3	SI_$MnCO_3$	SI_Mn_3O_4	SI_$Mn(OH)_2$	SI_MnO_2
Sea water	8.2	8					
Hydrothermal	5	-1					
0.1	6.52	5.95	-3.96	-0.27	-6.75	-6.30	-5.85
0.05	7.22	4.95	-3.17	**0.08**	-5.34	-5.20	-6.18
0.04	7.47	4.47	-3.00	**0.21**	-4.87	-4.80	-6.42
0.03	7.70	4.02	-2.87	**0.29**	-4.53	-4.46	-6.68
0.02	7.90	3.72	-2.76	**0.28**	-4.36	-4.24	-6.85
0.01	8.06	3.63	-2.67	**0.10**	-4.42	-4.22	-6.86
0.005	8.13	3.75	-2.63	-0.15	-4.62	-4.37	-6.70

The ongoing circulation of sea water (pH of 8.2) provides the system with oxygen and the continuous flow of acidic fluids causes variations in pH. Under acidic conditions rhodochrosite is not stable which results in the alteration to manganese oxide seen as dark brown coating of the pebbles at Fumarolic Field. Please note: the mineral stabilities in Fig. 47 apply to standard conditions (T = 25 °C, p = 1 bar). Boundary conditions of the stability fields depend on temperature and pressure changes causing the Eh-pH diagrams to look slightly different at local parameters.

5.3 Clay

Due to their wide range in concentration, which is larger than for major elements, trace element abundances can be used to indicate the origin of fluids. Rare earth elements (REE), for example, provide information about alteration or weathering processes in sedimentary areas (Frost and Frost, 2013). The diagram below (Fig. 49) shows chondrite-normalized REE abundances creating mainly smooth curves. The trend is ascending for Area 26, Black Point and Cave whereas the curves from Bottaro North, Fumarolic Field, Hot Lake, La Calcara and Point 21 gradually descend. Cerium (Ce) and europium (Eu) constitute exceptions but

the observed cerium anomaly could not be further examined. The positive Eu anomaly of the fluids of distinct locations indicates hydrothermal alteration of the plagioclases (Frost and Frost, 2013). Rare earth elements are generally incompatible which means that these elements favor the aqueous phase of a system and are therefore concentrated in the hydrothermal waters. Eu, however, behaves like a compatible element in plagioclase-bearing systems. Plagioclase preferentially concentrates Eu so that upon its weathering an enrichment of this element occurs in the solution compared to the other REE (personal communication with W. Bach).
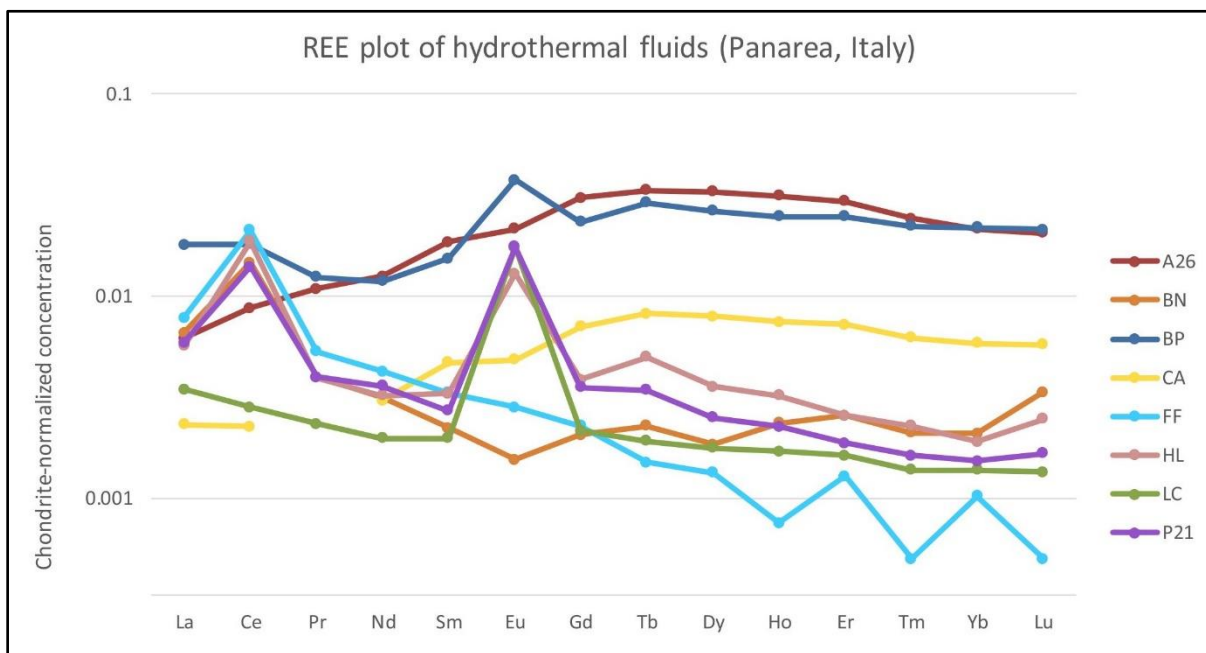
Fig. 49: *Chondrite-normalized REE diagram of the hydrothermal fluids (Tab. 12 in the appendix). Similar trend of A26, BP and CA, comparable in respect of element concentration except CA; clearly recognizable positive Eu anomaly of the fluids from HL, LC, P21, and a slight anomaly in BP. Data from McDonough and Sun (1995). See Tab. 14 for normalized values.*

Clay samples used in this thesis were not taken during the last field trip because previous excursions have shown that various types of clay minerals are common in the investigation area. In Area 26 alunitic clay is found at the bottom of the '3-bowl' structure. Localized, such clays were also found within the sediment of Hot Lake as isolated lenses. Because of the ovate shape, these lenses are called 'dragon eggs'. Furthermore, beneath the recent sands of La Calcara mainly alunite and lesser smectite are widely distributed over the total area but were mixed with fine-grained sand (Prautsch et al., 2013).

The predominant clay around Panarea is made of alunite and minor smectite (Prautsch et al., 2013). They result from the hydrothermal alteration of silicate minerals. Alunite is a potassium-enriched, white to gray colored clay mineral, commonly formed as a weathering product of alkali feldspar (Lever and Fanning, 2004). The sulfur required for the formation of

alunite is provided by the fluids of the hydrothermal system of Panarea. The acidity of the fluids and the supply of SO_4^{2-} is described in the chemical equations (1) and (2) above. Another possible reaction to produce sulfuric acid is the oxidation of H_2S near or above the ground water surface at temperatures ranging from 90 to 180 °C (Höller, 1967). Oxidation of this sulfuric species is also possible due to the contact with oxygen dissolved in the sea water (Zhang and Millero, 1993):

$$H_2S + 2\,O_2 \quad = \quad HSO_4^- + H^+ \quad = \quad SO_4^{2-} + 2\,H^+ \qquad (5)$$
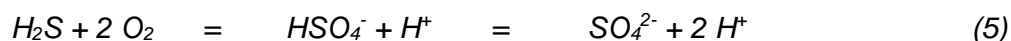
The high potassium calc-alkaline dacitic and andesitic rocks of Panarea and its small islands (Calanchi et al., 2002; Esposito et al., 2006; Lucchi et al., 2013) show a remarkable amount of potassium (between 1 and 6 wt-% K_2O) (Sarbas and Nohl, access date 18/10/2018). The volcanic rocks contain 10-15 % of plagioclase phenocrysts and a few percent of clinopyroxenes and amphiboles (Esposito et al., 2006). Because these rocks have only a small proportion of alkali feldspars, the potassium for the alunite formation originates from the rocks themselves as part of hydrothermal alteration of the groundmass.

Due to the geochemical composition and the elements provided by the acidic fluids, alunite is formed out of plagioclase according to the following reactions (modified after Höller, 1967):

$$3\,Ca[Al_2Si_2O_8] + 2\,K^+ + 12\,H^+ + 6\,SO_4^{2-} = 2\,KAl_3[(OH)_6|(SO_4)_2] + 6\,SiO_2 + 3\,Ca^{2+} + 2\,SO_4^2 \quad (6)$$

$$3\,Na[AlSi_3O_8] + K^+ + 6\,H^+ + 3\,SO_4^{2-} \quad = \quad KAl_3[(OH)_6|(SO_4)_2] + 9\,SiO_2 + 3\,Na^+ + SO_4^{2-} \quad (7)$$
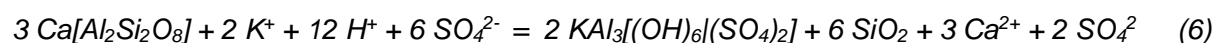
Both endmembers of plagioclase, anorthite and albite, can act as reactant for the alunite formation. Ca and Na remain as dissolved ions in the liquid phase depending on temperature and pH of the hydrothermal water. The fluid data show a higher concentration of these cations compared to the surrounding sea water which indicates that Ca^{2+} and Na^+ mainly stay in solution. The SiO_2 can precipitate as sedimentary-formed quartz or chalcedony in the vicinity of the educts or stay in solution depending on temperature and pH of the fluids (Höller, 1967; Okrusch and Matthes, 2014). A precursor mineral for the alunite formation can be pyrite and/or marcasite as well. If these sulfidic minerals were oxidized, sulfate would be derived for the reaction.
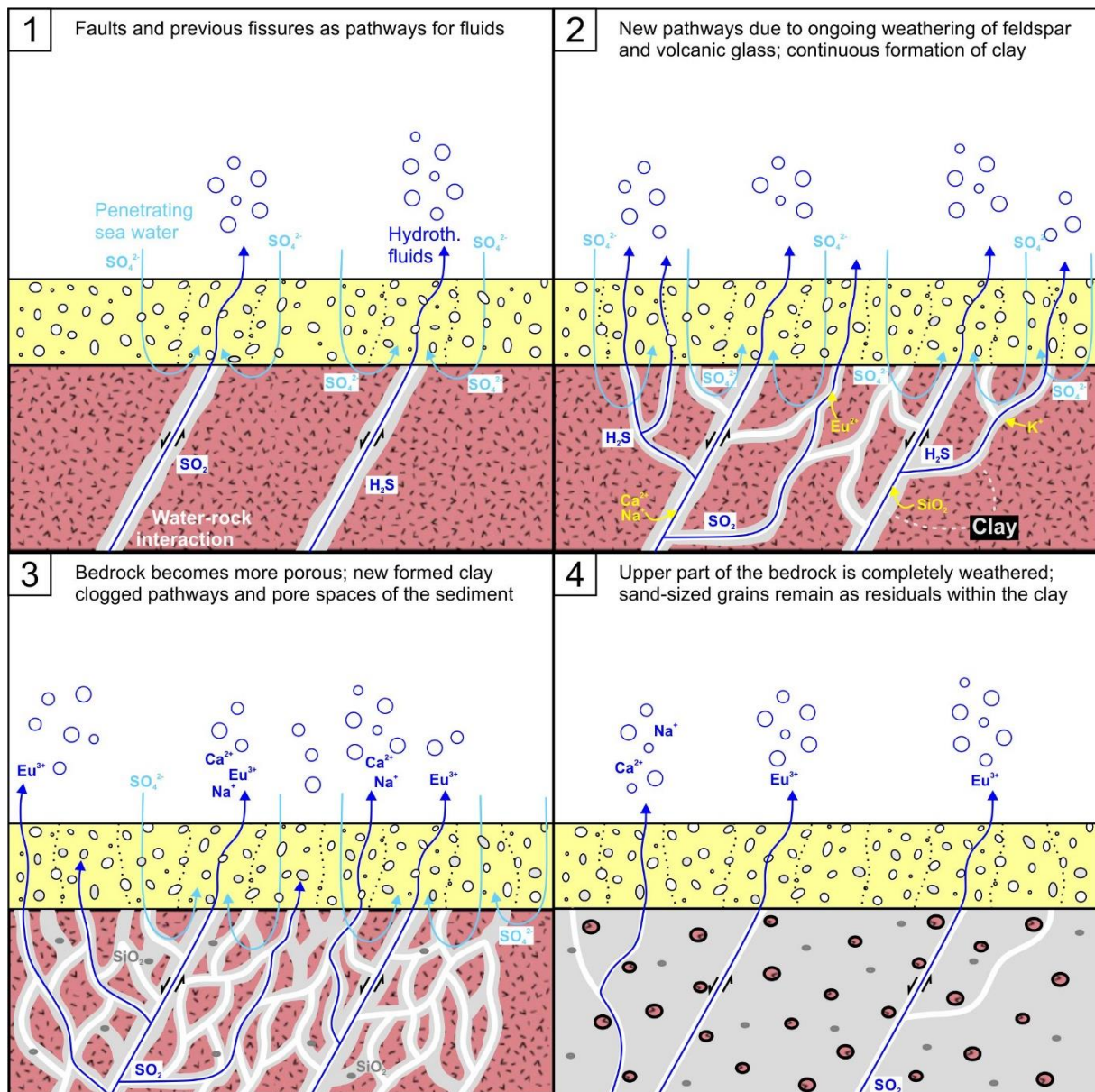
Fig. 50: *Formation of clay as a result of the alteration of high-potassium calc-alkaline dacitic and andesitic rocks;*
1: *Faults and fissures act as initial pathways for hydrothermal fluids, sea water penetrates through the sediment and reaches the bedrock;* ***2:*** *Due to the aggressive, acidic character of the fluids and high water-rock interaction, silicate minerals, especially (Eu-bearing) plagioclase, and volcanic glass are hydrothermal altered, clay precipitates in the direct vicinity of the altered minerals, other elements were dissolved and transported further upwards;* ***3:*** *Element-enriched fluids reach the seafloor where they can be sampled, clay formation continues, probable clogging of some pathways because of impermeability of clay, dissolved SiO_2 precipitates as quartz or chalcedony grains;* ***4:*** *At some point, nearly the complete upper part of the bedrock is hydrothermally decomposed, clay with sand-sized residuals of the volcanic rock, insoluble minerals like quartz and new formed SiO_2 remain.*

Clay is found in La Calcara predominantly beneath the recent sediment cover mixed with a small amount of fine-grained sand, which is composed of grains with dacitic composition and quartz (Kakuk, 2016). In Hot Lake, alunitic clay occurs only as egg-shaped lenses and in Area 26 merely at the bottom of the '3-bowls'.

The genesis model of the clay formation in La Calcara is described in Fig. 50. Hydrothermal gases and hot acidic waters migrate along faults and fractures through the high-potassium calc-alkaline bedrock. The aggressive, acidic, and reducing character of the fluids allows high water-rock interaction and alteration of the rock-forming minerals and volcanic glass. Plagioclases are affected as well as the groundmass of the volcanic rocks resulting in the dissolution of Al, Ca, K and Na. The cooler circulating Mediterranean sea water penetrates the sediment and the seafloor. There, it gets in contact with the enriched hot waters and causes changes in temperature and pH resulting in the precipitation of alunite and probably other clay minerals.

The formation of alunite occurs in-situ and is a slow diagenetic alteration process. It needs temperatures of 90 to 180 °C as well as sulfur-acidic solutions (Höller, 1967). The bedrock will be continuously altered as long as the hydrothermal system is active. At some point, the upper part of the bedrock is almost completely hydrothermally decomposed. Fragments of rocks and insoluble minerals, e.g. quartz, remain as sand-sized grains within the clay.

In Hot Lake, tuff clasts were found in previous diving excursions (see Stanulla, 2012; Ganß, 2013). Beside (K-)feldspars, other clays and sulfide minerals, tuff is a probable precursor for the alunite formation (Lever and Fanning, 2004). Tuffaceous layers have a high porosity and good permeability. This leads to an encouraged fluid flow within the layer compared to the surrounding sediment. Thus, alteration to alunite occurs merely in lenses and thin layers (Lever and Fanning, 2004). The positive Eu anomaly of the fluids of Point 21 indicates alunitization of plagioclase. The resulting clay formation, however, does not occur at this location. The bedrock is exposed to the seafloor without or only a thin sediment cover as a protection against wave action and ground currents. Therefore, the clay is carried away.

5.4　N$_2$-samples

To analyze mineral alteration conventionally taken samples were compared with the corresponding N$_2$-samples. For this analytical method a small air-tight box was used to guarantee a continued protective and oxygen free atmosphere.
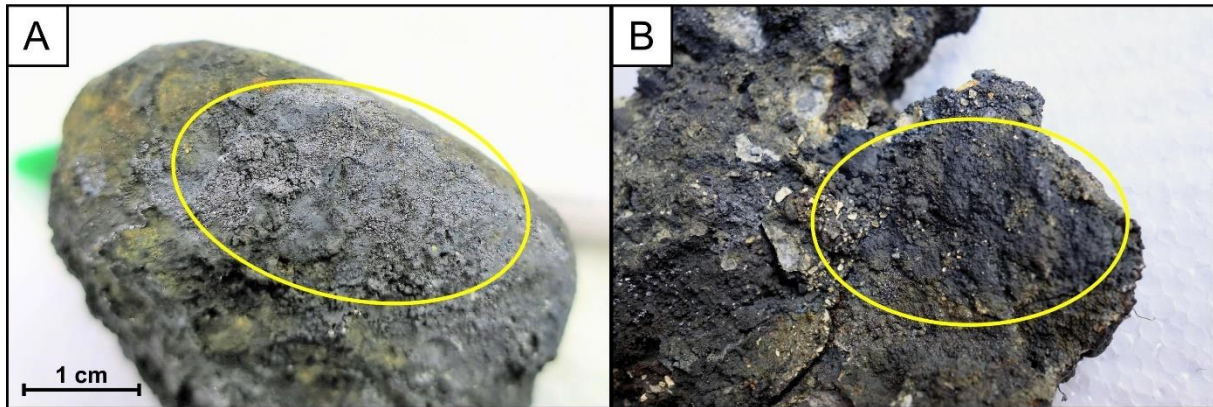
Fig. 51: *Comparison of sampling methods and their appearance;* ***A:*** *N$_2$-sample from BP, lead-gray galena with metallic luster;* ***B:*** *Conventionally taken sample exposed to atmospheric oxygen, anthracite-colored and mat.*

Differences in respect to the presence of other minerals were not detected with µXRD, but variations in optical properties are apparent. Sulfide ore minerals taken under N$_2$ protection and stored in a glove box still have a metallic luster and their typical color (Fig. 51, A). Being exposed to atmospheric oxygen for a certain time, the minerals lose their luster and become matt (Fig. 51, B).
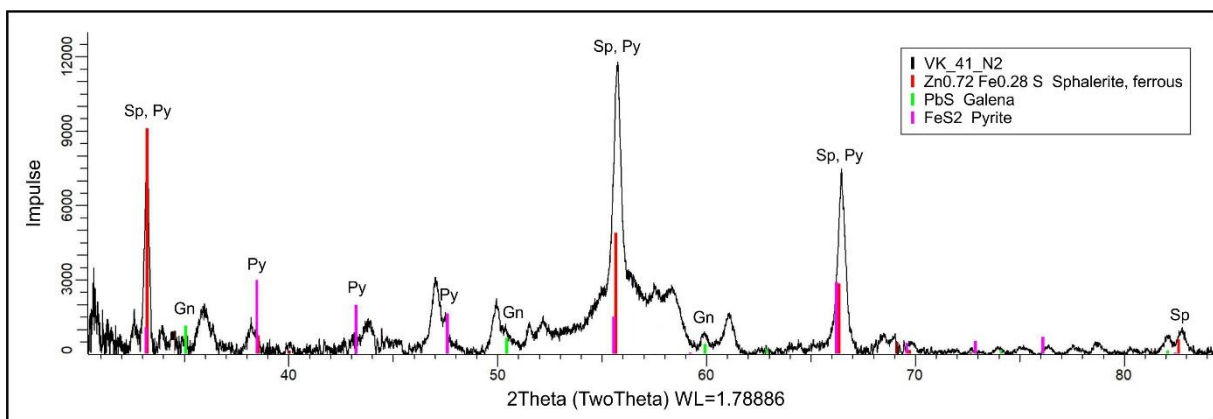
Fig. 52: *Diffractogram of the N$_2$-sample VK_41 from BP.*
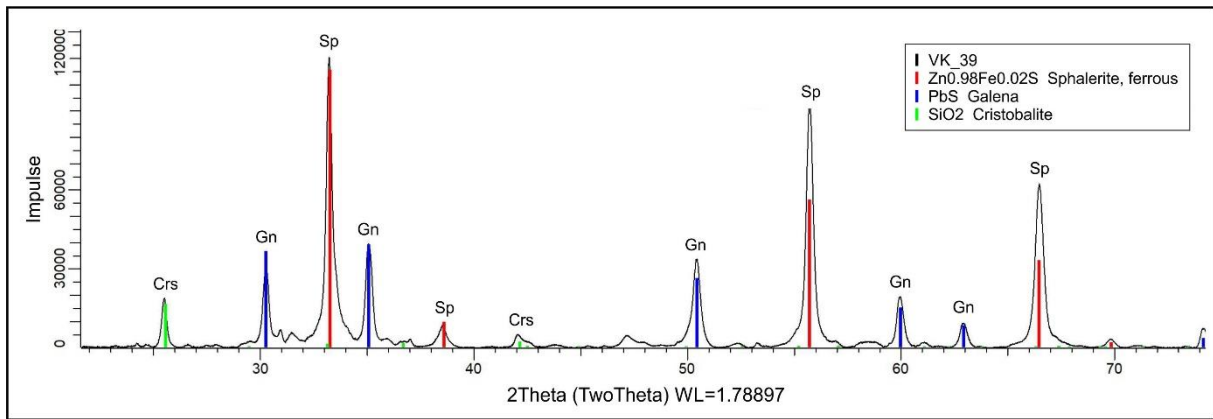
Fig. 53: *Diffractogram of the conventionally taken sample VK_39 from BP.*

Results of the µXRD analyses, displayed in Fig. 52 and 53, reveal no changes or differences in the mineralogy, but it is obvious that oxidation took place. Hence, it is very likely that the oxidation layer around a mineral acts as a protective coating. If this shielding layer is developed completely, the underlying mineral is not affected by oxidation anymore.

In respect to the energy and the resulting penetration depth of the X-ray beam and the extremely low thickness of the oxidation layer (probably in nm-scale), the laser probably shot through this coating and penetrated right down to the unaffected mineral. For that reason, no differences are noticeable. A background noise occurs only at the diffractograms of the N_2-samples (compare Fig. 52 and 53) and is the result of the plastic, air-tight box which ensures the protective atmosphere.

6   Conclusion

In the shallow-marine hydrothermal system of Panarea, mineral precipitation depends on temperature, pH-value, redox potential, supply of metal-enriched, acidic fluids and the amount of sea water mixing with them. The latter results in higher pH-values and lower temperatures of the hydrothermal fluids. Furthermore, secondary mineral precipitation is closely related to (active) faults, fractures and fissures. These tectonic features act as pathways. Due to fast ascent of hot gases and water, erosion of possible mineral precipitates takes place and consequently larger pathways stay open. The supply of fluids depends on permeability of sediments and the underlying bedrock as well. During the ascent of hydrothermal fluids, the minerals can precipitate and occur therefore disseminated in the sediment or as cement. This leads to the decrease of permeability.

Fluids in the Panarea system are interpreted as black smoker type or acid sulfate fluids. In Area 26, Black Point and Point 21 sulfide minerals, which precipitate out of the hot waters, are in accordance with mineral associations of black smokers. However, the high content of dissolved sulfide species in the fluids results in high acidity and the occurrence of elemental sulfur at all locations according to the reaction equations (1)-(3). Besides sulfur, the most abundant secondary minerals are marcasite and pyrite followed by sphalerite, galena and rhodochrosite. Probable oxidation products as sort of tertiary mineral phases are MnO_2-type minerals and iron(hydr)-oxides. Manganese carbonate and FeS_2 as precursor minerals were oxidized in areas where sea water can easily penetrate the seafloor and mixes with the fluids. Additionally, products of hydrothermal alteration are alunite and SiO_2 which originate from the bedrock and tuffaceaous layers. In case of alunite, Fe-sulfide minerals can be precursors as well.

The named minerals develop in different but mainly reducing environments. Metal(hydr)-oxides prefer oxic, neutral to alkaline conditions whereas sulfidic species likely precipitate in anoxic settings (Fig. 54). Elemental sulfur is unlisted because it occurs in both environments and in a wide pH-range. Certain minerals are distinctive for their formation conditions. Marcasite, for example, favors to precipitate in acidic solutions whereas at pH-values more than 6 only pyrite is formed. With increasing oxygen content, these two FeS_2 minerals were oxidized to hematite and/or goethite.
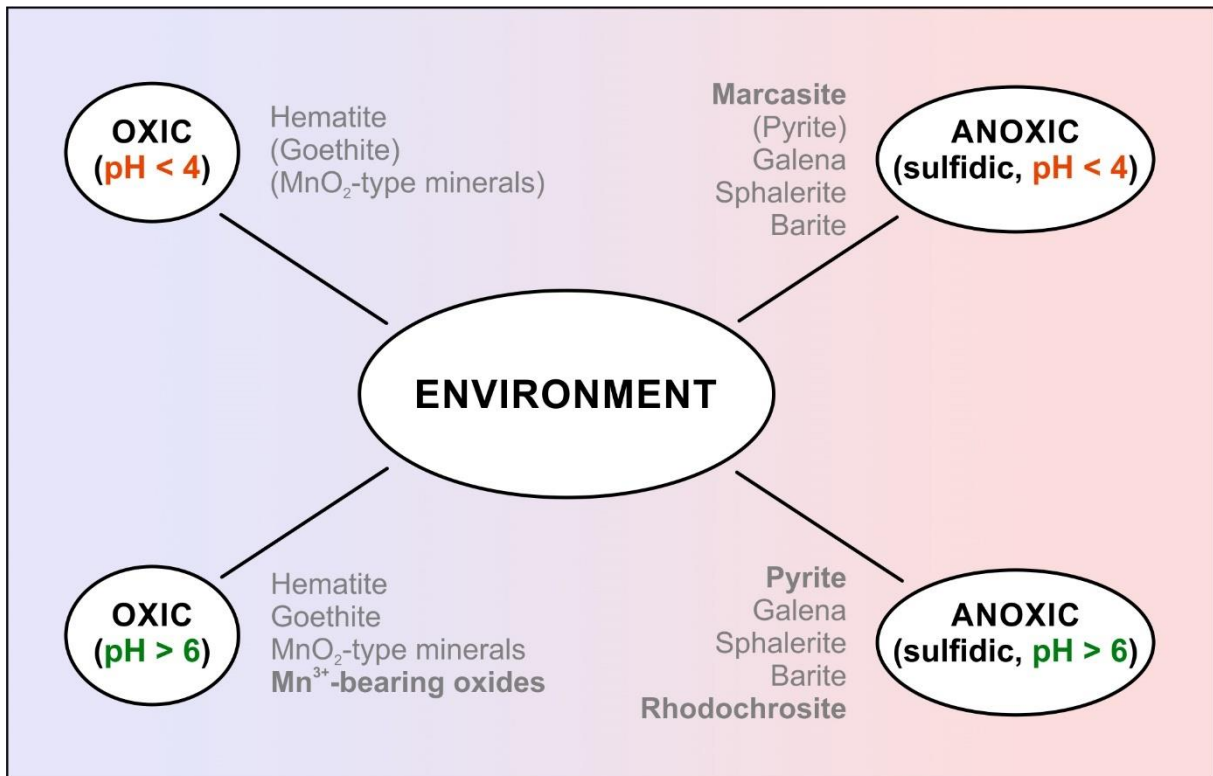
Fig. 54: Scheme of minerals occurring in the hydrothermal system of Panarea at certain environmental conditions. Words in bold indicate characteristic minerals in their respective environment.

The dynamic of the system causes variations of distinct parameters. Ongoing subduction and volcanic activity affect the amount of discharging fluids and their SO_2 content. Tectonic features coupled with ground and tidal currents lead to changes in redox potential due to the mixture of fluids with ambient sea water. Furthermore, seasonal variations play an important role. During winter, water temperatures are lower, and storms are more violent than during summer.

Oxidation processes and consequent alterations of the secondary minerals were analyzed by comparison of conventionally taken samples with samples under N_2 protection. Analyses have shown that differences can be seen optically, but not in mineralogy. A thin oxidation layer protects the underlying mineral from further alteration.

If the composition of the oxidation layer should be considered more closely, X-ray Reflection (XRR) is a suitable method. The XRR uses total reflection of radiation at interfaces so that layer thicknesses in the range from 3 to 300 nm can be measured non-destructively (Schreier, 2016).

References

Aliani, S.; Bortoluzzi, G.; Caramanna, G.; Raffa, F. (2010): Seawater dynamics and environmental settings after November 2002 gas eruption off Bottaro (Panarea, Aeolian Islands, Mediterranean Sea). In: *Continental Shelf Research* 30 (12), pp. 1338–1348.

Anon. (2017): Micro X-ray Diffraction (µXRD) | XOS. [online] https://xos.com, last update 2017, access date 08/09/2018.

Becke, R. (2009): Mineralogical and geochemical characteristics of the shallow-water massive sulfide precipitates of Panarea, Aeolian Islands, Italy. Unpublished Diploma Thesis, TU Bergakademie Freiberg.

Berner, R. A. (1985): Sulphate reduction, organic matter decomposition and pyrite formation. In: *Phil. Trans. R. Soc. Lond. A* 315 (1531), pp. 25–38.

Calanchi, N.; Peccerillo, A.; Tranne, C.A.; Lucchini, F.; Rossi, P.L.; Kempton, P. et al. (2002): Petrology and geochemistry of volcanic rocks from the island of Panarea: implications for mantle evolution beneath the Aeolian island arc (southern Tyrrhenian sea). In: *Journal of Volcanology and Geothermal Research* 115 (3-4), pp. 367–395.

Capaccioni, B.; Tassi, F.; Vaselli, O.; Tedesco, D.; Poreda, R. (2007): Submarine gas burst at Panarea Island (southern Italy) on 3 November 2002: A magmatic versus hydrothermal episode. In: *J. Geophys. Res.* 112 (B5), pp. 222.

Dekov, V. M.; Kamenov, G. D.; Abrasheva, M. D.; Capaccioni, B.; Munnik, F. (2013): Mineralogical and geochemical investigation of seafloor massive sulfides from Panarea Platform (Aeolian Arc, Tyrrhenian Sea). In: *Chemical Geology* 335, pp. 136–148.

Dutrow (2006): Fossil Black Smoker - Massive Sulfides. [online] http://geol.lsu.edu, last update 8/27/2006, access date 19/11/2018.

Ellis, A. J.; Mahon, W.A.J. (1964): Natural hydrothermal systems and experimental hot-water/rock interactions. In: *Geochimica et Cosmochimica Acta* 28 (8), pp. 1323–1357.

Esposito, A.; Anzidei, M.; Atzori, S.; Devoti, R.; Giordano, G.; Pietrantonio, G. (2010): Modeling ground deformations of Panarea volcano hydrothermal/geothermal system (Aeolian Islands, Italy) from GPS data. In: *Bull Volcanol* 72 (5), pp. 609–621.

Esposito, A.; Giordano, G.; Anzidei, M. (2006): The 2002–2003 submarine gas eruption at Panarea volcano (Aeolian Islands, Italy): Volcanology of the seafloor and implications for the hazard scenario. In: *Marine Geology* 227 (1-2), pp. 119–134.

Frost, B. R.; Frost, C. D. (2013): Essentials of igneous and metamorphic petrology: Cambridge University Press.

Gamberi, F.; Marani, M.; Savelli, C. (1997): Tectonic, volcanic and hydrothermal features of a submarine portion of the Aeolian arc (Tyrrhenian Sea). In: *Marine Geology* 140 (1-2), pp. 167–181.

Gamo, T.; Chiba, H.; Masuda, H.; Edmonds, H. N.; Fujioka, K.; Kodama, Y. et al. (1996): Chemical characteristics of hydrothermal fluids from the TAG Mound of the Mid-Atlantic Ridge in August 1994: Implications for spatial and temporal variability of hydrothermal activity. In: *Geophys. Res. Lett.* 23 (23), pp. 3483–3486.

Ganß, R. (2013): Geochemische und kleinmorphologische Untersuchungen am Beispiel Area 26, Panarea, Italien. Unpublished Bachelor Thesis, TU Bergakademie Freiberg.

He, B. B. (2004): Microdiffraction using two-dimensional detectors. In: *Powder Diffr.* 19 (2), pp. 110–118.

Hildebrand, M.-C. (2013): Charakterisierung von sedimentären Ablagerungen und Präzipitaten des Arbeitsgebietes Black Point nahe der Insel Panarea (Italien). Unpublished Bachelor Thesis, TU Bergakademie Freiberg.

Höller, H. (1967): Experimentelle Bildung von Alunit-Jarosit durch die Einwirkung von Schwefelsure auf Mineralien und Gesteine. In: *Contr. Mineral. and Petrol.* 15 (4), pp. 309–329.

Inguaggiato, S.; Diliberto, I. S.; Federico, C.; Paonita, A.; Vita, F. (2018): Review of the evolution of geochemical monitoring, networks and methodologies applied to the volcanoes of the Aeolian Arc (Italy). In: *Earth-Science Reviews* 176, pp. 241–276.

Italiano, F.; Nuccio, P. M. (1991): Geochemical investigations of submarine volcanic exhalations to the east of Panarea, Aeolian Islands, Italy. In: *Journal of Volcanology and Geothermal Research* 46 (1-2), pp. 125–141.

James, R. H.; Green, D. R.H.; Stock, M. J.; Alker, B. J.; Banerjee, N. R.; Cole, C. et al. (2014): Composition of hydrothermal fluids and mineralogy of associated chimney material on the East Scotia Ridge back-arc spreading centre. In: *Geochimica et Cosmochimica Acta* 139, pp. 47–71.

Kakuk, F. (2016): Entstehung der Präzipitate im Geothermalgebiet La Calcara (Panarea, Italien). Unpublished Master Thesis, TU Bergakademie Freiberg.

Leng, Y. (2013): Materials characterization. Introduction to microscopic and spectroscopic methods. 2. Edition. Weinheim: Wiley VCH. 376 pp.

Lever, H.; Fanning, C. M. (2004): Alunite alteration of tuffaceous layers and zircon dating, Upper Permian Kennedy Group, Carnarvon Basin, Western Australia. In: *Aust J Earth Sci* 51 (2), pp. 189–203.

Lowell, R. P.; Rona, P. A.; Herzen, R. P. von (1995): Seafloor hydrothermal systems. In: *J. Geophys. Res.* 100 (B1), pp. 327–352.

Lucchi, F.; Tranne, C. A.; Peccerillo, A.; Keller, J.; Rossi, P. L. (2013): Chapter 12 Geological history of the Panarea volcanic group (eastern Aeolian archipelago). In: *Geological Society, London, Memoirs* 37 (1), pp. 351–395.

Manini, E.; Luna, G. M.; Corinaldesi, C.; Zeppilli, D.; Bortoluzzi, G.; Caramanna, G. et al. (2008): Prokaryote diversity and virus abundance in shallow hydrothermal vents of the Mediterranean Sea (Panarea Island) and the Pacific Ocean (north Sulawesi-Indonesia). In: *Microbial ecology* 55 (4), pp. 626–639.

Markl, G. (2015): Minerale und Gesteine. Mineralogie – Petrologie – Geochemie. 3. Auflage. Berlin, Heidelberg: Springer Berlin Heidelberg. 619 pp.

McDonough, W. F.; Sun, S.-S. (1995): The Composition of the Earth. In: *Chemical Geology* 120, pp. 223–253.

Okrusch, M.; Matthes, S. (2014): Mineralogie. Einführung in die spezielle Mineralogie, Petrologie und Lagerstättenkunde. 9. Auflage. Berlin, Heidelberg: Springer Berlin Heidelberg. 726 pp.

Pichler, T. (2009): Marine shallow-water hydrothermal systems as natural laboratories. In: *Freiberg Online Geology* 22, pp. 77–81.

Pohl, T.; Becke, R.; Ganß, R.; Stanulla, R.; Merkel, B. (2009): Mineralogical and geochemical characteristics of the shallow-water massive sulfide precipitates of Panarea, Aeolian Islands, Italy. In: *Freiberg Online Geology* (Vol. 22), pp. 94–100.

Prautsch, A.; Stanulla, R.; Pohl, T.; Merkel, B. (2013): Geochemical-mineralogical investigation of degassing structures caused by recent volcanic hydrothermalism - case study: La Calcara, Isle of Panarea (Italy).

Robb, L. (2005): Introduction to Ore-Forming Processes. Cornwell (UK): Blackwell Science Ltd. 386 pp.

Sarbas and Nohl (2018): Geochemical Rock Database-Query. GWDG Göttingen. [online] http://georoc.mpch-mainz.gwdg.de, last update 1/10/2018, access date 18/10/2018.

Sato, M. (1992): Persistency-field Eh-pH diagrams for sulfides and their application to supergene oxidation and enrichment of sulfide ore bodies. In: *Geochimica et Cosmochimica Acta* 56 (8), pp. 3133–3156.

Schoonen, M. A.A. (2004): Mechanisms of sedimentary pyrite formation. In: *Geological Society of America Special Paper* 379, pp. 117–134.

Schoonen, M.A.A.; Barnes, H.L. (1991): Mechanisms of pyrite and marcasite formation from solution: III. Hydrothermal processes. In: *Geochimica et Cosmochimica Acta* 55 (12), pp. 3491–3504.

Schreier, S. (2016): Kristallanalyse mittels Röntgendiffraktometrie (XRD). Universität Stuttgart.

Seewald, J. S.; Reeves, E. P.; Bach, W.; Saccocia, P. J.; Craddock, P. R.; Shanks, W. C. et al. (2015): Submarine venting of magmatic volatiles in the Eastern Manus Basin, Papua New Guinea. In: *Geochimica et Cosmochimica Acta* 163, pp. 178–199.

Stanulla, R. (2012): Geological record of submarine hydrothermal gas and water escape structures - morphology and geochemistry of the recent volcanic system of Panarea, Italy. Unpublished Master Thesis, TU Bergakademie Freiberg.

Stanulla, R.; Pohl, T.; Müller, C.; Engel, J.; Hoyer, M.; Merkel, B. (2017): Structural and mineralogical study of active and inactive hydrothermal fluid discharges in Panarea, Italy. In: *Environ Earth Sci* 76 (11), pp. 1338.

Steinbrückner, D. (2009): Quantification of submarine degassing of Panarea Volcano in the Aeolian archipelago, Italy. In: *Freiberg Online Geology* (Vol. 23), pp. 1–113.

Tassi, F.; Capaccioni, B.; Caramanna, G.; Cinti, D.; Montegrossi, G.; Pizzino, L. et al. (2009): Low-pH waters discharging from submarine vents at Panarea Island (Aeolian Islands, southern Italy) after the 2002 gas blast: Origin of hydrothermal fluids and implications for volcanic surveillance. In: *Applied Geochemistry* 24 (2), pp. 246–254.

van der Veen, A. (2003): Schwefelspeziation und assoziierte Metalle in rezenten Sedimenten. Doctoral Dissertation, TU Carolo-Wilhelmina Braunschweig.

Zhang, J.-Z.; Millero, F. J. (1993): The products from the oxidation of H2S in seawater. In: *Geochimica et Cosmochimica Acta* 57 (8), pp. 1705–1718.

List of figures

vi

List of tables

Appendix

Tab. 12: Extreme values of fluids (2006-2017)

	unit	Vulcano sea water	A26	BN	BP	CA	FF	HL	LC	P21
pH		8.2	4.5	5.3	2.4	4.8	5.4	4.4	4.6	4.7
temp	°C	25.0	58.4	65.1	134.1	40.2	60.0	78.7	116.0	74.0
EC	mS/cm	48.0	68.7	60.8	82.0	54.9	70.9	114.3	64.8/39.7	60.5
O2	%	100.0	6.7	16.5	16.7	0.5	14.6	0.6	0.60	4.8
O2	mg/l	7.8	0.5	1.3	1.1	2.8	1.2	0.0	0.04	0.4
Eh	mV	400	2	7	10	-30	3	3	0.50	1
Na	mg/l	11300.00	12941.73	12141.89	12325.25	13210.00	12683.40	17664.84	12154.33	12295.47
K	mg/l	475.00	958.86	723.00	1890.73	715.10	1422.03	3276.28	1020.54	549.00
Ca	mg/l	488.00	1918.65	1520.00	5239.90	13449.00	3278.98	8903.14	3457.09	750.00
Sr	mg/L	9.30	30.10	21.40	116.00	15.58	64.80	169.00	71.30	14.30
Mg	mg/l	1415.00	1330.45	1439.40	1502.42	1398.00	1300.32	1456.78	1445.00	1532.00
Mn	mg/l	0.00	153.00	57.40	367.00	36.96	74.40	480.00	299.52	52.50
Fe	mg/l	0.03	2.95	6.82	45.00	0.09	3.96	12.80	6.00	5.70
Li	mg/l	0.13	5.70	2.36	13.95	1.18	11.80	28.10	8.75	1.30
B	mg/l	4.20	39.46	21.30	94.29	9.86	61.49	314.68	46.87	16.42
F	mg/l	1.50	2.48	2.46	11.66		1.60	11.18	1.89	3.09
Cl	mg/l	21000.00	27175.57	23630.01	31446.81		29412.43	49539.51	25392.08	22897.52
Br	mg/l	76.50	118.00	105.60	146.50	98.08	118.00	221.34	110.80	304.20
I	ug/L	0.06	721.90	500.00	5460.00		665.90	4758.00	885.63	300.00
NO3	mg/l		0.65	10.80	7.97		1.35	0.00	3.21	4.09
SO4	mg/l	2800.00	2935.90	3247.87	3152.38		2477.01	2562.73	2959.20	3265.24
C(4)	mg/l	30.00	333.98	308.25	226.70		316.78	274.28	209.24	334.21
S(2-)	mg/l	0.00	36.00	57.00	12.00	0.58	43.00	58.00	2.20	72.00
NO2-	mg/l	0.00	0.04	12.00	0.75		0.13	60.00	0.05	0.22
NH4	mg/l	0.01	9.00	7.08	29.00		14.60	58.00	11.20	8.00
Si	mg/L	1.00	106.00	81.93	183.80		14.60	109.40	94.77	51.18
Be	ug/L	0.61	6.65	3.00	10.20	1.03	2.11	18.30	1.27	3.00
Al	ug/L	25.00	1201.00	60.00	3745.00	387.20	205.00	600.00	1467.33	302.90
Sc	ug/L	1.00	12.30	33.20	82.00	2.17	12.30	47.42	3.50	32.43
Ti	ug/L		12.30	20.00	41.00	0.00	4.10	30.50		20.00
V	ug/L	5.04	17.92	10.68	131.90	6.04	6.71	20.30	18.41	11.97
Cr	ug/L	1.00	32.80	80.00	291.10	3.91	41.00	433.10	2.35	170.00
Co	ug/L	0.10	0.78	0.94	6.07	0.08	1.76	19.40	1.55	3.61
Ni	ug/l	1.00	106.60	356.70	974.40	110.90	237.80	710.00	64.68	385.40
Cu	ug/L	10.00	143.50	172.20	192.70	13.14	188.60	244.00	8.07	159.90
Zn	ug/L	25.00	324.00	688.00	71840.00	927.30	159.90	203.50	855.67	217.30
Ga	ug/l	0.37	1.47	1.23	6.45	0.21	0.82	9.30	2.16	0.82
Ge	ug/L		0.82	1.23	7.14	0.84	3.69	7.93		0.82
As	ug/L	2.00	16.12	28.29	1259.70	7.32	16.27	54.90	948.30	40.59
Se		42.00	39.48	41.23	52.73	23.87	456.90	95.82	53.47	43.31
Rb	ug/l	145.85	5258.00	2723.00	14000.00	1291.00	9390.00	27807.00	6903.67	784.20

Y	ug/l	0.01	55.30	5.91	40.28	12.95	2.30	4.75	2.51	3.90
Zr	ug/L	0.03	0.30	0.82	1.23		0.30	1.22	0.10	0.82
Nb	ug/L	0.00	0.30	0.30	0.30		0.30	0.15	0.10	0.30
Mo	ug/L	27.08	31.94	22.33	42.44	3.66	32.75	99.50	54.35	23.24
Ru	ug/L		0.12	0.32	1.23		0.12	0.61		0.31
Pd	ug/l		0.12	6.97	5.33		5.74	12.40		7.38
Ag	ug/L	0.50	2.46	6.00	12.30	0.60	2.46	10.01	0.20	8.09
Cd	ug/L	0.10	0.45	0.82	578.10	0.08	0.14	4.27	0.84	3.69
In	ug/L	0.03	0.13	0.08	0.88	0.03	0.11	0.41	0.16	0.08
Sn	ug/L	0.05	4.54	5.70	16.95	0.23	5.24	9.98	2.21	6.75
Sb	ug/L	0.30	0.38	0.82	5.33	0.22	0.47	4.88	108.00	0.41
Te	ug/L	1.50	1.99	3.00	6.63	0.20	7.76	35.01	2.94	3.00
Cs	ug/l	0.50	1277.00	739.00	3868.00	291.00	2631.00	8587.00	2236.33	210.90
Ba	ug/l	8.00	992.40	760.00	7617.00	93.48	1019.00	5654.70	6337.00	6966.00
La	ug/l	9.08	1.46	1.56	4.24	0.55	1.85	1.34	0.82	1.39
Ce	ug/l	0.15	5.34	8.98	11.10	1.39	12.96	11.47	1.72	8.53
Pr	ug/L	0.02	1.01	0.37	1.15		0.49	0.37	0.22	0.37
Nd	ug/L	0.05	5.73	1.44	5.39	1.39	1.93	1.46	0.90	1.64
Sm	ug/L	0.01	2.73	0.33	2.26	0.69	0.49	0.49	0.29	0.40
Eu	ug/L	0.01	1.21	0.09	2.12	0.27	0.16	0.73	0.98	0.99
Gd	ug/L	0.01	6.11	0.41	4.64	1.40	0.45	0.76	0.43	0.70
Tb	ug/L	0.01	1.20	0.08	1.05	0.30	0.05	0.18	0.07	0.12
Dy	ug/L	0.01	8.09	0.45	6.46	1.94	0.33	0.87	0.44	0.62
Ho	ug/L	0.01	1.71	0.13	1.35	0.41	0.04	0.18	0.09	0.12
Er	ug/L	0.01	4.72	0.41	3.96	1.15	0.21	0.41	0.26	0.30
Tm	ug/L	0.01	0.60	0.05	0.55	0.15	0.01	0.06	0.03	0.04
Yb	ug/L	0.01	3.46	0.34	3.51	0.94	0.16	0.31	0.22	0.25
Lu	ug/L	0.01	0.51	0.08	0.53	0.14	0.01	0.06	0.03	0.04
Hf	ug/L	0.00	0.01	0.03	0.08		0.01	0.12	0.00	0.03
Ta	ug/L	0.00	0.01	0.03	0.03		0.01	0.12	0.00	0.03
W	ug/L	0.10	10.25	0.73	0.77		0.25	364.00	0.00	87.74
Os	ug/L		0.02	0.06	0.08		0.02	0.12	0.00	0.06
Pt	ug/L		3.69	9.93	9.12		3.69	9.00	0.00	10.86
Au	ug/L	0.01	0.29	0.74	0.08		0.02	0.12	0.00	0.16
Hg	ug/L	0.00	2.46	7.38	6.09		2.46	11.20		6.00
Tl	ug/l	0.10	160.80	245.83	286.90	9.76	177.00	326.60	165.00	104.14
Pb	ug/L	0.10	14.00	4.50	1095.00	12.17	1.27	9.42	37.00	7.50
Bi	ug/L	0.07	3.69	9.92	11.19	0.01	3.69	15.35	0.18	10.03
Th	ug/L	0.11	0.03	0.03	0.22	0.04	0.03	0.06	0.22	0.08
U	ug/l	3.50	1.09	3.57	3.36	2.49	1.68	3.10	3.34	3.25

Tab. 13: Calculated SI for fluid data *without* sea water mixing

Red-colored values indicate possible mineral precipitation due to oversaturation (positive SI), values between -0.1 and 0.1 mean equilibrium

	Vulcano seawater	A26	BN	BP	CA	FF	HL	LC	P21
pH	8.2	4.5	5.3	2.4	4.8	5.4	4.4	4.6	4.7
temp	25	58.4	65.1	134.1	40.2	60	78.7	116	74
SI_Al(OH)3(a)	-2.54	-3.18	-2.45	-5.68	-1.88	-1.48	-4.47	-0.65	-3.11
SI_Albite	-1.70	-0.52	**0.42**	-5.92	-1000.00	-0.50	-1.74	**0.64**	-1.65
SI_Alunite	-5.69	**1.27**	**0.66**	-4.07	**4.91**	**3.54**	-3.53	**5.32**	-0.17
SI_Anhydrite	-0.86	-0.06	**-0.04**	**0.93**	**0.43**	**0.08**	**0.59**	**0.72**	-0.26
SI_Anorthite	-3.93	-6.50	-3.57	-12.88	-1000.00	-2.68	-7.58	**0.43**	-6.54
SI_Aragonite	**0.73**	-2.27	-0.84	-5.65	-1.08	-0.36	-1.53	-1.59	-2.16
SI_Calcite	**0.87**	-2.15	-0.72	-5.56	-0.95	-0.23	-1.42	-1.50	-2.04
SI_Celestite	-0.56	-0.06	-0.14	**0.58**	-0.59	**0.16**	**0.51**	**0.45**	-0.28
SI_Chalcedony	-0.81	**0.92**	**0.73**	**0.61**	-1000.00	**0.06**	**0.88**	**0.41**	**0.44**
SI_Chlorite(14A)	**7.92**	-17.23	-6.88	-30.68	-1000.00	-7.03	-15.98	-2.15	-13.16
SI_Chrysotile	**2.78**	-11.75	-6.55	-17.74	-1000.00	-7.88	-9.75	-6.53	-9.70
SI_Dolomite	**2.59**	-3.90	-0.95	-12.15	-2.33	-0.31	-3.12	-3.50	-3.32
SI_Fe(OH)3(a)	-4.80	-9.94	-8.47	-12.29	-10.73	-8.53	-9.59	-9.19	-9.34
SI_FeS(ppt)	-2.16	-1.64	**0.17**	-5.18	-4.39	**0.04**	-0.88	-2.33	-0.67
SI_Fluorite	-1.18	-1.44	-0.89	-1.70	-1000.00	-0.98	**0.78**	-1.64	-1.25
SI_Gibbsite	**0.15**	-0.77	**-0.08**	-3.71	**0.68**	**0.93**	-2.19	**1.41**	-0.80
SI_Goethite	**1.10**	-2.97	-1.31	-3.54	-4.31	-1.51	-2.06	-0.81	-1.94
SI_Gypsum	-0.58	-0.12	-0.16	**0.21**	**0.55**	**0.00**	**0.33**	**0.16**	-0.46
SI_Hausmannite	-29.91	-30.40	-26.16	-30.64	-33.42	-26.26	-26.92	-20.51	-28.18
SI_Hematite	**4.22**	-3.78	-0.44	-4.69	-6.54	-0.86	-1.88	**0.72**	-1.67
SI_Illite	-0.80	-0.37	**1.41**	-10.17	-1000.00	**1.62**	-3.38	**3.17**	-1.93
SI_Jarosite-K	-22.40	-24.45	-22.07	-21.92	-29.40	-22.88	-22.06	-19.86	-22.52
SI_K-feldspar	-0.81	**0.21**	**1.03**	-5.42	-1000.00	**0.40**	-0.84	**1.04**	-1.25
SI_K-mica	**5.13**	**4.52**	**6.75**	-6.48	-1000.00	**8.11**	**0.77**	**10.09**	**3.08**
SI_Kaolinite	**0.39**	**1.94**	**2.92**	-4.69	-1000.00	**3.60**	-1.01	**5.18**	**0.89**
SI_Mackinawite	-1.42	-0.90	**0.90**	-4.45	-3.66	**0.77**	-0.15	-1.59	**0.06**
SI_Manganite	-13.72	-16.49	-15.62	-20.81	-16.07	-15.31	-16.73	-16.68	-16.85
SI_Melanterite	-7.48	-6.04	-5.98	-5.73	-7.50	-6.33	-6.03	-6.28	-5.89
SI_Pyrite	**4.50**	**9.36**	**10.55**	**3.23**	5.99	**10.50**	**9.39**	**5.16**	**9.71**
SI_Pyrochroite	-7.34	-9.72	-8.54	-13.65	-9.73	-8.27	-9.61	-9.27	-9.77
SI_Pyrolusite	-26.00	-24.37	-22.95	-21.11	-26.01	-23.24	-22.49	-18.84	-23.10
SI_Quartz	-0.38	**1.26**	**1.05**	**0.79**	-1000.00	**0.39**	**1.17**	**0.62**	**0.74**
SI_Rhodochr.	-2.46	-1.17	**-0.10**	-5.55	-1.37	**0.15**	-1.01	-1.08	-1.21
SI_Sepiolite	**0.27**	-7.66	-4.71	-14.08	-1000.00	-6.57	-7.00	-6.55	-7.54
SI_Sepiolite(d)	-2.63	-11.35	-8.54	-19.08	-1000.00	-10.29	-11.09	-11.28	-11.55
SI_Siderite	-1.20	-2.91	-1.36	-6.37	-4.00	-1.40	-2.49	-2.73	-2.25
SI_SiO2(a)	-1.65	**0.18**	**0.01**	**0.04**	-1000.00	-0.68	**0.20**	-0.20	-0.25
SI_Sulfur	-5.85	-0.28	-0.66	-0.35	-1.55	-0.76	-0.30	-1.86	-0.35

Tab. 14: Chondrite-normalized REE values of hydrothermal fluids (Panarea, Italy)

Elements	A26	BN	BP	CA	FF	HL	LC	P21
La	0.00618	0.00657	0.01790	0.00232	0.00782	0.00566	0.00345	0.00588
Ce	0.00870	0.01465	0.01811	0.00226	0.02114	0.01871	0.00280	0.01391
Pr	0.01085	0.00398	0.01242		0.00530	0.00394	0.00233	0.00398
Nd	0.01253	0.00314	0.01179	0.00305	0.00422	0.00320	0.00197	0.00359
Sm	0.01846	0.00222	0.01528	0.00467	0.00332	0.00330	0.00198	0.00270
Eu	0.02142	0.00155	0.03762	0.00485	0.00281	0.01288	0.01738	0.01750
Gd	0.03068	0.00206	0.02331	0.00702	0.00227	0.00383	0.00215	0.00352
Tb	0.03327	0.00227	0.02906	0.00817	0.00150	0.00499	0.00191	0.00341
Dy	0.03289	0.00183	0.02628	0.00790	0.00133	0.00354	0.00177	0.00250
Ho	0.03128	0.00234	0.02467	0.00744	0.00075	0.00322	0.00170	0.00225
Er	0.02948	0.00256	0.02476	0.00720	0.00128	0.00256	0.00162	0.00188
Tm	0.02409	0.00211	0.02215	0.00619	0.00050	0.00227	0.00138	0.00162
Yb	0.02150	0.00209	0.02180	0.00585	0.00102	0.00189	0.00138	0.00153
Lu	0.02053	0.00333	0.02138	0.00573	0.00050	0.00246	0.00134	0.00166

Tab. 15: Geochemical data of minerals

Mineral	Formula	C	Na	Al	Si	S	K	Ca	Mn	Fe	Pb	Zn	Ba
Ab	$NaAlSi_3O_8$		7-9	10-12	30-33			0-2					
Alunite	$KAl_3(SO_4)_2(OH)_6$			19-20		15-16	8-10						
An	$CaAl_2Si_2O_8$			18-20	20-22			13-15					
Brt	$BaSO_4$					13-14							58-59
Gn	PbS					13-15					85-87		
Gt	$FeOOH$									62-63			
Hem	Fe_2O_3								0-1	68-70			
Or	$KAlSi_3O_8$			7-13	23-33		8-15						
Py/Mrc	FeS_2					40-60				40-60			
Qz	SiO_2				35-65								
Rds	$Mn(CO_3)$	10-11							45-60				
Sp	ZnS					32-34			0-3	0-18		44-67	

Tab. 16: EQ3/6 results for mixing of BP fluid with sea water (mass ratio factor 5)

log xi	temp (°C)	press	pH	log fo2	Eh	pe
-999	150	4.7572	2.4389	-50.9841	-0.0643	-0.7656
-8	150	4.7572	2.4389	-50.9841	-0.0643	-0.7656
-7.5	149.9999	4.7572	2.4389	-50.9841	-0.0643	-0.7656
-7	149.9998	4.7572	2.4389	-50.9841	-0.0643	-0.7656
-6.5	149.9992	4.7571	2.4389	-50.9841	-0.0643	-0.7656
-6	149.9975	4.7569	2.4389	-50.9840	-0.0643	-0.7655
-5.5	149.9921	4.7562	2.4390	-50.9838	-0.0643	-0.7653
-5	149.9750	4.7540	2.4390	-50.9831	-0.0642	-0.7646
-4.5	149.9210	4.7471	2.4392	-50.9808	-0.0640	-0.7624
-4	149.7505	4.7255	2.4399	-50.9737	-0.0634	-0.7553
-3.5	149.2144	4.6579	2.4420	-50.9515	-0.0614	-0.7332
-3	147.5490	4.4530	2.4495	-50.8874	-0.0556	-0.6661
-2.5	142.5646	3.8826	2.4770	-50.7859	-0.0404	-0.4903
-2.0453	130.9144	2.7771	2.5634	-50.9598	-0.0149	-0.1863
-2.0338	130.4847	2.7419	2.5654	-50.9820	-0.0142	-0.1774
-2	129.1667	2.6360	2.5759	-51.0340	-0.0120	-0.1500
-1.8955	124.6479	2.2980	2.6080	-51.2804	-0.0053	-0.0666
-1.5755	106.6153	1.2792	2.6227	-53.2028	0.0142	0.1888
-1.5687	106.1729	1.2599	2.6225	-53.2596	0.0146	0.1941
-1.5	101.5718	1.0720	2.6198	-53.8760	0.0184	0.2468
-1.1331	75.5639	1.0132	2.5941	-57.9198	0.0361	0.5216
-1	66.6667	1.0132	2.5870	-59.4932	0.0413	0.6126
-0.5618	44.2723	1.0132	2.5992	-63.8279	0.0530	0.8414
-0.5	42.0659	1.0132	2.6059	-64.2811	0.0539	0.8625
-0.2383	34.9567	1.0132	2.6495	-65.7618	0.0561	0.9175
0	30.9524	1.0132	2.7176	-66.6047	0.0551	0.9127
	Quartz	Numbers below mineral names indicate their precipitation				
-999	-3.3878					
-8	-3.3878					
-7.5	-3.3878					
-7	-3.3878					
-6.5	-3.3877					
-6	-3.3877					
-5.5	-3.3875					
-5	-3.3868					
-4.5	-3.3847					
-4	-3.3781					
-3.5	-3.3581					
-3	-3.3018					
-2.5	-3.1708					
	Quartz					
-2.0453	-2.9783					

	Quartz				
-2.0338	-2.9729				
-2	-2.9571				
	Quartz	**Sphalerite**			
-1.8955	-2.9081	-6.6958			
	Quartz	**Sphalerite**			
-1.5755	-2.7689	-3.6587			
	Quartz	**Sphalerite**			
-1.5687	-2.7663	-3.6415			
-1.5	-2.7411	-3.5896			
	Barite	**Quartz**	**Sphalerite**		
-1.1331	-7.1417	-2.6427	-3.4696		
-1	-4.6562	-2.6206	-3.4558		
	Barite	**Galena**	**Quartz**	**Sphalerite**	
-0.5618	-4.3239	-8.1510	-2.5834	-3.4405	
-0.5	-4.3131	-6.2994	-2.5813	-3.4404	
	Barite	**Galena**	**Pyrite**	**Quartz**	**Sphalerite**
-0.2383	-4.2883	-5.7143	-6.6859	-2.5796	-3.4411
0	-4.2800	-5.5959	-4.8526	-2.5877	-3.4759

Tab. 17: **EQ3/6 results for mixing of BP fluid with sea water (mass ratio factor 20)**

log xi	temp (°C)	press	pH	log fo2	Eh	pe
-999	150	4.7572	2.4389	-50.9841	-0.0643	-0.7656
-8	150	4.7572	2.4389	-50.9841	-0.0643	-0.7656
-7.5	150	4.7572	2.4389	-50.9841	-0.0643	-0.7656
-7	149.9999	4.7572	2.4389	-50.9841	-0.0643	-0.7656
-6.5	149.9998	4.7571	2.4389	-50.9840	-0.0643	-0.7656
-6	149.9994	4.7569	2.4389	-50.9838	-0.0643	-0.7655
-5.5	149.9980	4.7562	2.4390	-50.9831	-0.0643	-0.7653
-5	149.9938	4.7540	2.4390	-50.9809	-0.0642	-0.7647
-4.5	149.9802	4.7471	2.4393	-50.9739	-0.0640	-0.7627
-4	149.9375	4.7255	2.4400	-50.9521	-0.0635	-0.7565
-3.5	149.8027	4.6579	2.4424	-50.8846	-0.0619	-0.7374
-3	149.3781	4.4530	2.4505	-50.6876	-0.0571	-0.6814
-2.5	148.0543	3.8826	2.4794	-50.2082	-0.0455	-0.5440
-2	144.0476	2.7771	2.5877	-49.3497	-0.0245	-0.2954
-1.9247	142.9837	2.7419	2.6191	-49.1975	-0.0207	-0.2505
-1.9136	142.8120	2.6360	2.6225	-49.1829	-0.0201	-0.2441
-1.5717	135.2250	2.2980	2.7515	-49.1114	-0.0062	-0.0760
-1.5	132.9341	1.2792	2.7588	-49.2895	-0.0033	-0.0413
-1.438	130.7194	1.2599	2.7629	-49.4899	-0.0009	-0.0109

-1	108.3333	1.0720	2.7472	-52.2172	0.0179	0.2359
-0.9295	103.7072	1.0132	2.7389	-52.8728	0.0212	0.2831
-0.9292	103.6907	1.0132	2.7389	-52.8752	0.0212	0.2832
-0.9286	103.6458	1.0132	2.7391	-52.8820	0.0212	0.2833
-0.8943	101.3195	1.0132	2.7346	-53.2217	0.0228	0.3068
-0.5	73.4282	1.0132	2.6982	-57.7540	0.0393	0.5710
0	45.8333	1.0132	2.7471	-63.1102	0.0490	0.7739

	Quartz	Numbers below mineral names indicate their precipitation				
-999	-3.3878					
-8	-3.3878					
-7.5	-3.3878					
-7	-3.3878					
-6.5	-3.3878					
-6	-3.3877					
-5.5	-3.3877					
-5	-3.3875					
-4.5	-3.3871					
-4	-3.3856					
-3.5	-3.3808					
-3	-3.3664					
-2.5	-3.3246					
-2	-3.2211					

	Quartz					
-1.9247	-3.1979					

	Quartz					
-1.9136	-3.1943					

	Quartz	**Sphalerite**				
-1.5717	-3.0609	-6.6138				
-1.5	-3.0285	-4.3683				

	Pyrite	**Quartz**	**Sphalerite**			
-1.4380	-6.6865	-3	-4.1156			
-1	-5.0899	-2.8058	-3.6127			

	Barite	**Pyrite**	**Quartz**	**Sphalerite**		
-0.9295	-7.2494	-6.1840	-2.7795	-3.5590		

	Barite	**Pyrite**	**Quartz**	**Sphalerite**		
-0.9292	-7.0004	-6.0595	-2.7794	-3.5589		

	Barite	**Galena**	**Quartz**	**Sphalerite**		
-0.9286	-6.6677	-5.3859	-2.7792	-3.5588		

	Barite	**Quartz**	**Sphalerite**			
-0.8943	-5.2213	-2.7672	-3.5350			
-0.5	-4.3894	-2.6684	-3.4603			
0	-4.2948	-2.6318	-3.4425			